Axisymmetric Numerical and Analytical Studies of the Magnetorotational Instability in a Magnetized Taylor-Couette Flow

Wei Liu

a dissertation

presented to the faculty

of princeton university

in candidacy for the degree

of doctor of philosophy

recommended for acceptance

by the department of

astrophysical sciences

November, 2007

Abstract

The magnetorotational instability (MRI) is probably the main cause of turbulence and accretion in sufficiently ionized astrophysical disks. However, despite much theoretical and computational work, the nonlinear saturation of MRI is imperfectly understood. In Chap. 2 and Chap. 3 of this thesis we present non-ideal magnetohydrodynamic simulations of the Princeton MRI experiment. In vertically infinite or periodic cylinders, MRI saturates in a resistive current-sheet with a significant reduction of the mean shear, and with poloidal circulation scaling as the square root of resistivity. Angular momentum transport scales as the reciprocal square root of viscosity but only weakly depends on resistivity. For finite cylinders with insulating end caps, a method for implementing the fully insulating boundary condition is introduced. MRI grows with a clear linear phase from small amplitudes at rates in good agreement with linear analysis. In the final state one inflowing "jet" opposite to the usual Ekman "jet" is found near the inner cylinder. The MRI enhances the angular momentum transport at saturation. Under proper conditions, our experimental facility is a good platform to show that MRI could be suppressed by a strong magnetic field.

Recently, Hollerbach and Rüdiger have reported that MRI modes may grow at much reduced magnetic Reynolds number (Re_m) and Lundquist number S in the

presence of a helical background field, a current-free combination of axial and toroidal field. We have investigated these helical MRI modes in Chap. 4 and Chap. 5. In vertically infinite or periodic cylinders, resistive HMRI is a weakly destabilized hydrodynamic inertial oscillation propagating axially along the background Poynting flux. Growth rates are small, however, and require large axial currents. Furthermore, finite cylinders with insulating endcaps were shown to reduce the growth rate and to stabilize highly resistive, inviscid flows entirely, and the new mode is stable in Keplerian flow profiles regardless of end conditions. We also numerically investigate a traveling wave pattern observed in experimental magnetized Taylor-Couette flow at low magnetic Reynolds number. By accurately modeling viscous and magnetic boundaries in all directions, we reproduce the experimentally measured wave patterns and their amplitudes. Contrary to previous claims, the waves are shown to be transiently amplified disturbances launched by viscous boundary layers rather than globally unstable magnetorotational modes.

The experiment is complicated by the extremely large Reynolds number and by Ekman circulation and Stewartson layers, even though the experimental apparatus has been designed to minimize the circulation (*e.g.* by the use of independently controlled split endcaps). Understanding the role of the boundary layers is critical to this research. In Chap. 6 the magnetic field is found to inhibit the Ekman suction. While we quantitatively confirmed the conclusions of Gilman *et al*, the finite differential rotation cannot be neglected and modifies the linear Ekman layer. The width of the Ekman layer is reduced with increased magnetic field normal to the end plate. A uniformly-rotating region forms near the outer cylinder. The Stewartson layer penetrates deeper into the fluid with larger Reynolds number and stronger magnetic field. Furthermore a strong magnetic field leads to a steady Stewartson layer, at least in axisymmetric configuration.

Acknowledgements

I am gratefully indebted to my primary thesis advisor, Prof. Jeremy Goodman, for his tireless efforts on behalf of my graduation education. His insight, stimulating suggestions, and passion for science has made this experience fruitful and memorable. He was always patient, and ensured that I understood every subtle point.

I would like to offer sincere thanks and appreciation to my co-advisor, Prof. Hantao Ji, who is an inspiring mentor, and initiated me into this fascinating world of plasma astrophysics. His quest for perfection and constant encouragement made this thesis possible.

I am much obliged to Prof. James Stone and Prof. Stephen Jardin for their help with numerical methods as well as providing access to their commendable knowledge and wisdom. Many thanks are due to Prof. Roscoe B. White for his role as my faculty advisor and to Prof. Greg Hammett for his role on my thesis committee. Special thanks to Prof. James Stone and Prof. Masaaki Yamada for kindly being the readers of my thesis.

I would like to express my gratitude to all my colleagues of our group, who gave me various assistance in my research work, especially Dr. Michael Burin, Mr. Ethan Schartman, Dr. Mark Nornberg and Mr. Brendan McGeehan. I want to thank them for all their help, interest, and valuable hints. Special thanks to Dr. Mark Nornberg,

Dr. Stefan Gerhardt, Mr. Nathaniel Ferraro, Mr. Timothy Stoltzfus-Dueck and Mr. Erik Granstedt for kindly proofreading my thesis and various suggestions to make this thesis better.

Also thanks to Prof. Ronald C. Davidson, Prof. Phil Efthimion and Dr. Eric Gilson, with whom I spent my first year on PTSC project. That is a very pleasant experience in my life.

And I would also like to thank Prof. Nat Fisch and Ms. Barbara Sarfaty, who provided me the chance to attend Princeton and offered me warm-hearted assistance throughout these years. Thanks to my wonderful friends: thank you all for the enjoyment and happiness so far, and that yet to come. Without you, life is just without salt.

Finally, Thanks to my loving and supporting family: my parents, Chengzhou and Lingling, my brother, Zhong, my sister, Juan. No words can express my profound appreciation and love for my wife, Jie, who is a designated lovely millennium gift from God. Without her, my life is just in the darkness.

This work was supported by the US Department of Energy, NASA under grants ATP03-0084-0106 and APRA04-0000-0152 and also by the National Science Foundation under grant AST-0205903.

Contents

List of Tables

List of Figures

Chapter 1

Introduction

1.1 An informal overview of accretion disks

"An accretion disk consists of gas, dust and plasmas rotating around and slowly accreting onto a central point-like object. Accretion disks are the most efficient energy source known to astrophysics. Whereas hydrogen fusion has a maximum efficiency for converting rest-mass to radiation $\lesssim 1\%$, accretion onto a black hole or neutron star can have efficiency $\sim 5-40\%$. Accretion disks power many of the most luminous and violent astrophysical sources"[1], including:

- Formation of stars and planets in proto-star systems (Fig. 1.1 (a));
- Mass transfer and energetic activity in binary stars (Fig. 1.1 (b));
- Release of energy (as luminous as 10^{15} of Sun) in quasars (Fig. 1.1 (c)) and Active Galactic Nucleus (AGN).

"Accretion disks around young stars, though energetically much less efficient and luminous, are nevertheless of great interest as sites of planet formation."[1]

[1] taken from the 2003 project proposal entitled "Numerical and Theoretical Studies of Magnetorotational Instability in a Gallium Disk" authored by Hantao Ji, Jeremy Goodman, James Stone and Akira Kageyama

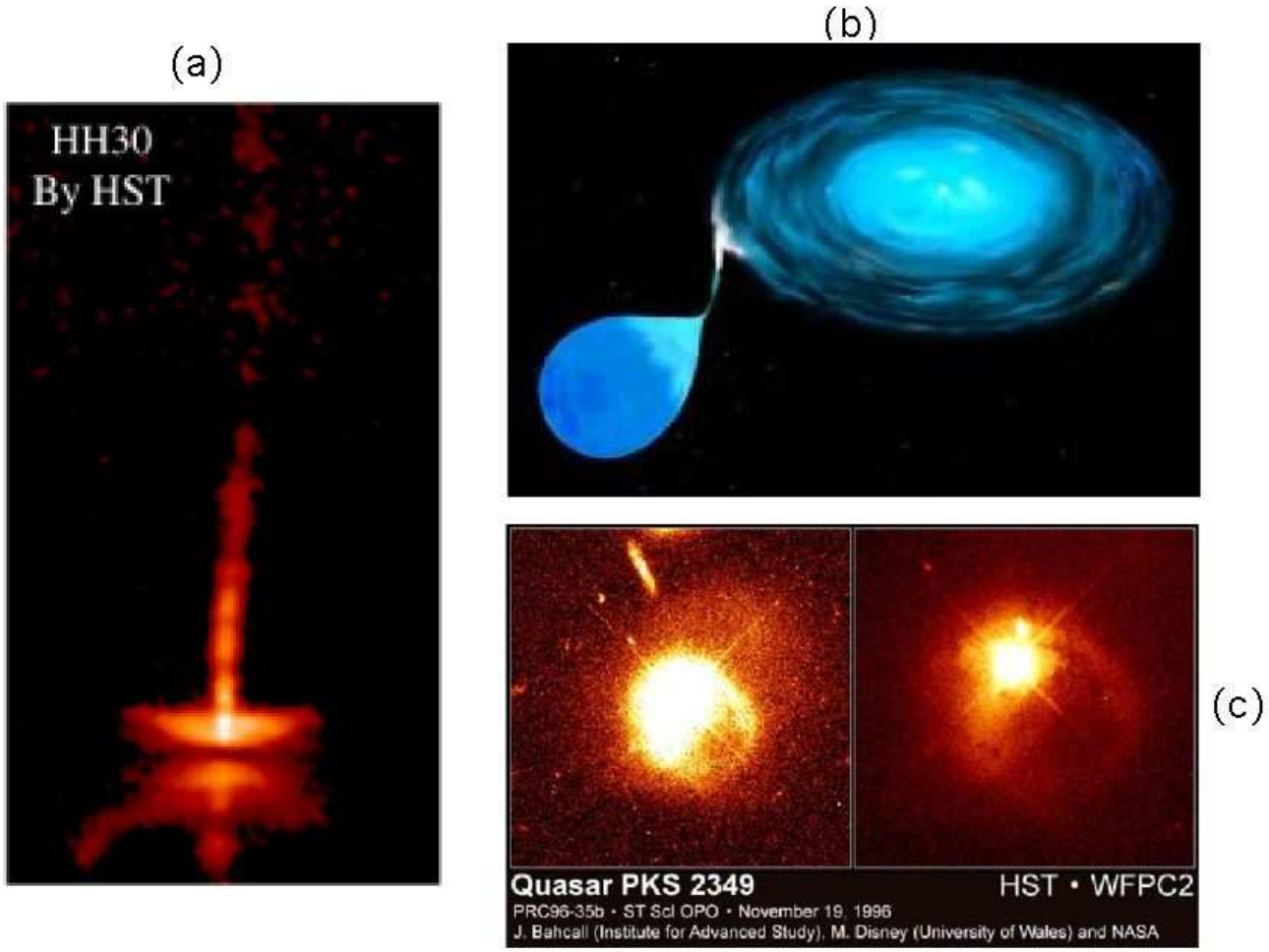

Figure 1.1: Figure (a) (c) courtesy of HST; Figure (b) courtesy of Space Telescope Science Institute, NASA.

A long-standing puzzle to the theory of accretion disks has been to show from first principles how they accrete [1]. Principally the shear molecular viscosity transfers angular momentum from one fluid element to another. In almost all cases, however, the observational inferred accretion rates are much higher than those predicted by standard microscopic viscosities due to collisions can supply [2]. For the completeness, we start from a minimum introduction to accretion disks here. A comprehensive introduction to thin-disk accretion can be found in Pringle [3]. Jeremy Goodman also has a good set of pedagogical introduction notes (unpublished) to the thin disks [4]. Part of the following introduction is inherited and modified from those notes. For more details, people could refer to Pringle [3] or Goodman [4].

1.1.1 Accretion[2]

In this section the cylindrical coordinate (r, φ, z) is chosen, which is aligned with the rotation axis and mid-plane of the disk. The Keplerian rotation angular frequency is $\Omega \sim r^{-3/2}$. Axisymmetry is assumed in this whole section. Disk orbits are not quite closed circles but gradually contracting spirals. Most of the plasma eventually ends up on the central star or black hole, though a fraction may be expelled as a wind or jet. This process is called accretion. The accretion rate $\dot{M}$ is defined as the integrated mass flux across an infinite cylinder centered on the rotation axis:

$$\dot{M}(r,t) \equiv -\int_{-\infty}^{\infty} dz \int_{0}^{2\pi} \rho v_r r d\varphi \,, \tag{1.1}$$

where ρ is the density and v_r is the radial velocity. Assuming v_r is a constant along the height, $\dot{M} = -2\pi r v_r \Sigma$, where the mass per unit area is defined as:

$$\Sigma(r,t) \equiv \int_{-\infty}^{\infty} \rho(r,z) dz \,.$$

[2]inherited and modified from Goodman [4]

The accretion rate $\dot{M}$ is defined in such a way that $\dot{M} > 0$ if mass flows inwards.

1.1.2 Steady accretion and transport[3]

The necessity of the angular momentum transport could be demonstrated clearly in a steady axisymmetric disk. Thus $\Sigma = \Sigma(r)$. It also follows that $\dot{M}$ must be constant with r in a steady disk since

$$-2\pi r \frac{\partial \Sigma}{\partial t} = \frac{\partial \dot{M}}{\partial r} \,.$$

We can also define $\dot{\mathrm{J}}$ as the accretion rate of the angular momentum similar to $\dot{M}$:

$$\dot{\mathrm{J}}(r,t) \equiv -\int_{-\infty}^{\infty} dz \int_{0}^{2\pi} \rho J v_r r d\varphi \,,$$

in which J is the specific angular momentum defined as:

$$J \equiv r^2 \Omega \,.$$

The angular momentum in the disk between r and $r + dr$ is $2\pi r J \Sigma dr$, therefore we get:

$$-2\pi r J \frac{\partial \Sigma}{\partial t} = \frac{\partial \dot{\mathrm{J}}}{\partial r} \tag{1.2}$$

on the assumption of $\partial J/\partial t = 0$ (This is not quite right, however on typical time scales of the disk the variation of J could be neglected since $J = \sqrt{GMr}$, where G is the gravitational constant and M is the mass of the central object of the disk). From Eq. 1.2, we can see that the accretion rate of the angular momentum $\dot{\mathrm{J}}$ must also be independent of r in steady state.

Part of $\dot{\mathrm{J}}$ should be the advection of angular momentum by the accreting mass

[3]inherited and modified from Goodman [4]

$J\dot{M}$. However there must be an additional contribution to $\dot{\mathrm{J}}$,

$$\Gamma = -\dot{\mathrm{J}} + J\dot{M}\,, \tag{1.3}$$

to make in steady state

$$\frac{d\Gamma}{dr} = \dot{M}\frac{dJ}{dr} \tag{1.4}$$

so that $d\dot{\mathrm{J}}/dr = 0$. Immediately we get $\Gamma(r) = \dot{M}J(r)+\Gamma_0$, where Γ_0 is the integration constant depending upon the boundary conditions at the inner edge of the disk, which is unimportant at large radii since J increases with r.

Up to this point, we have not specified the physical details of the torque Γ but rather simply applying the conservation of mass and angular momentum with the assumption of *steady state*.

1.1.3 Effective viscosity and the α parameter[4]

By comparing with fluid turbulence, astrophysicists introduce an effective kinematic viscosity ν defined as:

$$\Gamma \equiv -2\pi r^3 \Sigma\nu\frac{d\Omega}{dr}\,,$$

Thus in the steady state

$$\dot{M} = -2\pi\Sigma\nu\frac{d\ln\Omega}{d\ln r} + \frac{\Gamma_0}{J}\,, \tag{1.5}$$

and Hence, except near the inner edge, in a steady Keplerian disk, we get:

$$\dot{M} \approx 3\pi\nu\Sigma\,.$$

Principally the shear molecular viscosity transfers angular momentum from one fluid element to another. In almost all cases, however, the observational inferred ac-

[4]inherited and modified from Goodman [4]

cretion rates are much higher than those predicted by standard microscopic viscosities due to collisions can supply [2]. The effective viscosity enhanced due to turbulence could be large enough to provide the observed accretion rates. Hence it has been argued that ν results from turbulence and/or magnetic stresses. Shakura and Sunyaev [5] introduced the α parameter as:

$$\tau_{r\varphi} \equiv \alpha p \,, \tag{1.6}$$

where τ_{ij} is the viscous stress tensor and p is the plasma pressure excluding the magnetic pressure but possibly including radiation pressure. Usually this parameter is defined alternately as:

$$\nu = \alpha V_s H \,, \tag{1.7}$$

in which V_s is the sound speed while the vertical scale height H is defined as:

$$H \equiv \frac{V_s}{\Omega} \,.$$

Shakura and Sunyaev [5] used dimensional analyses to postulate that $\alpha < 1$. Given the observational constrains (only on $\dot{M}$ and/or Σ), a more reasonable relation with height average replaces Eq. 1.6:

$$\frac{\Gamma}{2\pi r^2} = \int_{-\infty}^{\infty} \alpha p dz \equiv \bar{\alpha} \int_{-\infty}^{\infty} p dz \,. \tag{1.8}$$

Local three-dimension simulation with a large plasma parameter $\beta \equiv 8\pi p / \langle B \rangle^2$, where $\langle B \rangle$ is the volume-averaged magnetic field under the "shearing-box" geometry show that the averaged parameter $\bar{\alpha}$ is around 0.01 [1, 6], which is separately verified by several groups with different codes [7–9]. Global simulations tend to have larger $\bar{\alpha}$ with values around 0.1, though no global simulations of MRI in truly thin disks have been performed as yet [10, 11].

1.1.4 α value from observation[5]

To measure the disk viscosity from direct astrophysical observations might be more effective than the purely theoretical analyses [3]. However, it is basically not "possible" to explain the observations in a unambiguous way especially for disks in steady state. The most common systems in which accretion disks exist and in which their time-varying behavior can be studied are the cataclysmic variables, a class of binary stars containing a white dwarf and a companion star. When modeling the outburst of TCrB, a recurrent nova, Webbink [12] defines an effective Reynolds number Re in the disk as:

$$Re_\nu \simeq 6 \left(\frac{GM}{R_d^3} \right)^{1/2} \tau_\nu \,,$$

where R_d is the circular orbit radius and $\tau_\nu = R_d^2/6\nu$ is the natural viscous time scale. Note Re_ν as defined does not depend upon disk thickness or temperature, but the inferred value of α does. Also note that Re_ν involves the turbulent rather than the true viscosity, in contrast with the Reynolds number quoted in Table.1.1 later on. The observations suggest an effective Reynolds number of the order $\sim 10^3$. For dwarf nova outbursts, Re_ν in the range $10^2 - 10^3$, or α in the range $0.1 - 1$ fit the data nicely [13, 14]. Whether the viscosity remains at that level or descends to a lower level during quiescence is still an open question [15, 16].

1.2 Two main possible mechanisms for fast accretion

1.2.1 Nonlinear Hydrodynamical Instability

A long-standing puzzle to the theory of accretion disks has been to show from first principles how the disks accrete [1]. As discussed in §1.1.3, an enhanced turbulence

[5] inherited and modified from Pringle [3]

viscosity is a must. It is natural for people to relate the source of turbulence to the famous Rayleigh's centrifugal instability, which takes place if the specific angular momentum decreases outward. In most astrophysical disks, which usually have Keplerian rotational profile, this requirement is not satisfied. However provided a large Reynolds number $Re \equiv UL/\nu$ (where U is the characteristic large-scale flow velocity, L is its associated length scale and ν is the microscopic viscosity.), the differentially rotating flow might be unstable to a nonlinear disturbance, the so-called *nonlinear hydrodynamic instability* [17]. In astrophysical disks the Reynolds number is very high. Some astrophysicists argue that disks must be very turbulent given this huge Reynolds number. Based on old Couette experiments [18, 19], Richard and Zahn [20] speculated an effective turbulence viscosity due to purely hydrodynamic turbulence as:

$$\nu_t = -\beta r^3 \frac{\partial \Omega}{\partial r}, \quad \beta \approx 1.5 \times 10^{-5}\,. \tag{1.9}$$

Scaled to the astrophysical disks, it is very important especially for the cold disks, where the particles are too weakly ionized. This argument has been partially confirmed by Richard [21], though their experiment is with small gaps ($\triangle R/R \leqslant 1/3$) and the boundary effects are not well handled (dividing the cap into two parts: the inner one fixed to the inner cylinder, and the outer one fixed to the outer cylinder). Other astrophysicists are not convinced considering the differences between laboratory flow and accretion disk flow, for example, a supersonic shear velocity and lack of confining walls [22]. Generally this issue is still controversial [20, 23–25].

Recently our group [26] reported laboratory results on this topic. In the experiment purely hydrodynamic quasi-keplerian flows with Reynolds numbers $\sim 10^6$ are found to be steady. Angular momentum transport rates are much smaller than the one required in astrophysical disks after scaling the results to them. Our results exclude the purely nonlinear hydrodynamic instability and imply that MRI might also be important in poorly magnetized disks. Fig. 1.2 shows that β overlaps between

quasi-keplerian and solid-body rotation and is much less than the specified range in Eq. 1.9. In the figure, we gauged the systematic errors of the experiment by comparing quasi-keplerian flows with solid body ones, which must be stable, for lack of free energy.

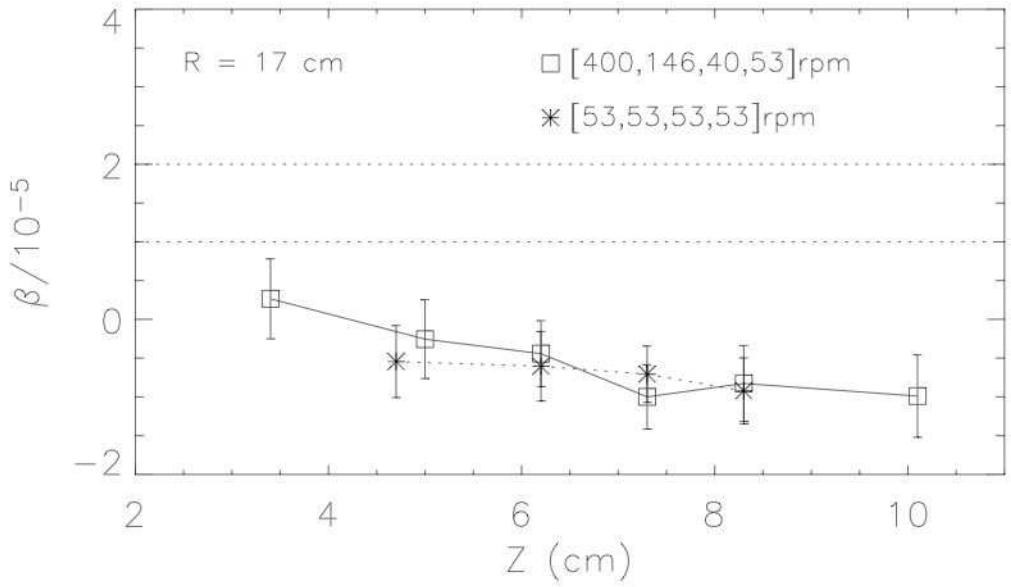

Figure 1.2: Figure courtesy of Ji et al. Experimentally measured Reynolds stress versus height in a quasi-keplerian profile. dashed line, estimated value of $\beta = (1 - 2) \times 10^{-5}$ from Richard and Zahn; $*$, solid rotation; $\Box$, quasi-keplerian rotation.

1.2.2 Magnetorotational Instability

After decades of research, people come to agree that the most promising candidate to provide fast accretion is the so-called *magnetorotational instability* (MRI). In the milestone work by Balbus and Hawley [6] and its companion paper [27], accretion disks were shown to be subject to a very powerful shearing instability imposed by a weak magnetic field, which they called the magnetorotational instability. Although discovered by Velikhov [28] and Chandrasekhar [29], MRI was not studied seriously by the astrophysical community until rediscovered by Balbus and Hawley [6]. MRI

takes place provided that the angular velocity decrease outwards, $\partial\Omega^2/\partial r < 0$, and may occur when the specific angular momentum increases outwards, $\partial(r^2\Omega)^2/\partial r > 0$, which does not apply to Rayleigh's centrifugal instability. These conditions exist in Keplerian disks. Provided a purely axial magnetic field, a simple axis-symmetric instability occurs. If the background field is helical (having both azimuthal and axial component), MRI modes are overstable and the growth rate is reduced [30]. However, it is hard to stabilize a disk totally if there is any axial field [31, 32] unless the disk is a poor conductor, as some may be.

1.3 Basic idea of MRI

The mechanism of MRI can be explored in a simple way by imposing a weak uniform vertical magnetic field in an axisymmetric gas disk (left figure of Fig. 1.3) [1]. The gravitational force is balanced by the centrifugal force, which results in the fluid equilibrium. The uniform vertical magnetic field is not involved in the force balance. Thus it does not have any influence on the equilibrium. Given an initial perturbation with spatial structure $\exp(ikz)$, thus a fluid element is displaced a bit inwards from its original orbit position whereas another fluid element with phase shift $k\triangle z = \pi$ is displaced outwards. Now consider the plane view in the right panel of Fig. 1.3. The two mass points, having the same radius at different heights initially, are displaced to two new separated orbits due to the perturbation. The magnetic field in the figure is taken to be a massless spring, which connects these two mass points. If the inner particle is rotating faster than the outer particle, which is the case in the Keplerian disks, the string stretches and tension builds up. The tension pulls the inner particle backward and pushes the outer particle forward. Therefore some angular momentum is transported from the inner particle to the outer particle. The inner particle cannot stay on the orbit and must drop down to an orbit with a smaller radius and therefore

smaller angular momentum. At the same time the outer particle must shift to an orbit with a larger radius and therefore larger angular momentum. The spring stretches even further and a run-away process commences. This process is the essence of MRI.

It is essential for the magnetic field to be weak. If the magnetic field is strong enough that the Alfvén time is smaller than the orbit time, the instability does not grow. The above analysis also implies the system would be stable if

$$\frac{d\Omega^2}{d\ln r} > 0\,. \tag{1.10}$$

Except for some anomalous regions, Eq. 1.10 is not satisfied in almost all astrophysical disks.

In highly conducting disks the maximum growth rate is [33]:

$$|\omega| = -\frac{1}{2}\frac{d\Omega}{d\ln r}\,. \tag{1.11}$$

It is surprisingly independent of the magnetic field and is recognized as the local Oort A-value of the disk [33]. It turns out to be $3/4\Omega$ for a Keplerian rotation. A disk without any magnetic field or with a strong field is locally stable. However, any weak poloidal magnetic field will ignite the instability with a maximum growth rate independent of the field. This maximum growth rate is found to be the maximum possible related to the differential rotation of the disk [33].

1.4 Taylor-Couette Flow

The history of Taylor-Couette Flow dates back to the 19th century. Intending to measure viscosity, Couette (1890) first tried to study flows between rotating concentric cylinders. Rayleigh's criterion (discussed below) was introduced in 1916 during his study of cyclones. Taylor (1923) extended it by including viscosity, leading to quanti-

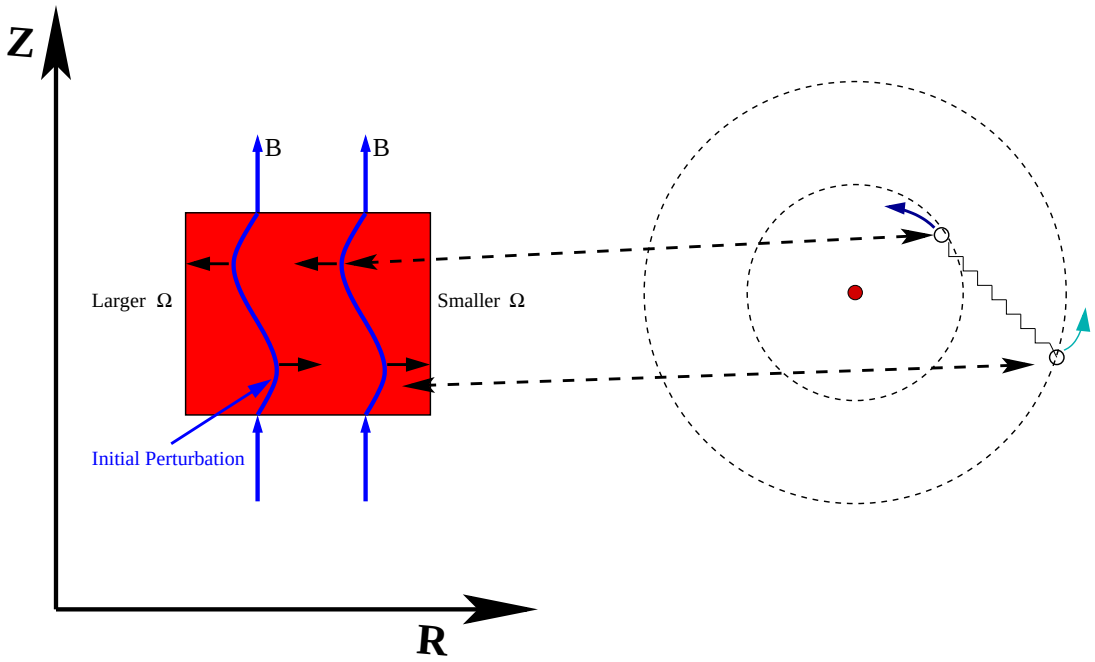

Figure 1.3: Diagram of the simple mechanism of MRI; the left figure is a side-view figure while the right one is a top-view figure. Initially there is a constant vertical magnetic field in the system. After one initial perturbation, some particle are kicked inside while other particles are kicked outside.

tative predictions of instability in Couette flow (Taylor number: Ta was named after him). Fig. 1.4 provides a brief idea of what Taylor-Couette flow is. If in Fig. 1.4 the cylinders were infinitely long—very easy to assume theoretically, but rather more difficult to build experimentally—the steady-state laminar solution would be ideal Taylor-Couette state:

$$\Omega(r) = a + \frac{b}{r^2}\,, \tag{1.12}$$

where $a = (\Omega_2 r_2^2 - \Omega_1 r_1^2)/(r_2^2 - r_1^2)$ and $b = r_1^2 r_2^2(\Omega_1 - \Omega_2)/(r_2^2 - r_1^2)$. Rayleigh's criterion suggests that in the unmagnetized and inviscid limit, such a flow is linearly axisymmetric stable if and only if the specific angular momentum increases outwards: that is, $(\Omega_1 r_1^2)^2 < (\Omega_2 r_2^2)^2$, or equivalently, $ab > 0$.

The study of the magnetized Taylor-Couette flow is much later. As mentioned before, Velikhov [28] and Chandrasekhar [29] discovered ideal MRI in the context of magnetized Couette flow. Chandrasekhar (1961) [34] also analyzed *dissipative* magnetized Couette flow. He concentrated on magnetic stabilization of Rayleigh-unstable flows: the critical Ta increases with B or Chandrasekhar number $Q \propto B^2$. On the other hand, a vertical magnetic field may destabilize the flow, provided that the angular *velocity* decreases outward, $\Omega_2^2 < \Omega_1^2$. In ideal MHD, the instability takes place with a arbitrarily weak field [6]. A number of experiments on magnetized Couette flow [35–38] have been performed, but MRI has never been conclusively demonstrated in the laboratory. Recently Sisan *et al* [39] claimed to have observed MRI for the first time in the laboratory. However, their experiment proceeded from a background state that was already hydrodynamically turbulent before the field was applied. Stefani *et al* also asserted that they have found the so called Helical MRI [40, 41] (discussed in §1.7 and more details in Chapter.4 and Chapter.5) in the laboratory [42–44]. However we challenge their arguments [45] and show that the traveling wave patterns observed in their experiment turn out to be transiently amplified disturbances launched by viscous boundary layers rather than globally unstable magnetorotational modes [46].

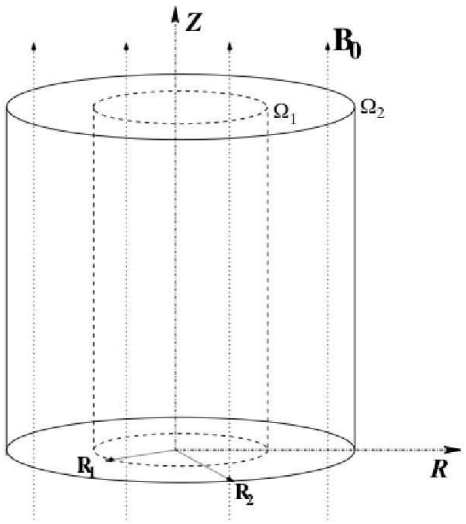

Figure 1.4: Diagram of Taylor-Couette Flow.

1.4.1 End Effects: Ekman Circulation

Taylor-Proudman Theorem

In fluid mechanics, the Taylor-Proudman theorem (after G. I. Taylor and Joseph Proudman) claims that in a incompressible fluid when a fluid element moves slowly in a co-rotating frame rotating with a large Ω, the fluid velocity is uniform in the direction of the axis of rotation. Ω must be much larger than the movement of the fluid element so that the Coriolis force dominates the inertial terms. Considering the inviscid Navier Stokes equations in a steady state, we get:

$$\rho(\vec{v}\cdot\nabla)\vec{v} = -2\rho\vec{\Omega}\times\vec{v} - \nabla P\,, \tag{1.13}$$

where $\vec{v}$ is the fluid velocity, ρ is the fluid density and $P = p + \rho\Phi$ is the effective pressure (p is the fluid pressure and Φ is the gravitational potential). If the Rossby

number is much smaller than unity, the advective terms may be unimportant. Thus,

$$2\rho\vec{\Omega} \times \vec{v} = -\nabla P \,, \tag{1.14}$$

where $\vec{\Omega}$ is the angular velocity vector. By taking the curl of this equation, we get the Taylor-Proudman theorem:

$$(\vec{\Omega} \cdot \nabla)\vec{v} = 0 \,. \tag{1.15}$$

Note that the condition $\nabla \cdot \vec{\Omega} = 0$ is used. Given coordinates in which $\Omega_r = \Omega_\varphi = 0$ and $\Omega_z \neq 0$, the equations are simplified to:

$$\frac{\partial \vec{v}}{\partial z} = 0 \,,$$

which implies that *all three* components of the velocity are independent of z.

It is followed by $\vec{\Omega}\cdot$ Eq. 1.14:

$$(\vec{\Omega} \cdot \nabla)P = 0 \,.$$

This implicates that the effective pressure is also independent of the height z. However in a real laboratory Taylor-Couette experiment (such as our experiment), some kind of confining walls (end caps) must be present. This causes the Ekman layer, which modifies the global poloidal circulation in the bulk via the Ekman suction. In the interior of the fluid the radial force balance determines the radial equilibrium effective pressure P (blue square of the right bottom part of left panel of Fig. 1.5). However, the liquid is at rest at the end plate due to the no-slip boundary condition in the co-rotating frame. The gradient of P becomes uncompensated unless the boundary co-rotates with the interior fluid. A radial flow near the end plate results from this

unbalance and is directed inward in our case (purple arrows of the right panel of Fig. 1.5, the direction of the Ekman flow actually depends upon the angular velocity of the boundary relative to the interior). After turning vertically along the inner cylinder, these two inward flows converge at the mid plane and then depart toward the outer boundary in a radial jet (blue rectangle of the right panel of Fig. 1.5) to complete the circulation (purple circulation of the left panel of Fig. 1.5). The width of the boundary layers (including the jet) depends on Re. Higher Re causes thinner boundary layers [47].

Given an infinitesimal differential rotation, the Ekman layer thickness is $\delta_E = \sqrt{\nu/\Omega}$, where ν is the kinematic viscosity. However, our experiment has a finite differential rotation. It is more appropriate to estimate δ_E via the epicyclic frquency,

$$\kappa = \left(\frac{1}{r^3} \frac{\partial J^2}{\partial r} \right)^{1/2} , \tag{1.16}$$

which is the maximum frequency of small axisymmetric inertial oscillations inside the inviscid fluid. Hence δ_E represents inertial forces balanced by viscous ones. In rigid rotation κ equals to 2Ω. Therefore we define $\delta_E = \sqrt{2\nu/\bar{\kappa}}$, where $\bar{\kappa}$ is the characteristic value for κ expressed as:

$$\bar{\kappa} = 2 \left(\frac{r_2^4 \Omega_2^2 - r_1^4 \Omega_1^2}{r_2^4 - r_1^4} \right)^{1/2} . \tag{1.17}$$

The corresponding time scale is the Ekman time, on order of $h/(\nu\bar{\kappa})^{1/2}$.

Novel method to reduce the Ekman Circulation

The poloidal circulation, and especially the jet, transport angular momentum efficiently and reduce the free energy available for shear-driven instabilities [47] (the blue symbols of Figure. 1.6 deviate significantly from the ideal Couette state.). Therefore, we will need to minimize this circulation in the MRI experiment.

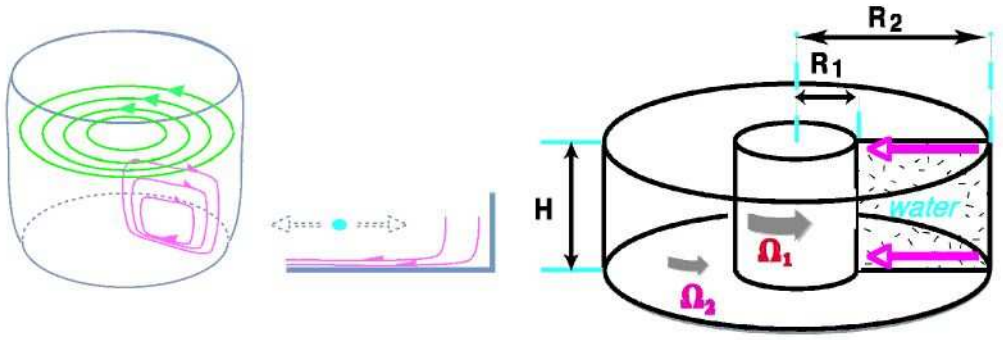

Figure 1.5: Figure courtesy of Akira Kageyama. Diagram of Ekman Circulation.

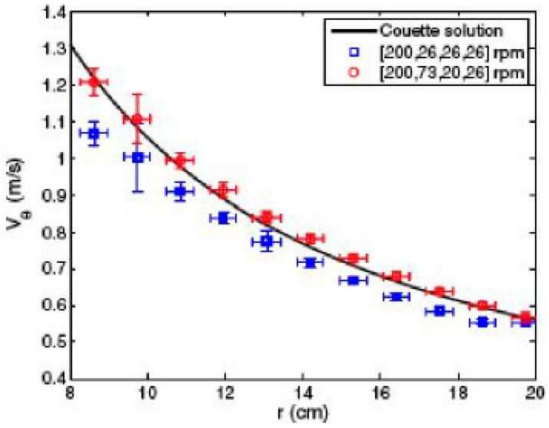

Figure 1.6: Figure courtesy of Burin et al. Azimuthal velocity v_φ *vs.* radius r. The solid line indicates the ideal Couette state; the blue symbols indicate the experiment data without any rings while the red symbols indicate the experiment data with two differentially rotating rings.

At least two methods have been previously used to reduce the effects of the end caps. One method is to use a tapered section [48]. Another one is to divide the cap into two parts: the inner one fixed to the inner cylinder, and the outer one fixed to the outer cylinder as in Richard [21] and in Wendt [18]. Here we divide the endcaps into several rings that rotate independently and differentially (Figure. 1.7).

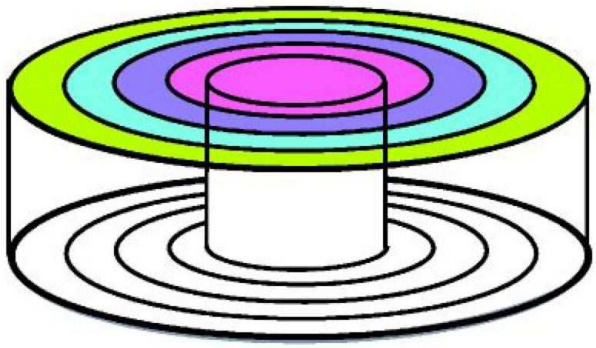

Figure 1.7: Figure courtesy of Akira Kageyama. Design with split rings to remove the Ekman Circulation.

In order to minimize the engineering challenges yet to control the flow profile as much as possible, we divide the end caps into only two rings in our experiment but the rings are not fixed to the cylinders as in Richard [21] and Wendt [18]. The simulation [47] and the experimental data (the red symbols of Fig. 1.6) [49] show that, though the rotation profile of the end caps is not the one specified in the simulation (This difference of the rotation profile at the end caps between in the experiment and in the simulation could possibly be explained by the wobbling of the inner cylinder in the experimental runs due to the difficulties of aligning the inner cylinder perfectly and non-smooth enough surfaces of the boundary walls), after the end caps are split into only two rings, the flow profile at the mid-plane is quite close to the ideal Circular Couette state.

Hollerbach and Fournier [50] cast doubts on our approach to reduce the Ekman circulation by stating that in a steady rotating fluid, the jump of the rotation speed

at the junction of the end cap rings extends deep into the bulk given a high Re. This develops a *Stewartson layer* [51]. However this effect is found not to be severe in our measurement (the red symbols of Fig. 1.6) as they claim. The azimuthal velocity profile is quite smooth; no obvious Stewartson layer is observed. This difference could be explained by an unstable Stewartson layer. The outer ring rotates more slowly than the inner one ($\Omega_4 < \Omega_3$), hence $\partial(r^2\Omega^2)/\partial r < 0$ across the joint, which could result in the *Kelvin-Helmholtz instability*. Also the *Rayleigh's centrifugal instability* may take place at sufficiently high Reynolds number since $\partial(r^2\Omega)/\partial r < 0$. The layer may be smoothed by localized circulation and/or turbulence from these instabilities. More details are discussed in §6.4.

1.5 Princeton MRI Experiment

Although its existence and importance are now accepted by most astrophysicists, MRI has yet to be clearly demonstrated in the laboratory. Recently[52, 53], we have proposed an experimental study of MRI using a magnetized Couette flow: that is, a conducting liquid (gallium) bounded by concentric differentially rotating cylinders and subject to an axial magnetic field. The radii of the cylinders are $r_1 < r_2$, as shown in Fig. 1.8; their angular velocities, Ω_1 & Ω_2, have the same sign in all cases of interest to us.

The challenge for experimentation, however, is that liquid-metal flows are very far from ideal on laboratory scales. While the fluid Reynolds number $Re \equiv \Omega_1 r_1 (r_2 - r_1)/\nu \approx 10^7$ can be large, the corresponding *magnetic* Reynolds number

$$Re_m \equiv \frac{\Omega_1 r_1 (r_2 - r_1)}{\eta} \approx 20\,, \tag{1.18}$$

is modest or small, because the magnetic Prandtl number $Pr_{\rm m} \equiv \nu/\eta \sim 10^{-6}$ in liquid metals. Standard MRI modes will not grow unless both the rotation period

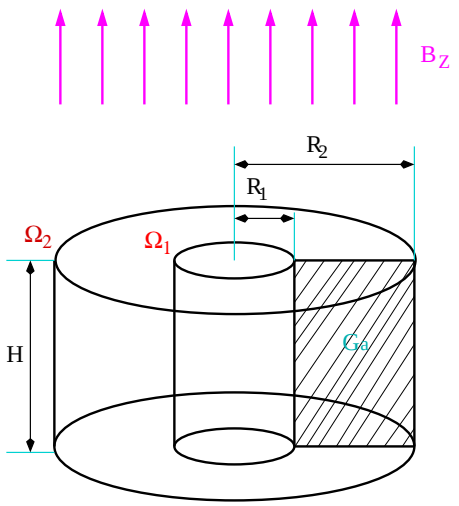

Figure 1.8: Geometry of Taylor-Couette flow. In the Princeton MRI experiment, $r_1 = 7.1\,\mathrm{cm}$, $r_2 = 20.3\,\mathrm{cm}$, $h = 27.9\,\mathrm{cm}$. $B_z \approx 5000$ Gauss and 100% run: $\Omega_1/2\pi = 4000$ rpm, $\Omega_2/2\pi = 533$ rpm.

and the Alfvén crossing time are shorter than the timescale for magnetic diffusion. This requires both $Re_m \gtrsim 1$ and $S \gtrsim 1$, where

$$S \equiv \frac{V_A(r_2 - r_1)}{\eta} \approx 4\,, \tag{1.19}$$

is the Lundquist number, and $V_A = B/\sqrt{4\pi\rho}$ is the Alfvén speed. Therefore, $Re \gtrsim 10^6$ and fields of several kilogauss must be achieved in typical experimental geometries.

Considering the aforementioned redistributing effects of the Ekman circulation (§1.4.1) and guided by the work of Kageyama *et al* [47], we have constructed a modified Taylor-Couette device having the proposed intermediary end-rings [49]. A schematic of our experimental apparatus may be seen in Fig. 1.9. The apparatus is a Taylor-Couette device with two intermediary end-rings at both end caps between the inner and outer cylinders. The details about the apparatus could be found in Burin et al. [49]. For the future gallium experiments, the outer cylinder will be composed of stainless steel.

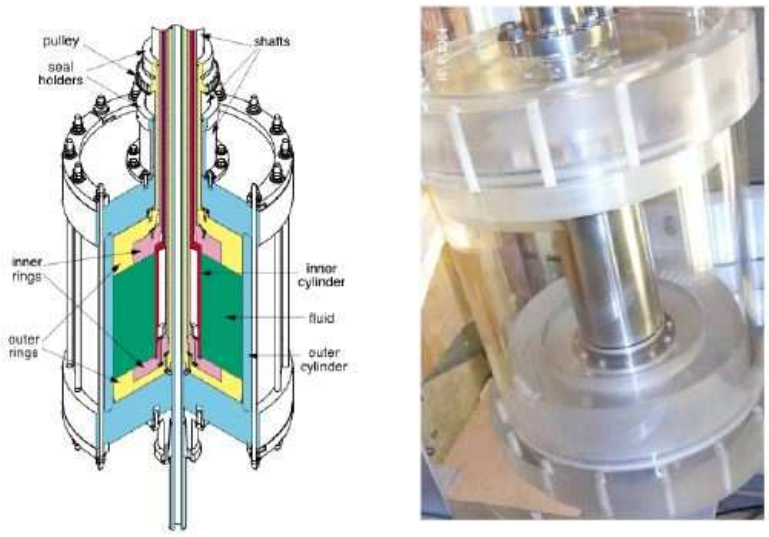

Figure 1.9: Figure courtesy of Ji et al. Apparatus of the Princeton MRI experiment.

1.6 Difference of MRI between in the lab and in the real disks

1.6.1 Ideal MRI *versus* non-ideal MRI

Given the magnetic Reynolds numbers Re_m and Lundquist numbers S are on the order of unity, our experiment is thought to be quite resistive. This is unlike fully ionized accretion disks, which are taken as nearly ideal fluids (or rather plasmas) since the astrophysical scales are enormous (Table. 1.1). Hence the turbulence in real astrophysical disks differs considerably from that in the lab. On the other hand, cool disks are so weakly ionized that the resistivity is enhanced by ion-neutral collisions and MRI may be suppressed, for example, in the quiescent states of cataclysmic variables [54] and highly possibly in protostellar disks where the exact source of the conductivity in protostellar disks is still unclear due to dust grains [55–58]. Our experiment provides a platform to study the turbulence of such cool and resistive

disks, and is most applicable to those with an externally sustained magnetic field (We know that the inner parts of many protostars could be threaded by their own strong dipole fields.).

1.6.2 Compressible MHD *versus* incompressible MHD

Our experimental regime is of course incompressible while in accretion disks the system is compressible and the shear is quite supersonic. This seems to make our experiment fundementally different from the real disks. Generally speaking *linear* MRI is constructed on incompressible fluid, especially with a weak field. In a ideal flow, the wavelength of the largest growing linear modes is $\sim V_A/\Omega$, where V_A is the Alfvén speed. If the magnetic field is so weak that the Alfvén speed is much smaller than the sound speed V_s, the system already undergoes strongly nonlinear behavior even though the flows are still very subsonic and incompressible. However, some people raised concerns upon the above logic considering that at saturation the field is amplified by MRI-driven turbulence and the Alfvén speed based on the perturbed magnetic field is about a fixed portion of the sound speed rather than the Alfvén speed based on the initial vertical magnetic field, *i.e.* $\langle V_A^2 \rangle^{1/2} \sim 0.1 V_s$ [7, 8, 59–62]. The explicit numerical algorithms used in those simulations restrict the initial V_A/V_s to $\gtrsim 0.01$ due to numerical stability and resolution, especially in three dimensional calculations. The purely incompressible nature of MRI may limit the very weak initial field, especially in a resistive flow, and therefore result in a field comparable to its initial strength $V_{A,sat}/V_{A,0} = constant$ rather than $V_{A,sat}/V_s = constant$ at saturation. Thus our experiment provides an opportunity to study MRI saturation in a truly incompressible system.

1.6.3 Plasma β_{plasma}

It is interesting to derive the relationship between the ratio $\lambda_{crit}/2H$ (where λ_{crit} is the critical wave length for MRI and $H = V_s/\Omega$ is the half disk thickness) and the magnetic field strength. For a thin isothermal Keplerian disk we have [6]

$$\frac{V_{A,z}}{V_s} = \frac{\sqrt{6}}{\pi}\frac{\lambda_{crit}}{2H}\,, \tag{1.20}$$

or alternatively in terms of the plasma parameter $\beta \equiv 8\pi\rho V_s^2/B_z^2$,

$$\beta_{plasma} = \frac{\pi^2}{3}\left(\frac{\lambda_{crit}}{2H}\right)^{-2}\,. \tag{1.21}$$

Thus the instability is supposed to be suppressed if the plasma parameter β is smaller than ~ 3.

1.6.4 Kinetic MRI

The collision-less nature of radiatively inefficient accretion flows (RIAFs) (the Coulomb collision time of RIAFs is much longer than the accretion time), like the one around the super massive black hole in the center of our Galaxy, makes kinetic effects important. We should use the Vlasov equation [63] which describes the time evolution of the distribution function of a plasma in a 6-D phase space. If the scales of interest are much larger than the ion Larmor radius, the fast gyromotion could be averaged to get the drift kinetic equation (DKE) [64, 65] in a 5-D phase space. The most important difference between collisionless and collisional plasmas is that the pressure is anisotropic with respect to the magnetic field, and there is rapid thermal conduction along the the field lines. Quataert *et al* [66–68] studied MRI in this regime using a so-called Braginskii MHD method. However the liquid metal (gallium or sodium) used in the laboratory is very collisional since the mean free path is much shorter

than the length dimension of the experiment. Hence the MHD formalism based on a simple fluid model is expected to be sufficient Princeton MRI experiment.

Parameters	Hot Disk	Cold Disk	Experiment
Reynolds Number Re	$> 10^{10}$	$> 10^{12}$	$\sim 10^7$
Magnetic Reynolds Number Re_m	$> 10^{18}$	$\lesssim 1$	20
Magnetic Prandtl Number Pr_m	$\sim 10^7$	$< 10^{-8}$	$\sim 10^{-6}$
Plasma $\beta = 8\pi P_{gas}/B^2$	$\sim 10^2$	$\sim 10^3(?)$	$\sim 10^3$

Table 1.1: Parameters in astrophysical disks

1.7 Other on-going experiments

Here we comment on the other related experiments.

A sodium experiment with a similar Couette geometry is on-going [69]. Its magnetic Reynolds number and Lundquist number are larger than ours. However, since the end plates corotate with the outer cylinder, the Ekman circulation is not avoidable, leading to a poorly controlled background toroidal flow.

MRI has already been claimed to be observed in an sodium experiment in spherical geometry [39]. The stationary outer sphere would cause the flow axisymmetrically unstable, even before the poloidal magnetic field is imposed. The angular velocity is not constant along the field line, which is different from in the accretion disks and is in contrast to our design. Thus according to Ferraro's law no laminar steady-state, from which MRI could grow, is available. Though the angular-momentum transport is found to be enhanced with the increased magnetic field, the magnetic modes they observe are non-axis-symmetric, which is not consistent with the theoretical basic of the MRI that the primary modes should be axis-symmetric if only a poloidal field is applied. Jeremy Goodman has an analytic calculation (unpublished), which demonstrates that the attachment of the poloidal field lines to the inner (Copper) sphere would lead to a torque, which is already several times larger than the one

reported by Sisan et al. [39] and claimed to be from MRI, by magnetically coupling the fluid near the rotation axis to the inner Copper sphere even if the sodium is set to be at rest. This is because the experiment was originally designed to study planetary dynamos not MRI. The results are not directly related to MRI though they are interesting and potentially important.

One of the variants of MRI, so-called "Helical" MRI (HMRI) is discovered to grow at much reduced Re_m and S in the presence of a helical background field, a current-free combination of axial and toroidal field and thus it is thought to be easier to realize experimentally than standard MRI [40, 41]. Recently it has been reported to be observed in Posdam Rossendorf Magnetic Instability Experiment (PROMISE) [42–44]. Though we confirm their results: in infinitely long or periodic cylinders the instability survives in an inviscid fluid with arbitrarily large resistivity and the thresholds of the onset of the instability is lowered significantly, the growth rate is found to be on order of $O(\eta^{-1})$. We also doubt the relevance of this new mode to the astrophysical disks and find it less attractive for experiments. More details are in Chap. 4 and Chap. 5.

In all experiments above, the plasma or the liquid metal is rotated by rotating cylinders except Sisan et al. [39], in which the liquid metal is rotated by rotating the inner sphere but still suffers the same disadvantage mentioned below. This simple design has its disadvantages. The main one is that the equilibrium flow is controlled almost entirely by the endcaps of the vessel. Another way to rotate a liquid metal is to use the Lorentz force by applying a radial electric current between cylinders in a vertical magnetic field [70–72]. Under this set-up Hartmann layers (its thickness scales as $1/Ha$, where the Hartmann number $Ha = V_A L/\sqrt{\nu\eta}$. Va_A is the Alfvén speed, L is the characteristic length, ν is the kinetic viscosity and η is the magnetic diffusivity) and a parallel layer along the cylinder surfaces (its thickness scales as $1/\sqrt{Ha}$) need to be accounted for. With large Hartmann number (Ha) they are very

small, so that the flow in the bulk is not affected. The experimental device adopting this idea proposed by Velikhov is being built in Russian Research Center "Kurchatov Institute". However some physicists raised concerns on this strategy, noting that such a system is not current-free. Therefore the possibility of current-driven instability and the likely convection due to the Ohm heating both complicate the problem.

1.8 Outline of the following chapters

The main body of the thesis (Chapter. 2 - 6) is based on five papers (published or in preparation). The first is on linear MRI and its nonlinear saturation in a periodic cylinder; the second on the Princeton MRI Experiment; the third on Helical MRI with vertically periodic boundary as well as vertically insulating end caps; the fourth on the PROMISE Experiment with partially conducting boundary condition (Copper vessel considered); the last on magnetized Ekman layer and Stewartson layer with insulating end plates.

Chapter 2, based on [73], describes linear MRI, which serves as a benchmark of the code, and its nonlinear saturation with vertically periodic boundary conditions. We present non-ideal two-dimensional magnetohydrodynamic simulations of the nonlinear evolution of MRI in the experimental geometry. The simulations adopt initially uniform vertical magnetic fields, conducting radial boundaries, and periodic vertical boundary conditions. No-slip conditions are imposed at the cylinders. Our linear growth rates compare well with existing local and global linear analyses. MRI saturates nonlinearly with horizontal magnetic fields comparable to the initial axial field. The rate of angular momentum transport increases modestly but measurably over the initial state. For modest fluid and magnetic Reynolds numbers $Re, Re_m \sim 10^2 - 10^3$, the final state is laminar reduced mean shear except near the radial boundaries, and with poloidal circulation scaling as the square root of resistivity, in partial agreement

with the analysis of Knobloch and Julien [74]. A sequence of simulations at $Re_m = 20$ and $10^2 \lesssim Re \lesssim 10^{4.4}$ enables extrapolation to the experimental regime ($Re_m \approx 20$, $Re \sim 10^7$), albeit with unrealistic boundary conditions. MRI should increase the experimentally measured torque substantially over its initial purely hydrodynamic value.

Chaper 3, based on [75], describes the simulation of Princeton MRI Experiment. We implement the fully insulating boundary condition. The simulations mimic the on-going experiment except that the conductivity of the stainless steel walls is neglected and the simulation starts from an ideal Couette state rather than an actual hydrodynamical equilibrium with split end caps. We have also restricted our study to smaller fluid Reynolds number (Re) than in the experiment, but have used exactly the same magnetic Reynolds number (Re_m). MRI grows from small amplitudes at a rate in good agreement with linear analysis. A clear linear phase is observed. MRI saturates nonlinearly with horizontal magnetic fields as large as several percent of the initial axial field. Surprisingly one inflowing "jet" opposite to the usual Ekman circulation "jet" is found near the inner cylinder. Under the proper conditions, our experimental facility is a good platform to show that MRI could be suppressed by a strong magnetic field. The MRI enhances the angular momentum transport at saturation. We also study the effect of the partially conducting stainless steel walls and start the simulation from a hydrodynamic equilibrium state with an adjusted rotation profile in order to recover the linear phase. The influences from these two complications are minimal and some similar conclusions are achieved.

Chaper 4, based on [45], describes Helical MRI studies with both vertically periodic boundary condition and insulating end caps. We confirm the results of Hollerbach and Rüdiger [40], Rüdiger et al. [41] , calculate HMRI growth rates, and show that in the resistive limit, HMRI is a weakly destabilized inertial oscillation propagating in a unique direction along the axis. But we report other features of HMRI that make

it less feasible for experiments and for resistive astrophysical disks. Growth rates are small and require large axial currents. More fundamentally, instability of highly resistive flows is particular to infinitely long or periodic cylinders: finite cylinders with insulating endcaps are shown to be stable in this limit. Also, Keplerian rotation profiles are stable in the resistive limit regardless of axial boundary conditions. Nevertheless, the addition of toroidal field lowers thresholds for instability even in finite cylinders.

Chaper 5, based on [46], describes the simulation of Germany PROMISE Experiment with partially conducting boundary condition (Copper walls considered). We investigate numerically a traveling wave pattern observed in experimental magnetized Taylor-Couette flow at low magnetic Reynolds number. By accurately modeling viscous and magnetic boundaries in all directions, we reproduce the experimentally measured wave patterns and their amplitudes. Contrary to previous claims that the wave patterns are due to Helical MRI, a global instability [42–44], the waves are shown to be transiently amplified disturbances launched by viscous boundary layers rather than globally unstable magnetorotational modes.

Chaper 6, based on [76], describes the studies of magnetized Ekman layer and Stewartson layer. The magnetic field is found to inhibit the Ekman suction. While we quantitatively confirmed the conclusions of Gilman *et al* [77–81], the finite differential rotation cannot be neglected and modifies the linear Ekman layer. The width of the Ekman layer is reduced with an increased magnetic field normal to the end plate. A uniformly-rotating region forms near the outer cylinder. The Stewartson layer [51] penetrates deeper into the fluid with larger Reynolds number and stronger magnetic field. Furthermore a strong magnetic field leads to a steady Stewartson layer, at least in axisymmetry.

Main conclusions and future work are summarized in Chap. 7.

Appendix A contains the new physics and all the boundary conditions imple-

mented in ZEUS. Viscosity and resistivity have been incorporated into the code and the code is transformed to a flux-conservative form to conserve the angular momentum exactly since the angular momentum is the key issue in our project. Also no-slip hydrodynamic boundary condition is implemented. The technical details of how to implement (1) vertical periodic radial conducting; (2) vertical periodic radial insulating; (3) vertical insulating radial conducting; (4) fully insulating; and (5) partially conducting boundary conditions are discussed.

Appendix B contains the benchmarks against the newly added subroutine for viscosity and resistivity as well as the comparison between the ZEUS code, which is an astrophysical compressible ideal MHD code, and an incompressible code. For the viscosity, a low-Re test is performed to compare with Wendl's solution [82]. For the resistivity a Magnetic Gauss diffusion test shows that the error scales quadratically with cell size, as expected for our second-order difference scheme. All benchmarks show that the modification of ZEUS is favorable and that a supersonic ideal code could be modified to carry out subsonic diffusive simulations.

Chapter 2

MRI in Periodic Cylinders[1]

It is a good starting step to study MRI in a periodic cylinder. That is: we adopt vertically periodic boundary conditions for all fluid variables, with a periodicity length $L_z = 2h$, where $h = 27.9\,\mathrm{cm}$ is the actual height of the experimental flow. Such boundary conditions are physically unrealistic, but almost all published linear analyses of MRI in Couette flows have adopted them because they permit a complete separation of variables [52, 53, 69, 83, 84]; an exception is Rüdiger and Zhang [85]. Thus by adopting periodic vertical boundaries, we are able to test our code against well-established linear growth rates and to explore—apparently for the first time in Couette geometry—the transition from linear growth to nonlinear saturation.

One may question the relevance of experimental to astrophysical MRI, especially its nonlinear phases. In accretion disks, differential rotation arises from radial force balance between the gravitational attraction of the accreting body and centrifugal force. Thermal and magnetic energies are small compared to orbital energies, at least if the disk is vertically thin compared to its radius. Consequently, nonlinear saturation of MRI cannot occur by large-scale changes in rotation profile. In experiments, however, differential rotation is imposed by viscous or other weak forces, and the incompressiblity of the fluid and its confinement by a container allow radial force

[1] inherited and modified from Liu et al. [73]

balance for arbitrary $\Omega(r)$. Thus, saturation may occur by reduction of differential rotation, which is the source of free energy for the instability. In this respect, MRI experiments and the simulations of this chapter may have closer astrophysical counterparts among differentially rotating stars, where rotation is subsonic and boundaries are nearly stress-free [86, 87].

Both in the laboratory and in astrophysics nonlinear MRI is expected to enhance the radial transport of angular momentum. Quantifying the enhanced transport in a Couette flow is a primary goal of the Princeton MRI experiment and of the present chapter.

Most of the parameters of the simulations in §§2.1-2.2 are chosen to match those of the experiment. We adopt the same cylinder radii (Fig. 2.1). The experimental rotation rates of both cylinders (and of the endcaps) are separately adjustable, as is the axial magnetic field. For these simulations, we adopt fixed values within the achievable range: $\Omega_1 = 4000\,\mathrm{rpm}$ & $\Omega_2 = 533\,\mathrm{rpm}$, $B_{z0} = 5000\,\mathrm{G}$. We set the density of the fluid to that of gallium, $\rho = 6\,\mathrm{g\,cm^{-3}}$.

We also restrict our simulations to lower Reynolds number Re than the experimental one $\gtrsim 10^6$. Computations at $Re \gtrsim 10^6$ are out of reach of any present-day code and computer, at least in three dimensions; $Re \sim 10^6$ might just be achievable in axisymmetry, but higher-Re flows are more likely to be three-dimensional, so that an axisymmetric simulation at such a large Re is of doubtful relevance. (The same objection might be leveled at all of our simulations for $Re \gg 10^3$. Those simulations are nevertheless useful for establishing scaling relations, even if the applicability of the relations to real three-dimensional flows is open to question.) We use an artificially large kinematic viscosity so that $Re = 10^2 - 10^{4.4}$, whereas for the true kinematic viscosity of gallium ($\nu \simeq 3 \times 10^{-3}\,\mathrm{cm^2 s^{-1}}$), $Re \approx 10^7$ at the dimensions and rotation rates cited above. In defense of this approximation, we point to the fact that extrapolations of Ekman-circulation rates and rotation profiles simulated at $Re < 10^4$

agree well with measurements taken at $Re = 10^6$ both in a prototype experiment [47], and in the present aparatus [49]. We *are* able to reproduce the experimental values of the dimensionless parameters based on resistivity: $Re_m \sim 20$, $S \sim 4$; we also report simulations at $Re_m \sim 10^2 - 10^4$. (The actual diffusivity of gallium is $\eta \simeq 2 \times 10^3\,\mathrm{cm^2 s^{-1}}$).

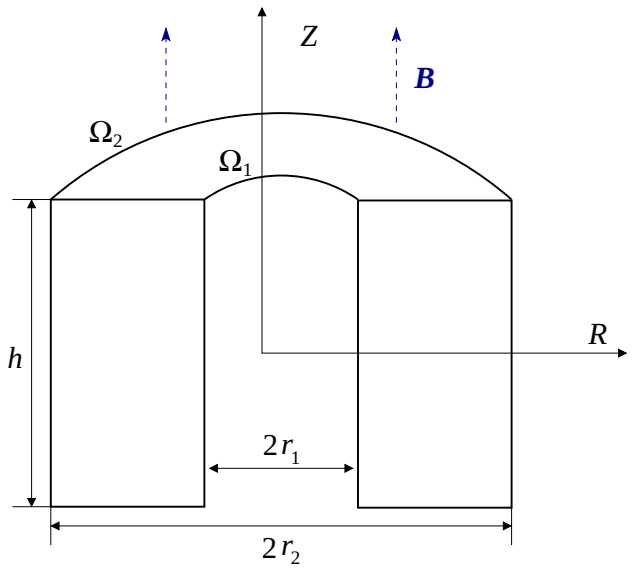

Figure 2.1: Geometry of Taylor-Couette flow. In the Princeton MRI experiment, $r_1 = 7.1\,\mathrm{cm}$, $r_2 = 20.3\,\mathrm{cm}$, $h = 27.9\,\mathrm{cm}$.

2.1 Linear MRI

In the linear regime, MRI has been extensively studied both locally and globally [52, 53, 69, 83–85]. We have used these linear results to benchmark our code.

In the linear analyses cited above, the system is assumed to be vertically periodic with periodicity length $2h$, twice the height height of the cylinders. In cylindrical coordinates, the equilibrium states are $\mathbf{B_0} = B_0\hat{\mathbf{e}}_z$ and $\mathbf{V_0} = r\Omega\hat{\mathbf{e}}_\varphi$. WKB methods describe the stability of this system very well even on the largest scales [52, 53]. Linear modes are proportional to $\exp(\gamma t - ik_z z)f(k_r r)$, where γ is the growth rate, and $f(x)$ is an approximately sinusoidal radial function, at least outside boundary layers, whose

zeros are spaced by $\Delta x \approx \pi$. The wavenumbers $k_z = n\pi/h$ and $k_r \approx m\pi/(r_2 - r_1)$, where n and m are positive integers. We will consider only the lowest value of k_r ($m = 1$) but allow $n \geq 1$. The initial perturbation is set to an approximate eigenmode appropriate for conducting boundary conditions:

$$\begin{aligned} \delta B_z &= A \sin k_z z \frac{r_1 + r_2 - 2r}{r}\,, \delta B_r = k_z A \cos k_z z \frac{(r_2 - r)(r - r_1)}{r}\,, \delta B_\varphi = 0\,, \\ \delta V_z &= B \cos k_z z \frac{r_1 + r_2 - 2r}{r}\,, \delta V_r = k_z B \sin k_z z \frac{(r_2 - r)(r - r_1)}{r}\,, \delta V_\varphi = 0. \end{aligned} \quad (2.1)$$

Evidently, the fast-growing mode dominates the simulations no matter which n is used initially. Figure 2.2 compares the MRI growth rate obtained from the simulations with those predicted by global linear analysis [53] as a function of magnetic Reynolds number.

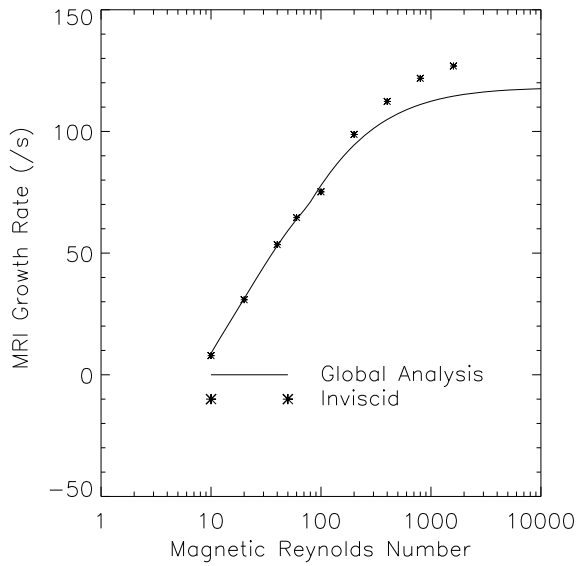

Figure 2.2: MRI growth rate versus Re_m for conducting radial boundaries. *Points:* simulations (see the comments in the main text). *Curve:* global linear analysis with $Re = 25,600$.

The radially global, vertically periodic linear analysis of Goodman and Ji [53] found that the linear eigenmodes have boundary layers that are sensitive to the dis-

sipation coefficients, but that the growth rates agree reasonably well with WKB estimates except near marginal stability. A comparison of the growth rates found by this analysis with those obtained from our simulations is given in Table 2.1. In the context of the simulations, "$Re = \infty$" means that the explicit viscosity parameter of the code was set to zero, but this does not guarantee inviscid behavior since there is generally some diffusion of angular momentum caused by finite grid resolution. Nevertheless, since the magnetic Reynolds number of the experiment will be about 20 and since $Re/Re_m \sim 10^6$, these entries of the table probably most closely approximate the degree of dissipation in the gallium experiment. In Table 2.1, the largest growth rate predicted by the linear analysis has been marked with an asterisk (*). The simulations naturally tend to be dominated by the fastest numerical mode—that is, the fastest eigenmode of the finite-difference equations, which need not map smoothly into the continuum limit. Fortunately, as asserted by the Table, the fastest growth occurs at the same vertical harmonic n in the simulations as in the linear analysis.

Re_m	Re	n	Prediction $[\mathrm{s}^{-1}]$	Simulation $[\mathrm{s}^{-1}]$
400	400	1	41.67	77.66
		2	72.71	
		3	77.69*	
		4	56.88	
		5	0.283	
20	∞	1	23.31	30.83
		2	32.43*	
		3	23.73	
		4	6.905	

Table 2.1: Growth rates from semianalytic linear analysis *vs.* simulation.

2.2 Nonlinear Saturation

As noted in the very beginning of this chapter, instabilities cannot easily modify the differential rotation of accretion disks because internal and magnetic energies are

small compared to gravitational ones, and MRI is believed to saturate by turbulent reconnection [88, 89]. In Couette flow, however, the energetics do not preclude large changes in the rotation profile. As shown by Fig. 2.3, while the differential rotation of the final state is reduced compared to the initial state in the center part of the flow, it is steepened near the inner cylinder for $|z| > 0$.

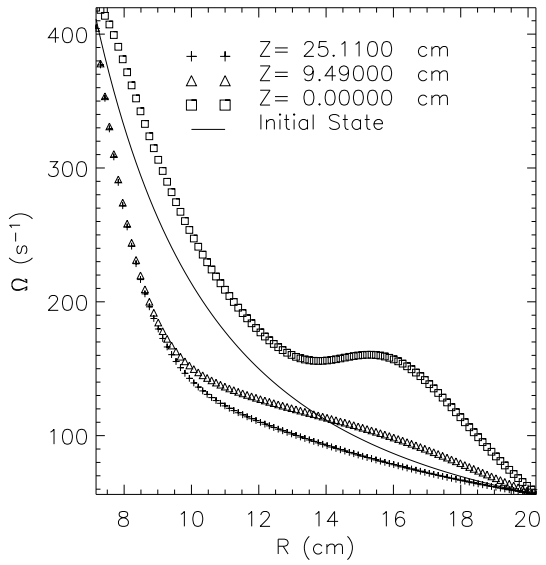

Figure 2.3: Angular velocity profile before and after saturation at several heights, for $Re = Re_m = 400$. "Jet" is centered at $z = 0$ (squares).

2.2.1 Structure of the final state

For moderate dissipation ($Re, Re_m \lesssim 10^3$), the final state is steady. Typical flow and field patterns are shown in Figure 2.4. The poloidal flux and stream functions are defined so that

$$\boldsymbol{V}_P \equiv V_r \boldsymbol{e}_r + V_z \boldsymbol{e}_z = r^{-1} \boldsymbol{e}_\varphi \times \boldsymbol{\nabla}\, \Phi, \qquad \boldsymbol{B}_P \equiv B_r \boldsymbol{e}_r + B_z \boldsymbol{e}_z = r^{-1} \boldsymbol{e}_\varphi \times \boldsymbol{\nabla}\, \Psi, \quad (2.2)$$

which imply $\boldsymbol{\nabla} \cdot \boldsymbol{V}_P = 0$ and $\boldsymbol{\nabla} \cdot \boldsymbol{B}_P = 0$. [Our velocity field is slightly compressible, so that eq. (2.2) does not quite capture the full velocity field. Nevertheless, the error is small, and Φ is well defined by $\nabla^2(\Phi \boldsymbol{e}_\varphi / r) = \boldsymbol{\nabla} \times \boldsymbol{V}_{\rm P}$ with periodic boundary conditions in z and $\partial\Phi/\partial z = 0$ on the cylinders.]

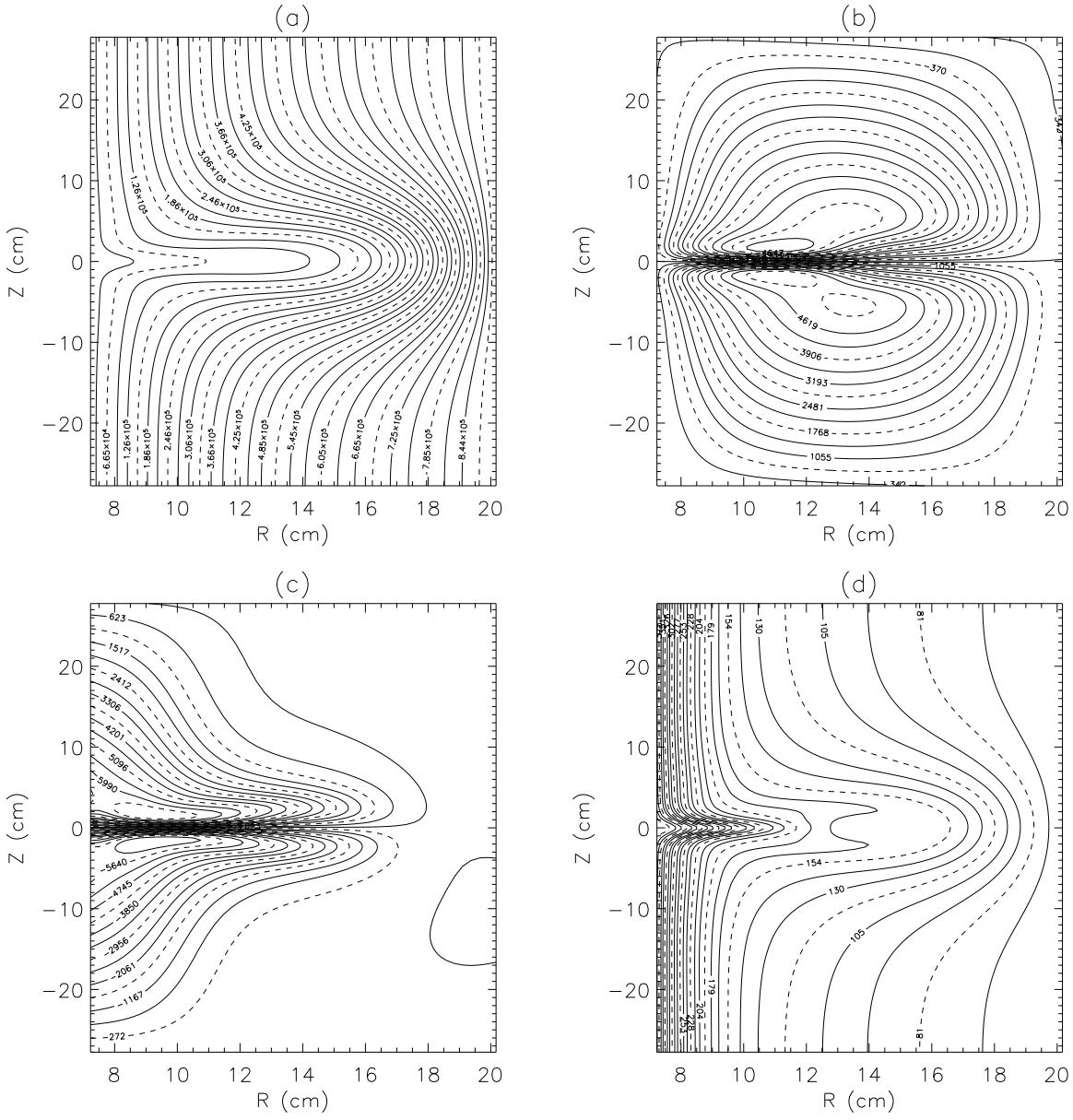

Figure 2.4: Contour plots of final-state velocities and fields. $Re = 400$, $Re_m = 400$. (a) Poloidal flux function Ψ (Gauss cm^2) (b) Poloidal stream function Φ (cm^{2}s^{-1}) (c) toroidal field B_φ (Gauss) (d) angular velocity $\Omega \equiv r^{-1} V_\varphi$ (rad s^{-1}).

The most striking feature is the outflowing "jet" centered near $z = 0$ in Figure 2.4.

The contrast in flow speed between the jet and its surroundings is shown more clearly in Figure 2.5. Figure 2.4 also shows that the horizontal magnetic field changes rapidly across the jet, which therefore approximates a current sheet.

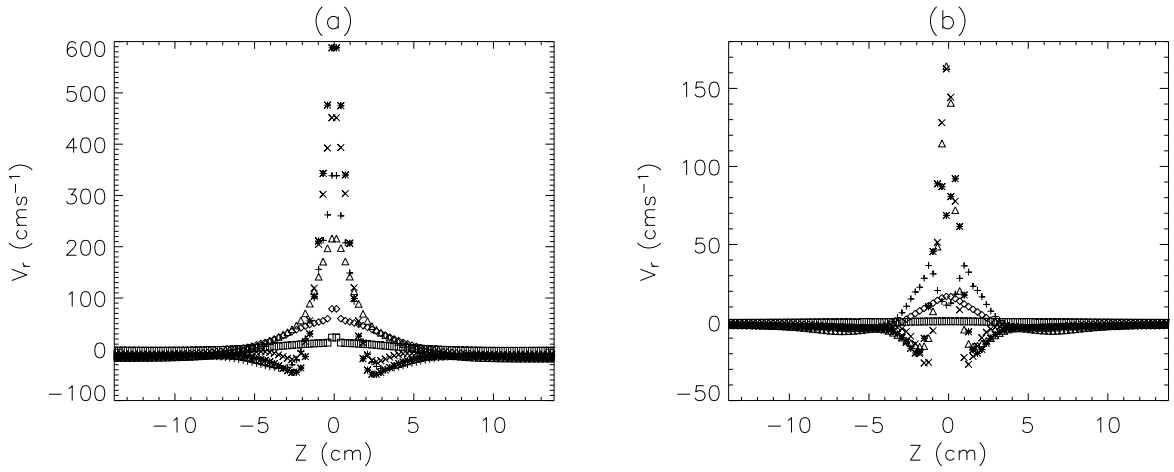

Figure 2.5: Radial velocity versus z for $Re = 400$, at several radii (cm): $+$, 8.42; $*$, 10.27; $\times$, 11.98; $\triangle$, 13.70; $\diamond$, 16.87; $\square$, 18.98. For clarity, only half the full vertical period (56 cm) is shown. Panel (a), $Re_m = 400$; panel (b) $Re_m = 6400$.

The radial flow speed in the jet scales with Re_m as (Fig. 2.6),

$$V_{\rm jet} \propto Re_m^{-0.53}. \tag{2.3}$$

We find that the radial inward speed outside the jet scales similarly,

$$V_{\rm external} \propto Re_m^{-0.56} \propto \eta^{0.56}. \tag{2.4}$$

Mass conservation demands that $V_{\rm jet} W_{\rm jet} = V_{\rm external}(2h - W_{\rm jet})$, where $W_{\rm jet}$ is the effective width of the jet. Thus we can conclude that this width is independent of magnetic Reynolds number:

$$W_{\rm jet} \propto Re_m^0 \,. \tag{2.5}$$

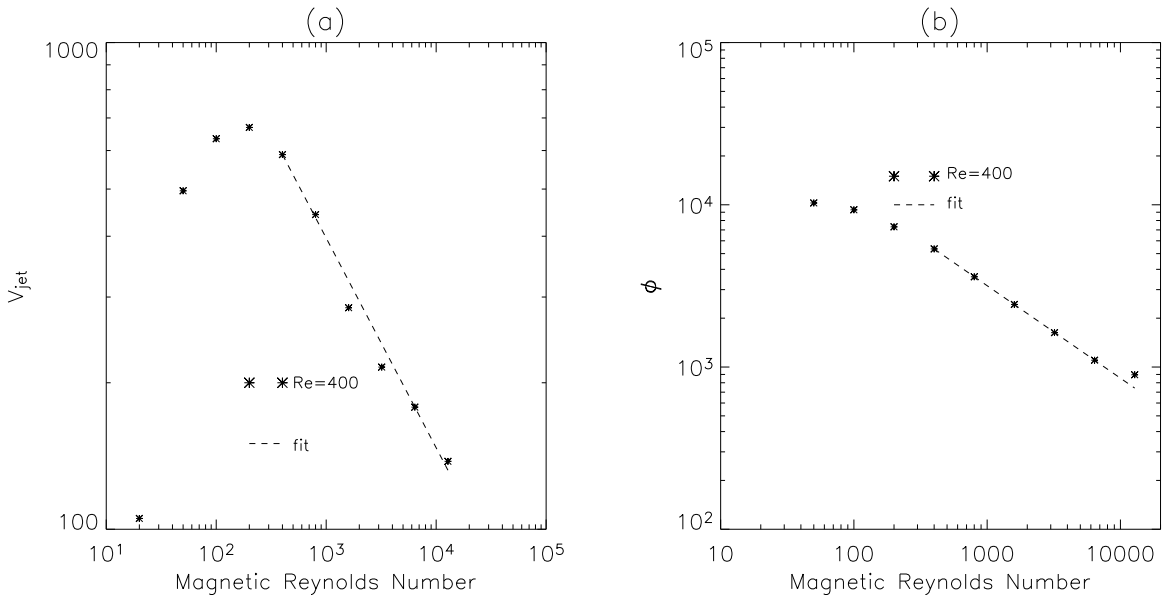

Figure 2.6: Maximum radial speed in the jet (left panel) and maximum of poloidal stream function (right panel) *vs.* magnetic Reynolds number, for $Re = 400$. Powerlaw fits are shown as dashed lines with slopes -0.53 [left panel, eq. (2.3)] and -0.57 [right panel].

Additional support for this conclusion comes from the nearly equal scaling of V_r and Φ with Re_m (Fig. 2.6), which indicates that the spatial scales in the velocity field are asymptotically independent of Re_m. The toroidal flow perturbation and toroidal field are comparable to the rotation speed and initial background field, respectively:

$$1.18 \lesssim \max \frac{B_\varphi}{B_{z0}} \lesssim 1.52, \qquad 0.28 \lesssim \max \frac{\delta V_\varphi}{r_1 \Omega_1} \lesssim 0.56\,. \tag{2.6}$$

We emphasize that the scalings (2.3)-(2.6) have been established for a limited range of flow parameters, $10^2 \lesssim Re, Re_m \lesssim 10^{4.4}$. The jet is less well defined at lower Re_m, especially in the magnetic field. Extrapolation of these scalings to laboratory Reynolds numbers ($Re \gtrsim 10^6$) is risky, and indeed our simulations suggest that the final states are unsteady at high Re and/or high Re_m (Fig. 2.7).

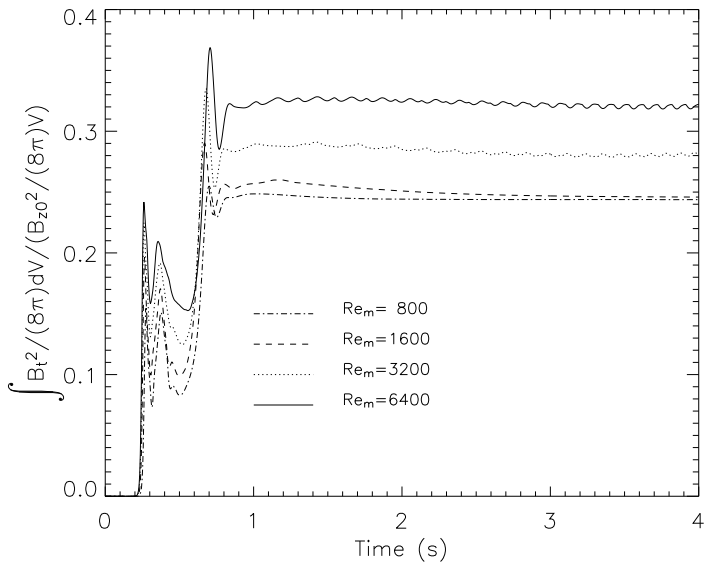

Figure 2.7: Total toroidal magnetic energy *vs.* time at $Re = 400$.

2.2.2 Angular Momentum Transport

Figure 2.8 displays the radial profiles of the advective, viscous, and magnetic torques integrated over cylinders coaxial with the boundaries:

$$\Gamma_{\rm advective}(r) = \int_{-h}^{h} dz\, \rho r^2 v_r v_\varphi \,, \tag{2.7}$$

$$\Gamma_{\rm magnetic}(r) = \int_{-h}^{h} dz \left(-\frac{r^2 B_r B_\varphi}{4\pi} \right) , \tag{2.8}$$

$$\Gamma_{\rm viscous}(r) = \int_{-h}^{h} dz \left[-r^3 \rho \nu \frac{\partial}{\partial r} \left(\frac{v_\varphi}{r} \right) \right] , \tag{2.9}$$

$$\Gamma_{\rm total}(r) = \Gamma_{\rm advective}(r) + \Gamma_{\rm magnetic}(r) + \Gamma_{\rm viscous}(r) \,. \tag{2.10}$$

The advective and magnetic torques vanish at r_1 and r_2 because of the boundary conditions but are important at intermediate radii. All components of the torque are positive except near r_2. The total torque is constant with radius, as required in steady state, but increases from the initial to the final state (Figure 2.8). From Figure 2.9,

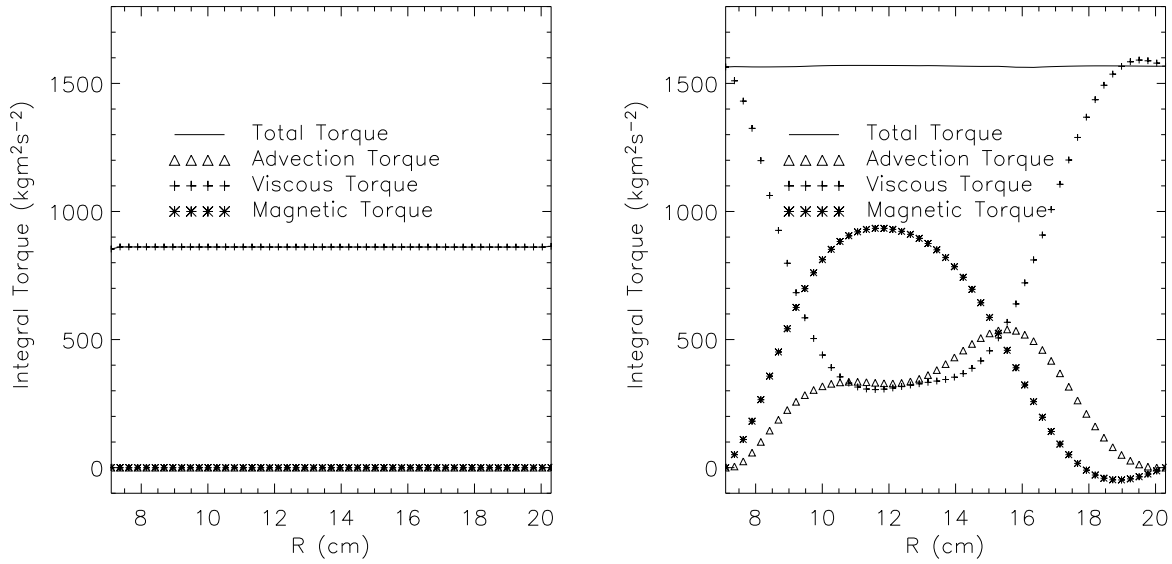

Figure 2.8: z-integrated torques versus r. $Re = 400$, $Re_m = 400$. Left panel: initial state; right: final state.

we infer the scalings

$$\frac{\Gamma_{\rm final} - \Gamma_{\rm init}}{\Gamma_{\rm init}} \propto Re^{0.5} Re_m^0, \tag{2.11}$$

at least at Re, $Re_m \gtrsim 10^3$. In fact, a better fit to the exponent of Re for $Re_m = 20$ and $Re \gtrsim 10^3$ would be 0.68 rather than 0.5, but the exponent seems to decrease at the largest Re, and it is ≈ 0.5 for $Re_m = 400$, so we take the latter to be the correct asymptotic value.

Representative runs are listed in Table 2.2. Additional runs have been carried out on coarser grids (smaller N_r, N_z) to check that the values quoted for the torques are independent of spatial resolution to at least two significant figures in the laminar cases ($Re, Re_m \lesssim 10^3$) and to better than 10% in the unsteady cases where precise averages are difficult to obtain. In the latter cases, the quoted values in the last two columns have been averaged over radius but not over time.

Re_m	Re	Resolution $N_z \times N_r$	Γ_{initial} $[\,\text{kg}\,\text{m}^2\,\text{s}^{-2}]$	Γ_{final} $[\,\text{kg}\,\text{m}^2\,\text{s}^{-2}]$	$\Delta\Gamma/\Gamma_{\text{initial}}$
10	400	200×50	8.60e2	8.60e2	0.00
20	400	200×50	8.60e2	9.02e2	0.05
50	400	200×50	8.60e2	1.12e3	0.30
100	400	200×50	8.60e2	1.35e3	0.57
200	400	200×50	8.60e2	1.50e3	0.74
400	400	200×50	8.60e2	1.57e3	0.83
800	400	200×50	8.60e2	1.57e3	0.83
1600	400	200×50	8.60e2	1.67e3	0.94
3200	400	200×50	8.60e2	1.65e3	0.92
6400	400	200×50	8.60e2	1.62e3	0.88
12800	400	228×50	8.60e2	1.62e3	0.88
400	100	200×50	3.44e3	4.45e3	0.44
400	200	200×50	1.72e3	2.58e3	0.50
400	400	200×50	8.60e2	1.57e3	0.83
400	800	200×50	4.30e2	9.70e2	1.26
400	1600	200×50	2.15e2	6.20e2	1.88
400	3200	200×50	1.08e2	3.90e2	2.63
400	6400	200×50	5.38e1	2.46e2	3.58
400	12800	228×58	2.69e1	1.55e2	4.77
20	100	200×50	3.44e3	3.44e3	0.00
20	200	200×50	1.72e3	1.72e3	0.00
20	400	200×50	8.60e2	9.02e2	0.05
20	800	200×50	4.30e2	4.95e2	0.15
20	1600	200×50	2.15e2	2.76e2	0.28
20	3200	200×50	1.08e2	1.57e2	0.45
20	6400	200×50	5.38e1	9.35e1	0.74
20	12800	228×50	2.69e1	5.75e1	1.14
20	25600	320×50	1.34e1	3.70e1	1.75

Table 2.2: Increase of total torque versus Re and Re_m.

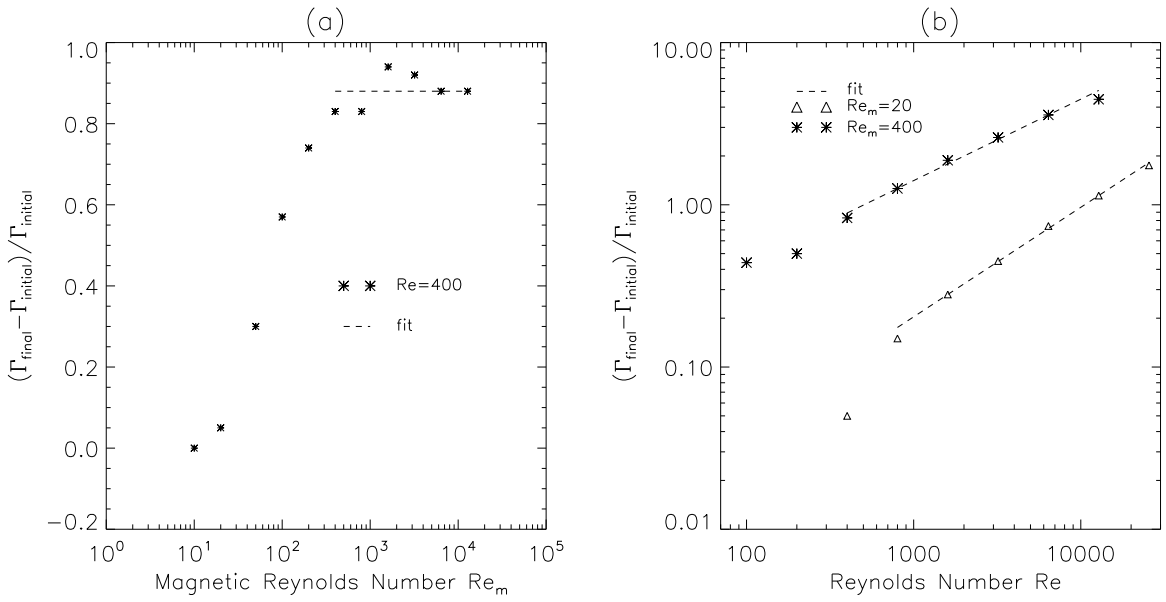

Figure 2.9: Increase of total torque versus (a) Re_m and (b) Re. In panel (b), dashed lines have slopes of 0.5 ($Re_m = 400$) and 0.675 ($Re_m = 20$).

2.2.3 Interpretation of the final state

The division of the flow into a narrow outflowing jet and a slower reflux resembles that found by Kageyama et al. [47] in their hydrodynamic simulations [Fig. B.2]. In that case, the jet bordered two Ekman cells driven by the top and bottom endcaps. In the present case, however, Ekman circulation is not expected since the vertical boundaries are periodic, and we must look elsewhere for an explanation of the final state.

Knobloch and Julien [74, hereafter KJ] have proposed that axisymmetric MRI may saturate in a laminar flow whose properties depend upon the dissipation coefficients ν & η, with a large change in the mean rotation profile, $\Omega(r)$. Although this mechanism of saturation probably cannot apply to thin disks, it is consistent with some aspects of the final state of our Couette-flow simulations: in particular, the scalings (2.3)-(2.4) of the poloidal velocities with Re_m; and the mean rotation profile does indeed undergo a large reduction in its mean shear, except near the boundaries (Fig. 2.3).

One prominent difference between the final states envisaged by KJ and those

found here is the axial lengthscale. KJ assumed the final state to have the same periodicity as the fastest-growing linear MRI mode, although they acknowledged that their theory does not require this. In our case, the linear and nonlinear lengthscales differ: whereas the fastest linear mode has three wavelengths over the length of the simulation (Table 2.1), the nonlinear state adopts the longest available periodicity length, namely that which is imposed by the vertical boundary conditions. Within that length, the flow is divided between the narrow jet and broad reflux regions. As discussed below, a third and even narrower reconnection region, whose width scales differently in Re_m from that of the jet itself, exists within the jet. Another possibly important difference concerns the role of radial boundaries. KJ simply ignored these, yet our jet clearly originates at the inner cylinder (Fig. 2.4). KJ's theory predicts that the poloidal flow should be proportional to $Re^{-1/2}$ as well as $Re_m^{-1/2}$. Yet, we find that $V_{\rm jet}$ actually *increases* with Re, roughly as $Re^{+1/2}$, up to $Re \sim 10^3$, above which it begins to decline and the flow becomes unsteady.

The jet is probably the part of the flow that corresponds most closely to the "fingers" envisaged by KJ. Let us at least try to understand how the quantities in our jet scale with increasing Re_m at fixed Re, even though it is more relevant to the experiment to increase Re at fixed and modest Re_m (for the latter, see below).

In steady state, the toroidal component of the electric field vanishes, $E_\varphi = 0$, because the flux through any circuit around the axis is constant. Consequently,

$$[\Phi, \Psi] \equiv \frac{\partial \Phi}{\partial r}\frac{\partial \Psi}{\partial z} - \frac{\partial \Phi}{\partial z}\frac{\partial \Psi}{\partial r} = \eta r \left(\frac{\partial^2}{\partial z^2} + \frac{\partial^2}{\partial r^2} - \frac{1}{r}\frac{\partial}{\partial r} \right) \Psi \equiv \eta r \Delta_* \Psi, \qquad (2.12)$$

The evidence from our simulations is that the peak values of Φ and Ψ scale as $\eta^{1/2}$ and η^0, respectively, in the nonresistive limit $\eta \to 0$, $Re_m \to \infty$. The radial velocity $V_r = r^{-1}\partial\Phi/\partial z$ also scales as $\eta^{1/2}$. In order that the two sides of eq. (2.12) balance, at least one of the derivatives of Ψ must become singular in the limit $\eta \to 0$. This

appears to be the case. In fact, a comparison of the flux contours in Figures 2.4(a) and 2.10(a) suggests that a current sheet develops at the center of the jet. This is more obvious in the horizontal components of current density, J_r and J_φ, whose peak values we find to scale as $\propto \eta^{-0.46} \approx Re_m^{1/2}$ (Figure 2.11) and the maximum toroidal magnetic field near the current sheet scales as

$$B_\varphi \propto Re_m^{0.18} \approx Re_m^{1/6}\,. \tag{2.13}$$

From these scalings one infers that the width of the current sheet scales as $\eta^{1/3}$. On the other hand, the region defined by $|B_r|, |B_\varphi| > |B_z|$ appears to have a width $\propto \eta^0$, like that of the velocity jet. We call this the magnetic "finger" because of its form in Fig. 2.10.

It is interesting to check whether these scalings are consistent with the observation that the total torque (radial angular-momentum flux) appears to be asymptotically independent of the resistivity. As $\eta \to 0$, the advective torque $\propto \int V_r V_\varphi dz$ tends to zero since $V_r \propto \eta^{1/2}$ and V_φ is presumably bounded by $\sim r\Omega_1$. The viscous contribution is always dominant near the cylinders but is reduced compared to the initial state at intermediate radii by the reduction in the vertically-averaged radial shear (Fig. 2.8). Since the total torque is larger in the final than in the initial state, a significant fraction of it must be magnetic, and this fraction should be approximately independent of η at sufficiently small η. If $B_r \sim B_\varphi \propto \eta^x$ within a vertical layer of width $\Delta z \sim \eta^y$, the torque $\propto \int B_r B_\varphi dz \propto \eta^{2x+y}$. Thus we expect $y \approx -2x$. In agreement with this, we have found that $x \approx -1/6$ and $y \approx 1/3$ in the current sheet, while in the finger, $x \approx y \approx 0$.

One notices in Fig. 2.10(a)&(d) that the angular velocity is approximately constant along field lines—$\Omega = \Omega(\Psi)$—as required by Ferraro's Law when the flow is predominantly toroidal and the resitivity small. There must therefore be an outward

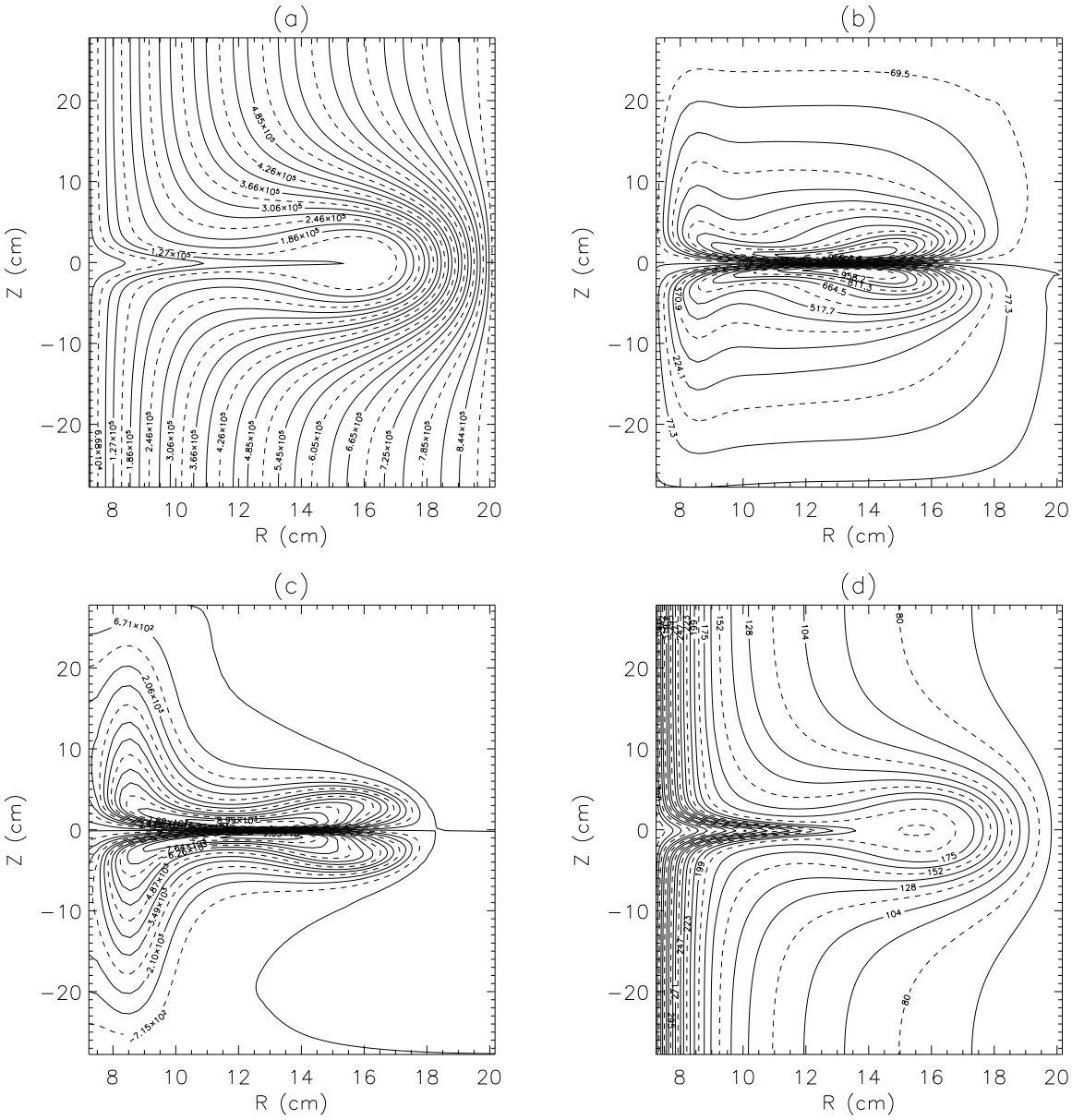

Figure 2.10: The same sequence as Fig. 2.4, but for $Re_m = 6400$, $Re = 400$. Symmetry about $z = 0$ has not been enforced; the jet forms spontaneously at $z \approx -20$, but the whole pattern has been shifted vertically to ease comparison with Fig. 2.4.

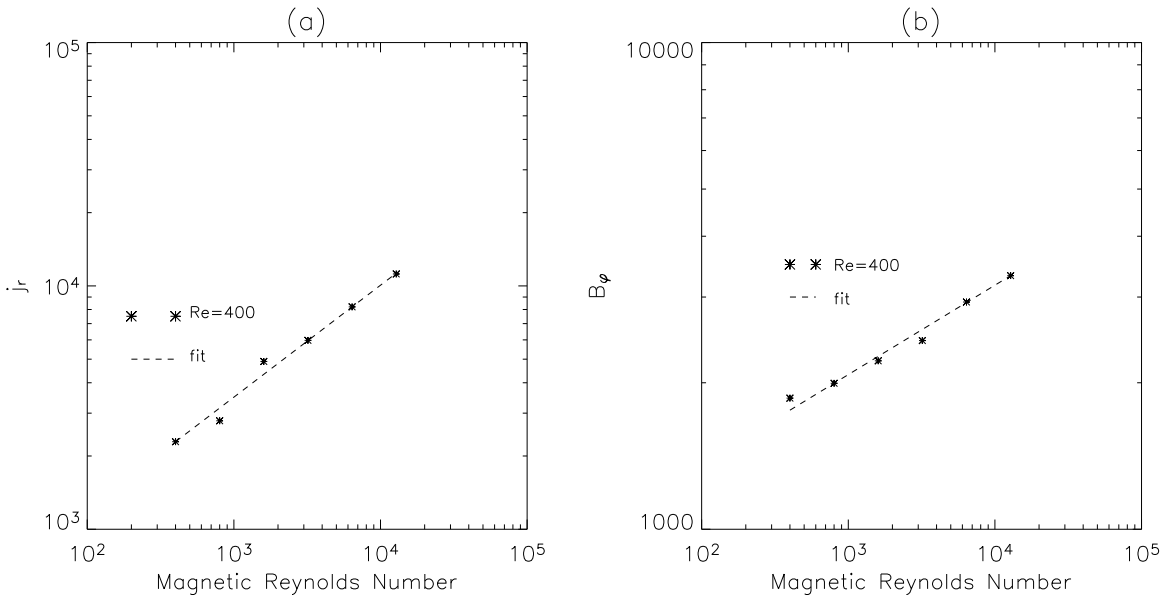

Figure 2.11: Maximum radial current in the current sheet (left panel) and maximum of toroidal magnetic field (right panel) *vs.* magnetic Reynolds number, for $Re = 400$. Powerlaw fits are shown as dashed lines with slopes 0.46 [left panel] and 0.18 [right panel, eq (2.13)].

centrifugal force along the lines in the magnetic finger, which in combination with the reconnection layer, presumably drives the residual radial outflow. Viscosity continues to be essential even as $\eta \to 0$ because it is then the only mechanism for communicating angular momentum between field lines, and between the fluid and the cylinders; the distortion of the field enhances viscous transport by bringing into closer proximity lines with different angular velocity.

To summarize, in the highly conducting limit $Re_m \to \infty$, Re =constant, there appear to be at least three main regions of the flow: (I) an "external" or "reflux" region in which the magnetic field is predominantly axial and the velocity predominantly toroidal, but with a small ($\propto \eta^{1/2}$) radial inflow; (II) a "jet" or "finger" of smaller but constant vertical width in which the fields are mainly horizontal and there is a more rapid but still $O(\eta^{1/2})$ flow along field lines; (III) a resistive layer or current sheet at the center of the jet whose width decreases as $\eta^{1/3}$, across which the horizontal fields change sign.

2.2.4 Simulations at small magnetic Prandtl number

In the ongoing Princeton MRI experiment, the experiment material, liquid gallium, has kinematic viscosity $\nu \approx 3 \times 10^{-3}$ cm^2 s^{-1} and resistivity $\eta \approx 2 \times 10^3$ cm^2 s^{-1}. The typical dimensionless parameters are $Re_m \approx 20$ and $Re \approx 10^7$ at the dimensions and rotation speeds cited above. The magnetic Prandtl number $Pr_{\rm m} \equiv Re_m/Re \approx 10^{-6}$ is very small. Reliable simulations with Reynolds number as high as 10^7 are beyond any present-day computer, and small $Pr_{\rm m}$ presents additional challenges for some codes.

Although our boundary conditions are not those of the experiment, we have carried out simulations at $Re_m = 20$ and much higher Re in order to explore the changes in the flow due to these parameters alone. A simulation for $Re = 25600$ is shown in Figures 2.12 & 2.13. All though this is still considerably more viscous than the experimental flow, it is clearly unsteady, like all of our simulations at $Re \gtrsim 3000$. A narrow jet can still be observed in the poloidal velocities, but the poloidal field is only weakly perturbed at this low Re_m: $B_{\varphi,\max} \approx 0.1 B_z$.

Since the Reynolds number of the experiment is much larger than that of our simulations, we can estimate the experimental torques only by extrapolation. Extrapolating according to eq. (2.11) from the highest-Re simulation in Table 2.2, one would estimate $\Delta\Gamma/\Gamma_{\rm initial} \sim 35$ at $Re \sim 10^7$. There are, however, reasons for caution in accepting this estimate. On the one hand, the experimental flow may be three-dimensional and turbulent, which might result in an even higher torque in the final state. On the other hand, the viscous torque in the initial state is likely to be higher than in these simulations because of residual Ekman circulation driven by the split endcaps. Nevertheless, we expect an easily measurable torque increase in the MRI-unstable regime.

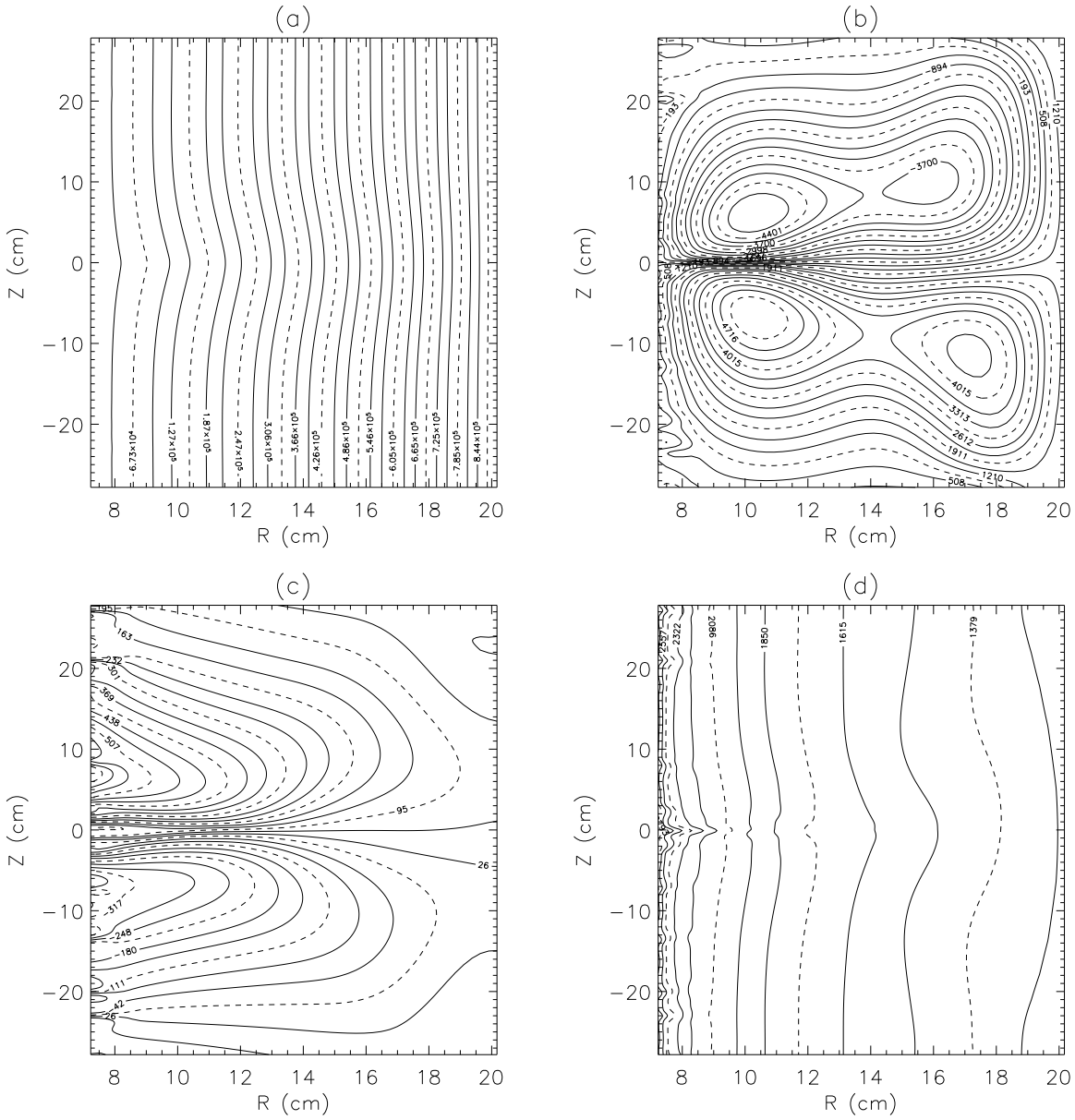

Figure 2.12: The same sequence as Fig. 2.4, but for $Re = 25600$, $Re_m = 20$. The flow is unsteady but closely resembles steady flows at lower Re for this Re_m.

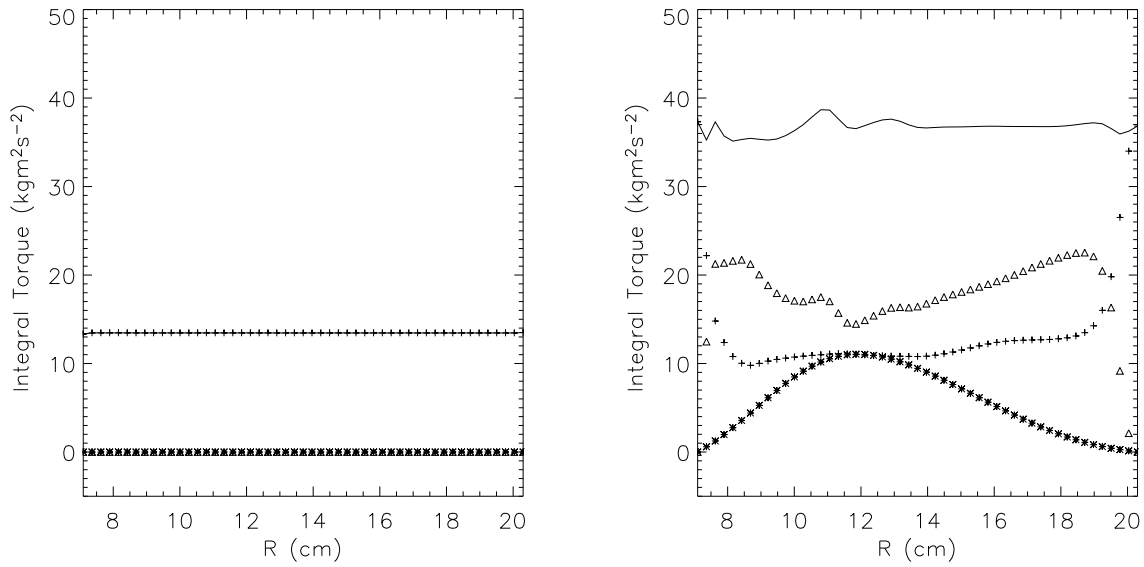

Figure 2.13: The z-averaged torques as in Fig. 2.8, but for the state shown in Fig. 2.12 ($Re = 25600$, $Re_m = 20$). The radial variation of the total torque, though slight, testifies to the unsteadiness of the flow. $+$, viscous torque; $*$, magnetic torque; $\triangle$, advective torque; solid line, total torque.

2.3 Conclusions

In this chapter, we have simulated the linear and nonlinear development of magnetorotational instability in a nonideal magnetohydrodynamic Taylor-Couette flow. The geometry matches with the experiment in preparation except in the vertical boundary conditions, which in these simulations are periodic in the vertical (axial) direction and perfectly conducting at the cylinders; these simplifications allow direct comparison with previous linear studies. We have also restricted our study to smaller fluid Reynolds number (Re), and extended it to larger magnetic Reynolds number (Re_m), than in the experiment. We find that the time-explicit compressible MHD code ZEUS-2D, which is widely used by astrophysicists for supersonic ideal flows with free boundaries, can be adapted and applied successfully to Couette systems. MRI grows from small amplitudes at rates in good agreement with linear analyses under the same boundary conditions. Concerning the nonlinear final state that results from

saturation of MRI, we draw the following conclusions:

1. Differential rotation is reduced except near boundaries, as predicted by Knobloch and Julien [74].

2. A steady poloidal circulation consisting of a narrow outflow (jet) and broad inflow is established. The width of the jet is almost independent of resistivity, but it does decrease with increasing Re. The radial speed of the jet $\propto Re_m^{-1/2}$.

3. There is a reconnection layer within the jet whose width appears to decrease $\propto Re_m^{-1/3}$.

4. The vertically integrated radial angular momentum flux depends upon viscosity but hardly upon resistivity, at least at higher Re_m [eq. (2.11)].

5. The final state is steady and laminar at $Re, Re_m \lesssim 10^3$ but unsteady at larger values of either parameter (Figs. 2.7 & 2.13.)

6. the final state contains horizontal fields comparable to the initial axial field for $Re_m \gtrsim 400$, and about a tenth as large for experimentally more realistic values, $Re_m \approx 20$.

We emphasize that these conclusions are based on axisymmetric simulations restricted to the range $10^2 \lesssim Re, Re_m \lesssim 10^{4.4}$, and that the boundary conditions are not realistic. This chapter is intended as a preliminary exploration of MRI in the idealized Taylor-Couette geometry that has dominated previous linear analyses. We have modeled many of the complexities of a realistic flow in the next chapters which show that these may significantly modify the flow.

Chapter 3

Princeton MRI Experiment[1]

3.1 Experimental Apparatus

As introduced in §1.5, for the gallium experiment, the inner and outer cylinders are made of stainless steel and the end plates are composed of two independently rotating rings. The computational domain is shown in: Fig. 3.1 and the parameters are summarized in Table 3.1. Six coils (black rectangles) with dimensions as shown were used, with 67 turns in the two coils nearest the midplane and 72 in the rest. They are split into two sets of three in parallel, with the upper three in serial and the bottom three also in serial. Currents I_φ were adjusted according to the experimental values. The implementation of full and partially conducting boundary condition is introduced in Appendix A.2.3. Note that in the simulations the magnetic diffusivity η is fixed to the experimental value $\eta = 2,430\ \mathrm{cm}^2\ \mathrm{s}^{-1}$ (Table.3.1), however the kinetic viscosity is changeable for the purpose of extrapolation.

The measured current waveform is displayed in Fig. 3.2 for the cases of 1000 A and 400 A. The waveform displayed has an overshoot at the early stage, a linear decline and then a linear ramp where the controller tries to adjust the output voltage to reach the programmed set point. This behavior is peculiar of the high current runs

[1] inherited and modified from Liu et al. [75]

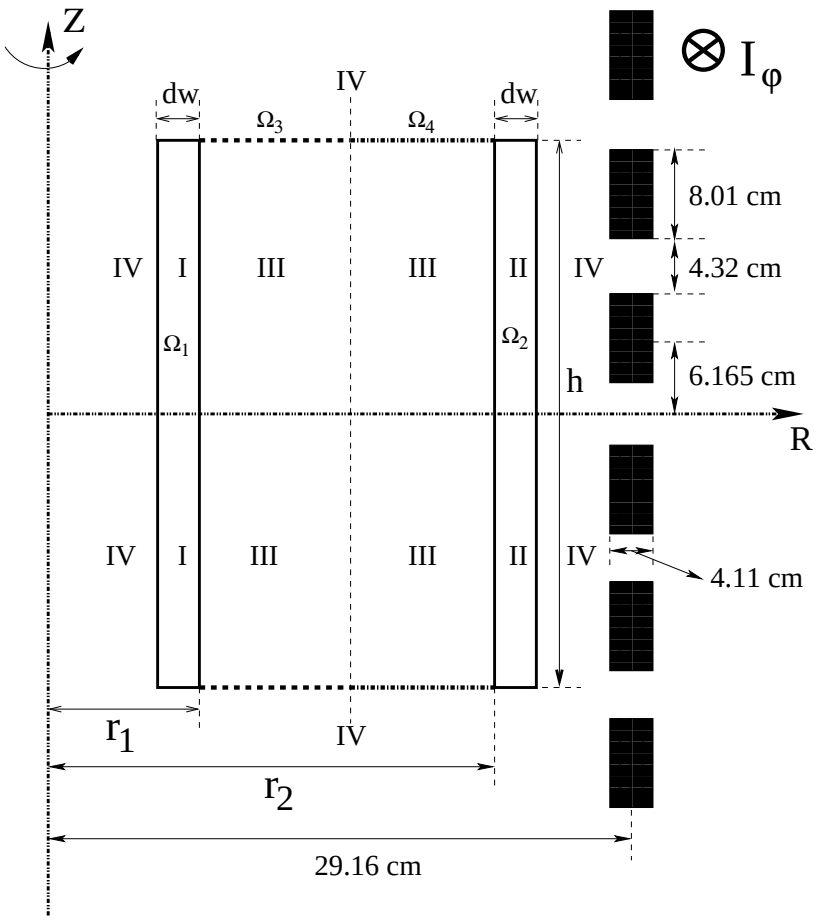

Figure 3.1: Computational domain for simulations of Princeton MRI experiment. Region (I): Inner copper cylinder, angular velocity Ω_1, magnetic resistivity η_I. (II): outer copper cylinder, Ω_2, η_{II}. (III): liquid gallium, $\eta_{\rm Ga}$; (IV): vacuum. Thick dash line: insulating inner ring, Ω_3. Thick dash-dot line: insulating outer ring, Ω_4. Thin dash line: middle plane. Dimensions: $r_1 = 7.1\,$cm; $r_2 = 20.3\,$cm; $h = 27.9\,$cm; $d_w = 0.9525\,$cm; 100% run: $\Omega_1/2\pi = 4000\,$rpm; $\Omega_2/2\pi = 533\,$rpm; $\Omega_3/2\pi = 1820\,$rpm; $\Omega_4/2\pi = 650\,$rpm.

Dimensions	
$r_1 = 7.1$ cm	$r_2 = 20.3$ cm
$h = 27.9$ cm	$d_w = 0.9525$ cm
Material Property	
$\rho_{\mathrm{Ga}} = 6.35$ gcm^{-3}	$\eta_{\mathrm{Ga}} = 2.43 \times 10^3$ cm^{2}s^{-1}
Rotation Profile (100% run)	
$\Omega_1/2\pi = 4000$ rpm	$\Omega_2/2\pi = 533$ rpm
$\Omega_3/2\pi = 1820$ rpm	$\Omega_4/2\pi = 650$ rpm
Rotation Profile (60% run)	
$\Omega_1/2\pi = 2400$ rpm	$\Omega_2/2\pi = 319.8$ rpm
$\Omega_3/2\pi = 1092$ rpm	$\Omega_4/2\pi = 390$ rpm
Adjusted Quiet Start (§3.3) (60% run)	
$\Omega_1/2\pi = 2400$ rpm	$\Omega_2/2\pi = 319.8$ rpm
$\Omega_3/2\pi = 1001$ rpm	$\Omega_4/2\pi = 390$ rpm

Table 3.1: Parameters used in the simulations

(left panel of Fig. 3.2). Lower currents have a much flatter waveform (right panel of Fig. 3.2).

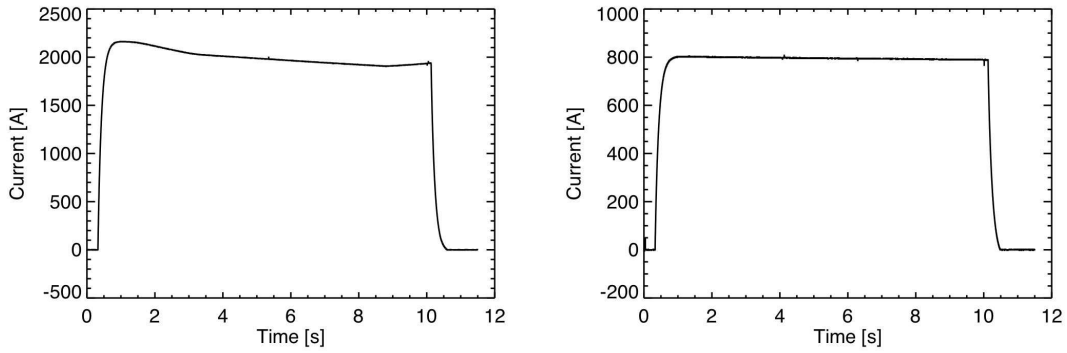

Figure 3.2: Figure Courtesy of Mark Nornburg. Experimental wave form of the coil current. Left panel: $I_\varphi = 1000$ A; right: $I_\varphi = 400$ A.

In the simulation a wave form like in Fig. 3.3 is used to approximate the experimental coil currents with ramp time $t_{coil} = 0.2$ s.

The outline of this Chapter is as follows. Section 3.2 presents the simulation results with fully insulating boundary condition. Two simplifications are employed in this section: (1) The conductivity of the stainless walls is ignored, that is: $\eta_I = \eta_{II} = \infty$ (Fig. 3.1). (2) All simulations in this section start from an arbitrary ideal

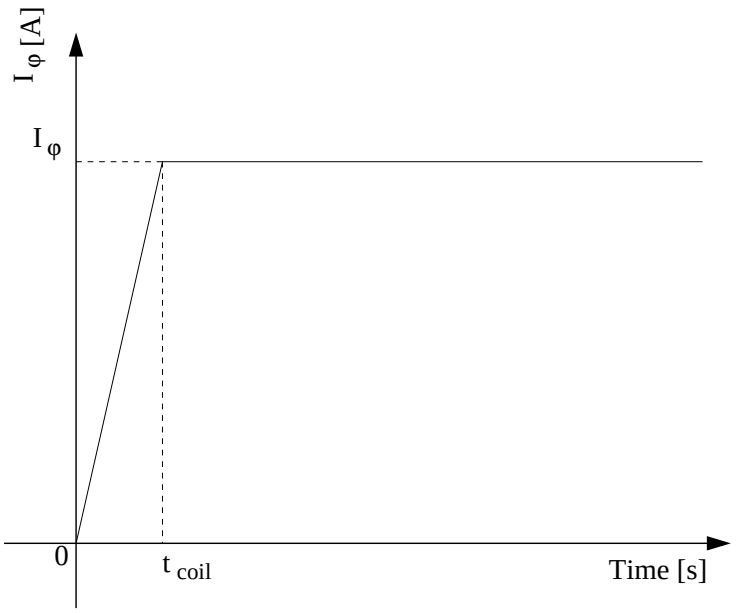

Figure 3.3: Simulated Current pattern in the external coils; the ramp time $t_{coil} = 0.2$ s; in most cases except stated explicitly, $I_\varphi = 1000$ A.

Couette state rather than an actual hydrodynamical equilibrium state with split end caps. Most of results presented in this section are the results of 100% run (100% of the designed values of our experiment, see Table.3.1) except stated explicitly. We idealize the problem further in Subsection 3.2.1 by assuming ideal Couette state at the end caps to remove the boundary effects (equivalent to divide the end caps into many rings). Subsection 3.2.2 mimics the Princeton MRI experiment more closely by splitting the end caps into only two rings as in the experiment (residual magnetic Ekman layer is present).

Section 3.3 models the problem even closer to the Princeton MRI experiment by addressing the problem with both complications ignored in Section 3.2. Furthermore in order to recover the linear phase, the rotation profile at the end caps is adjusted slightly to have a small $\widetilde{v}_r$ near the outer cylinder. Most of results in this section are the results of 60% run except stated explicitly since the experiment currently can only achieve 60% run restricted by the leakage resulted from the fast rotation. In

both sections the rotation profile at the end caps is different from the one used in the experiment.

3.2 Simulation with Fully Insulating Boundary Condition

As a first attack, we ignore the conductivity of the stainless steel walls, but regard them as insulating materials, that is: $\eta_I = \eta_{II} = \infty$. And please note that in this whole section, the simulations all start from an ideal Couette state rather than an actual hydrodynamical equilibrium state with split end caps.

As discussed in §1.4.1, The experiment is complicated by the extremely enormous Reynolds number and by Ekman circulation and Stewartson layers [50], even though the experimental apparatus has been designed to minimize the circulation by the use of independently controlled split endcaps. It is known that Ekman circulation is significantly modified when the Elsasser number [79] exceeds unity:

$$\Lambda = B_\infty^2/(8\pi\rho_{\rm Ga}\eta_{\rm Ga}\Omega) \gtrsim 1$$

where B_∞ is the axial magnetic field far away from the end cap and $\Omega = \sqrt{\Omega_1\Omega_2}$ is the characteristic rotation frequency. For the 100% rotation as above and with $I_\varphi = 1000$ A, $\Lambda = 0.36$.

3.2.1 Without Magnetic Ekman Circulation

In order to simplify the problem, in this subsection we set the rotation profile on the end caps to $\Omega = a + b/r^2$, where $a = (\Omega_2 r_2^2 - \Omega_1 r_1^2)/(r_2^2 - r_1^2)$ and $b = r_1^2 r_2^2(\Omega_1 - \Omega_2)/(r_2^2 - r_1^2)$. In other words the rotation profile on the end caps is ideal Couette state to remove the boundary effects. Also this set-up provides an opportunity to

Re_m	Re	n	Prediction [s^{-1}]	Simulation [s^{-1}]
20	6400	1	33.7(*)	33.1
20	6400	2	13.8	

Table 3.2: 100% run. Growth rates from semianalytic linear analysis *vs.* simulation.

benchmark with a "global" linear code [73], which is periodic in vertical direction thus also does not have the end caps effects.

In the linear regime, MRI has been extensively studied both locally and globally [52, 53, 69, 83–85]. We have used these linear results to benchmark our code used in Chap. 2. Linear modes are proportional to $\exp(\gamma t - ik_z z) f(k_r r)$, where γ is the growth rate, and $f(x)$ is an approximately sinusoidal radial function, at least outside boundary layers, whose zeros are spaced by $\Delta x \approx \pi$. The wavenumbers $k_z = 2n\pi/h$ and $k_r \approx m\pi/(r_2 - r_1)$, where n and m are positive integers. We will consider only the lowest value of k_r ($m = 1$) but allow $n \geq 1$. Please note here $k_z = 2n\pi/h$ rather than $n\pi/h$ used in [73] and the linear analyses mentioned above [52, 53, 69, 83–85]. This different definition of k_z sets $\delta v_r = 0$ and $\delta v_\varphi = 0$ at the end caps ($z = 0,\ h$) but $\delta v_z \neq 0$ due to the incompressibility. Therefore the "global" linear code does not have a radial flow at the end caps ($z = 0,\ h$) as the ZEUS simulation of this situation.

A comparison of the growth rates found by this analysis with those obtained from our simulations is given in Table 3.2. In Table 3.2, the largest growth rate predicted by the linear analysis has been marked with an asterisk (*). The simulations naturally tend to be dominated by the fastest numerical mode—that is, the fastest eigenmode of the finite-difference equations, which need not map smoothly into the continuum limit. Fortunately, as asserted by the Table, the fastest growth occurs at the same vertical harmonic n in the simulations as in the linear analysis. And they match nicely with 2 significant digits.

3.2.2 Split Rings

Next we create the boundary conditions closer to the real experiment by splitting the end caps into only two rings as in Fig. 3.1.

Linear phase

The first convincing evidence of the existence of MRI is its linear growth rate (Fig. 3.4). Interestingly the growth rate is reduced from 33.1 s^{-1} to 21.7 s^{-1}. This possibly is due to the residual magnetic Ekman circulation, which modifies the background flow. We note that the growth rate of the Helical MRI is even more dramatically reduced by having insulating end caps [45], which might be the combination of both Ekman circulation and the traveling wave-boundary interaction.

Structure of the final state

As noted in §2.1, instabilities cannot easily modify the differential rotation of accretion disks because internal and magnetic energies are small compared to gravitational ones, and MRI is believed to saturate by turbulent reconnection [88, 89]. In Couette flow, however, the energetics do not preclude large changes in the rotation profile. As shown by Fig. 3.5, the differential rotation of the final state is reduced somewhat compared to the initial state in the interior of the flow, and steepened near the inner cylinder.

For $Re = 6400$, the final state is not steady. Typical time averaged flow and field patterns are shown in Fig. 3.6. The poloidal flux and stream functions are defined so that

$$\boldsymbol{V}_P \equiv V_r \boldsymbol{e}_r + V_z \boldsymbol{e}_z = r^{-1} \boldsymbol{e}_\varphi \times \boldsymbol{\nabla} \Phi, \qquad \boldsymbol{B}_P \equiv B_r \boldsymbol{e}_r + B_z \boldsymbol{e}_z = r^{-1} \boldsymbol{e}_\varphi \times \boldsymbol{\nabla} \Psi, \quad (3.1)$$

which imply $\boldsymbol{\nabla} \cdot \boldsymbol{V}_P = 0$ and $\boldsymbol{\nabla} \cdot \boldsymbol{B}_P = 0$. [Our velocity field is slightly compressible,

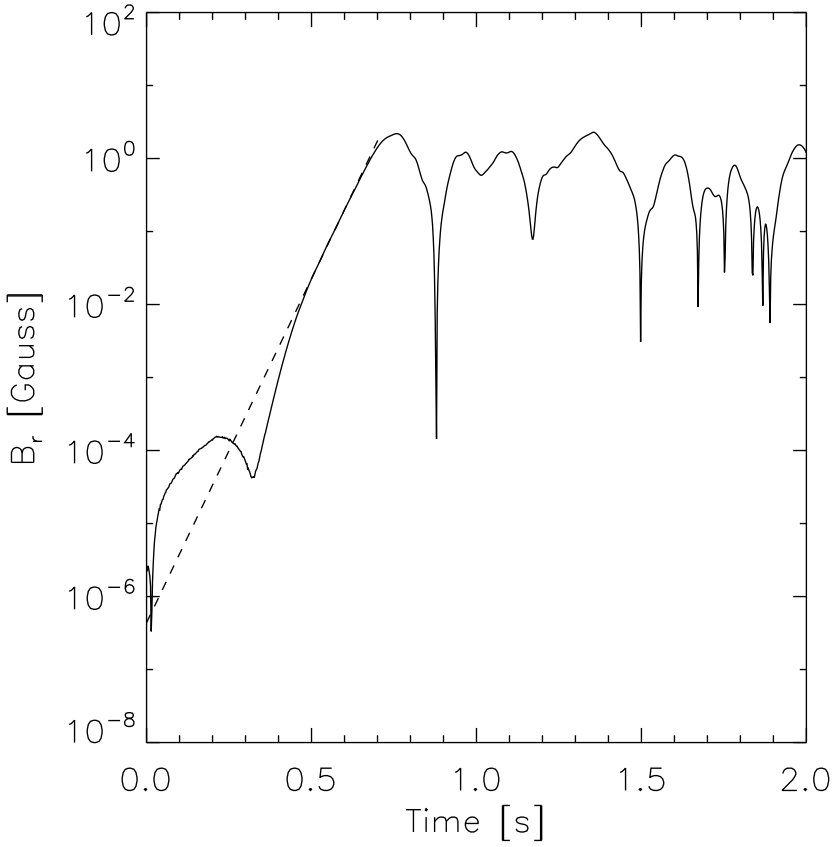

Figure 3.4: 100% run (MRI unstable) and $I_\varphi = 1000$ A. B_r *vs.* time for $Re = 6400$, $Re_m = 20$ sampled outside the fluid at $z = 13.95$ cm, $r = 25.0$ cm."Bottom end cap" is located at $z = 0$. Height $h = 27.9$ cm. Growth rate $\gamma = 21.7$ s^{-1}.

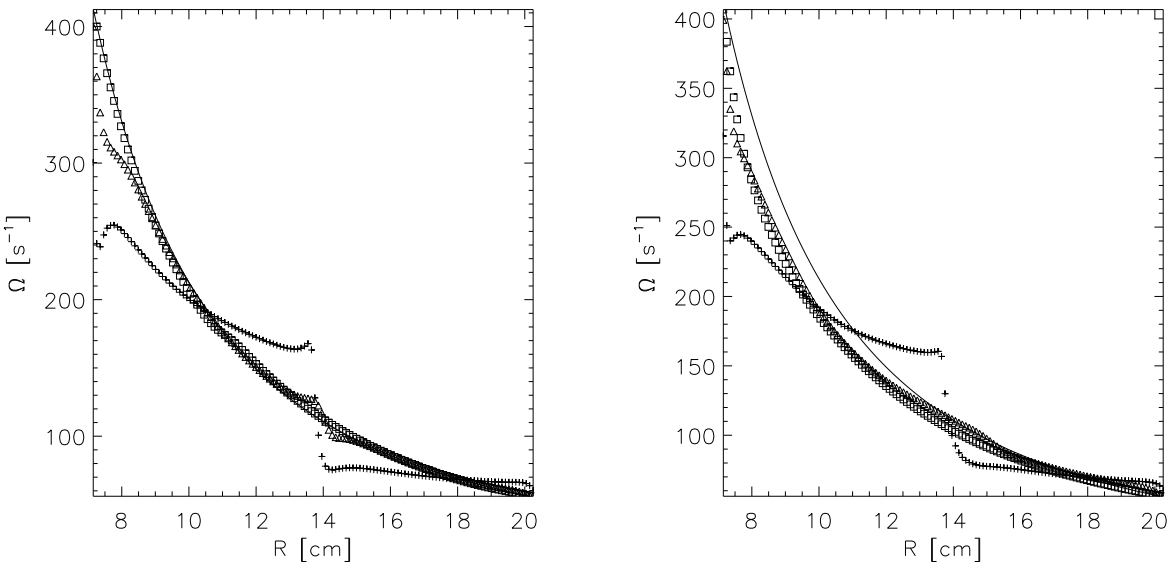

Figure 3.5: 100% run. Time averaged angular velocity profile before and after saturation at several heights (cm), for $Re = 6400$, $Re_m = 20$. left panel: pure hydro run; right: $I_\varphi = 1000$ A, $\Lambda = 0.36$. solid line, initial state (ideal Couette state); $+$, 0.11 cm; $\triangle$, 1.31 cm; $\square$, 13.95 cm. "Bottom end cap" is located at $z = 0$. Height $h = 27.9$ cm. for comparison, here a pure hydro run is also presented.

so that eq. (3.1) does not quite capture the full velocity field. Nevertheless, the error is small, and Φ is well defined by $\nabla^2(\Phi \boldsymbol{e}_\varphi/r) = \boldsymbol{\nabla} \times \boldsymbol{V}_{\rm P}$ with $\partial\Phi/\partial r = 0$ on the end caps and $\partial\Phi/\partial z = 0$ on the cylinders.]

We note that the induced toroidal field is around 6% at this magnetic Reynolds number Re_m: $B_{\varphi,\max} \approx 0.06 B_z$. The most striking feature is the inflowing "jet" centered near $z = 13.95$ cm in Figure 3.6 (see also Fig. 3.7), which is opposite to the usual Ekman circulation [47]. It seems that the rapid outflowing "jet" found in [73] with vertically periodic boundary condition, where the position of the "jet" is arbitrary, is shifted to the boundary layer, near the end caps in the experiment.

This opposite oriented "jet" especially near the inner cylinder part is a direct consequence of MRI. The use of independently controlled split endcaps without the magnetic field would split the big two Ekman cells [47] into eight small cells, four at the upper half and four at the bottom half (Fig. 3.8) (with a high Reynolds number,

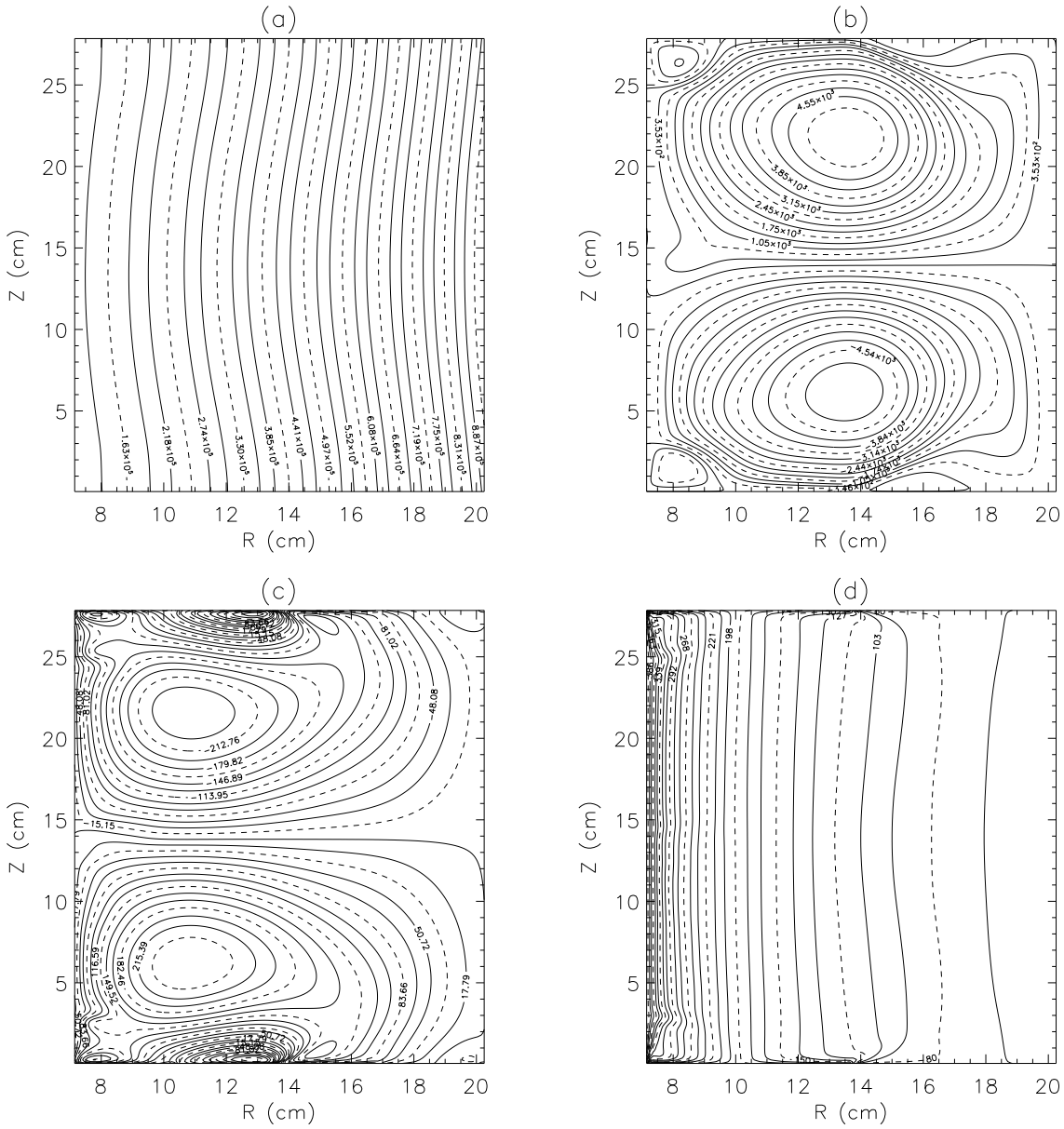

Figure 3.6: 100% run. Contour plots of final-state velocities and fields (MRI unstable). $Re = 6400$, $Re_m = 20$. $I_\varphi = 1000$ A, $\Lambda = 0.36$. (a) Poloidal flux function $\Psi\,(\mathrm{Gauss\,cm^2})$ (b) Poloidal stream function $\Phi\,(\mathrm{cm^2 s^{-1}})$ (c) toroidal field $B_\varphi\,(\mathrm{Gauss})$ (d) angular velocity $\Omega \equiv r^{-1}V_\varphi\,(\mathrm{rad\,s^{-1}})$.

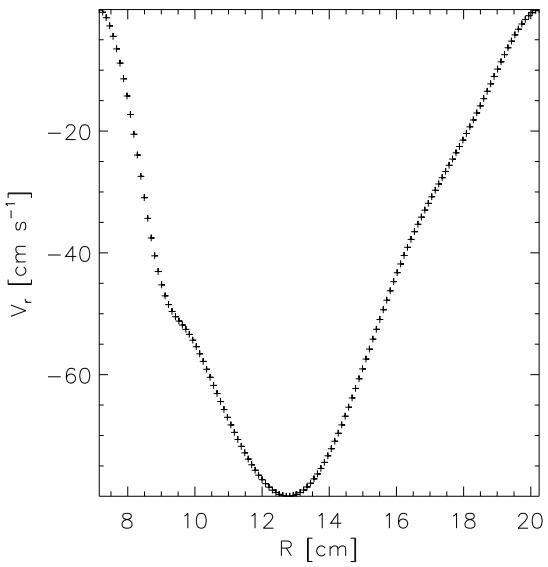

Figure 3.7: Corresponding to Fig. 3.6(b). 100% run (MRI unstable). Time averaged v_r *vs.* radius r on the middle plane ($z = h/2$). $Re = 6400$, $Re_m = 20$. $I_\varphi = 1000$ A, $\Lambda = 0.36$.

the system is not steady). Hereafter we focus only on the upper half. The circulation direction of the bottom four cells is opposite to the circulation direction of the corresponding upper cells. This can be understood from Fig. 3.10. The ideal Couette state causes a constant radial angular momentum flux along the radii. However the no-slip boundary condition at the end plate, though split into two rings, would still cause a development of the residual Ekman layer, where the velocity of the flow differs from a pure toroidal rotation. In the bulk of the fluid the radial equilibrium pressure p_0 is determined from the equation of radial force balance. However, at the end plate the velocity of the liquid is not ideal Couette state. Where $r \lesssim 10.6$ cm, as the usual Ekman circulation, the radial gradient of p_0 undergoes not counterbalanced by the sum of the centrifugal and Coriolis forces due to the rotation of the fluid with a smaller rotation speed Ω_3 than the corresponding ideal Couette rotation speed. This extra pressure gradient forces the radial flow near the end plate. This flow is oriented inward, i.e., from the region of higher uncompensated pressure to the region

of lower pressure. This usual anti-clock-wise Ekman circulation arises in this region (see Fig. 3.9). However where 10.6 cm $\lesssim r \lesssim$ 13.7 cm, the radial gradient of p_0 could not balance the sum of centrifugal and Coriolis forces due to a larger rotation speed Ω_3 than the corresponding ideal Couette one. This leads to an anomalous clock-wise Ekman circulation in this region, leading to the inflowing "jet" (see Fig. 3.9). The same situation happens where 13.7 cm $\lesssim r \lesssim$ 18.2 cm (anti-clock-wise) and where $r \gtrsim$ 18.2 cm (clock-wise) (Fig. 3.9). We do not observe an inflowing "jet" near the inner cylinder ($r \lesssim$ 10.6 cm) (Fig. 3.9).

The addition of the external magnetic field (set up still in the MRI stable regime by reducing the rotation speed, however keeping the same Elsasser number Λ) aligns the flow along the magnetic field lines, elongate the cells vertically, which make the cells penetrate deeper into the fluid, and lead to a more steady final state (Fig. 3.11). Again at this time we would not observe an inflowing "jet" near the inner cylinder ($r \lesssim$ 10.6 cm) (Fig. 3.12). However in the MRI unstable regime with the same Λ the scale of the middle clock-wise cell would be increased not only vertically but also horizontally and eventually dominate the other three which retreat to the corners if the instability is strong enough. This leads to one inflowing "jet" near the inner cylinder (Fig. 3.7).

We note that in the MRI stable case the induced toroidal field is much weaker ($B_{\varphi,\max} \approx 0.0036 B_z$ compared to $B_{\varphi,\max} \approx 0.06 B_z$ in the MRI unstable case). The poloidal field also changes more slightly in the MRI stable case. This implication is that the Lorentz force is much more significant in the MRI unstable case than the MRI stable case. The Lorentz force is given by:

$$(\vec{B} \cdot \nabla)\vec{B} = B_r \frac{\partial}{\partial r} B_r + B_z \frac{\partial}{\partial z} B_r - \underline{\frac{B_\varphi^2}{r}},$$

in which the underlined term is much more dominant in the MRI unstable case,

enhancing the clock-wise cells and drives the fluid flowing inward near the inner cylinder.

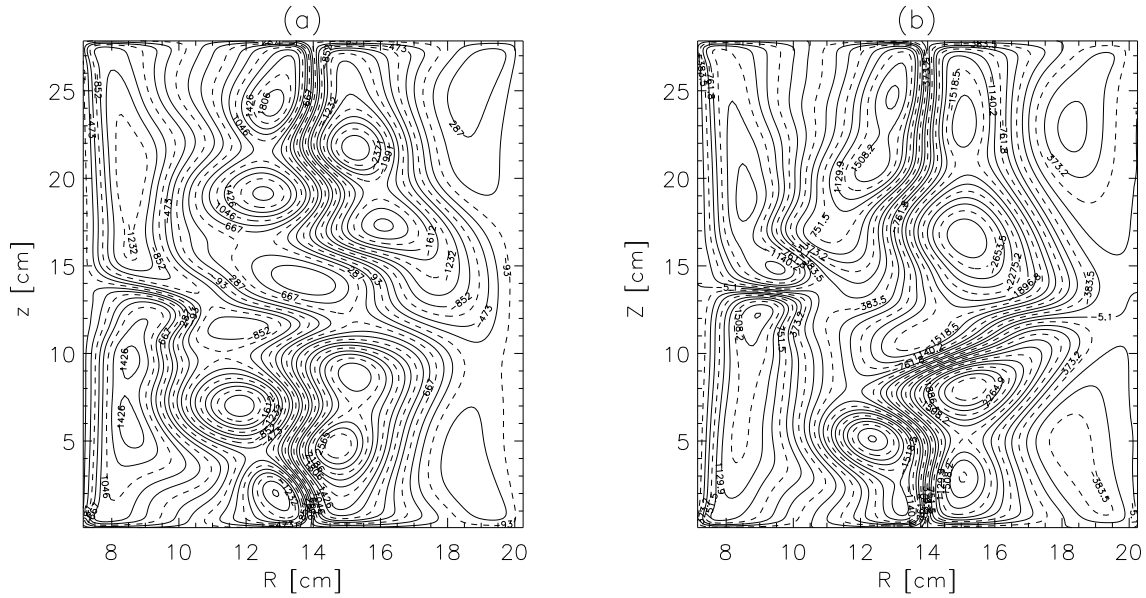

Figure 3.8: 100% rotation run. Compare with Fig. 3.6 (b). Contour plots of poloidal stream function $\Phi\,(\mathrm{cm}^2\mathrm{s}^{-1})$ for $Re = 6400$ without magnetic field at different time t [s]. (a) $t = 4.5$ s, (b) $t = 4.75$ s.

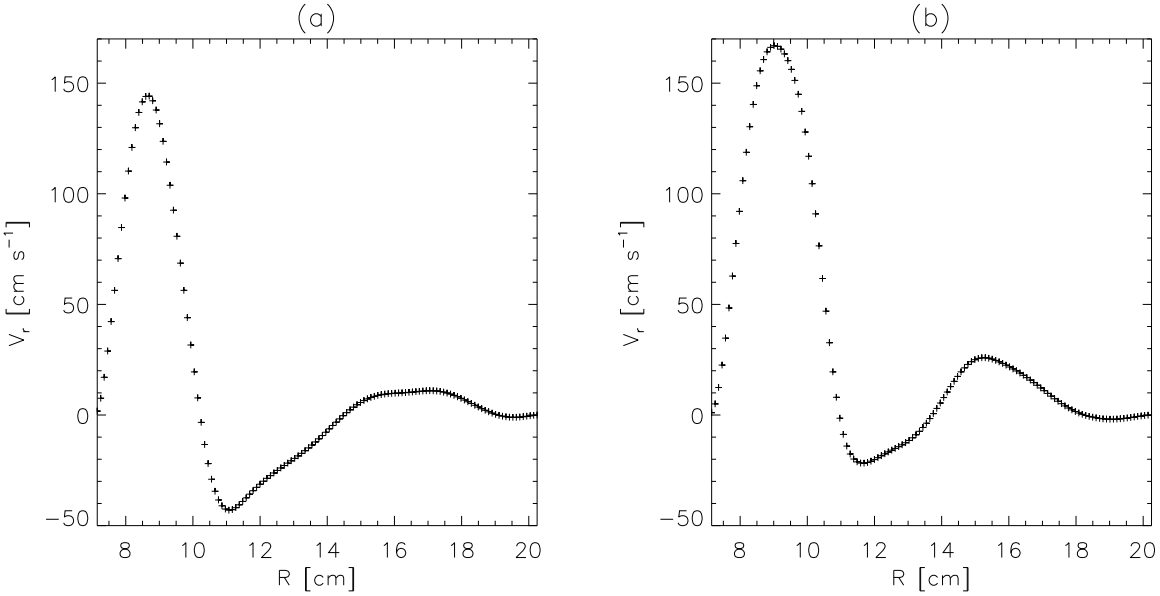

Figure 3.9: Corresponding to Fig. 3.8. 100% rotation run. Time averaged v_r *vs.* radius r on the middle plane ($z = h/2$). $Re = 6400$, $Re_m = 20$. $I_\varphi = 0$ A, $\Lambda = 0$.

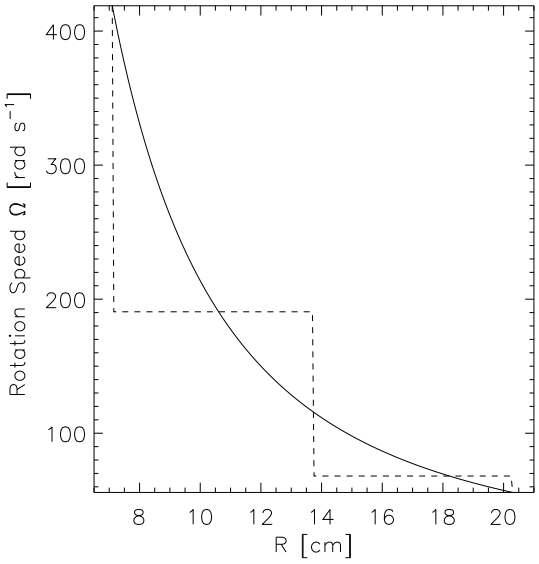

Figure 3.10: 100% run. Two independent rotating rings generates 8 cells. solid line, ideal Couette state; dashed line, rotation profile at the end caps.

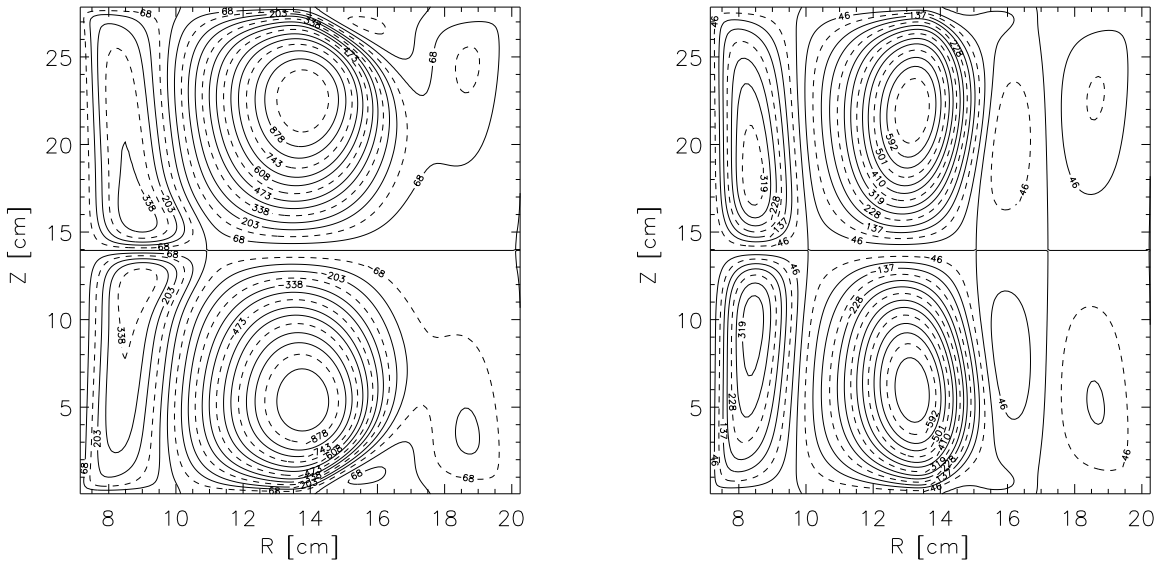

Figure 3.11: 25% rotation run (MRI stable). Contour plots of final-state poloidal stream function $\Phi\,(\mathrm{cm}^2\mathrm{s}^{-1})$ for $Re = 6400$, $Rm = 4$. Left panel: $I_\varphi = 500$ A, $\Lambda = 0.36$; right: $I_\varphi = 1000$ A, $\Lambda = 1.43$. Note the aligning effect of the external magnetic field for higher Λ.

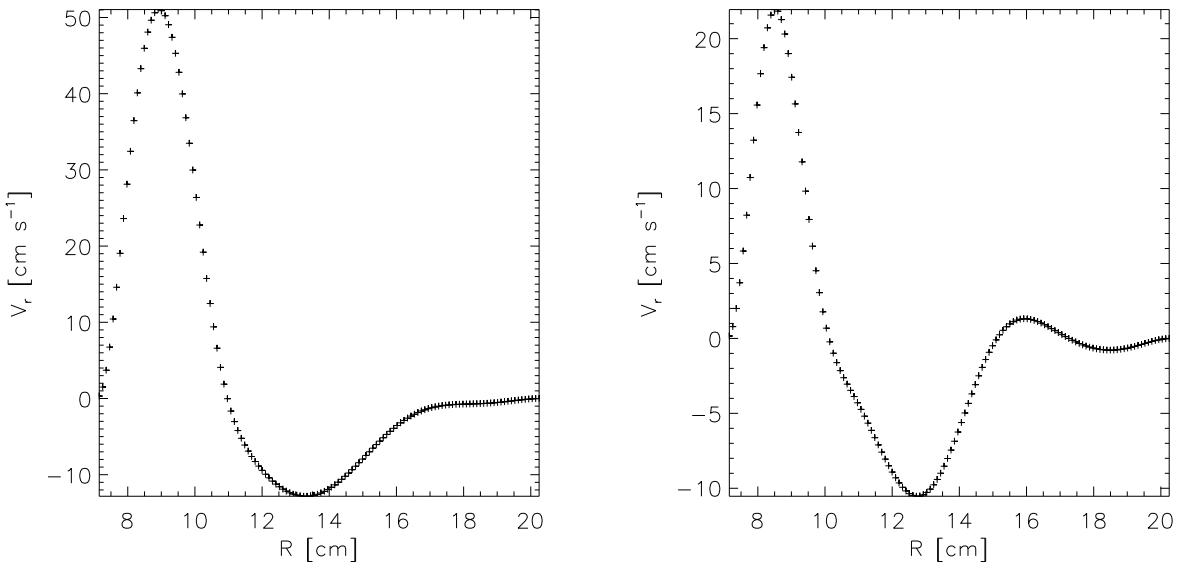

Figure 3.12: Corresponding to Fig. 3.11. 25% rotation run (MRI stable). Time averaged v_r *vs.* radius r on the middle plane ($z = h/2$) for $Re = 6400$, $Rm = 4$. Left panel: $I_\varphi = 500$ A, $\Lambda = 0.36$; right: $I_\varphi = 1000$ A, $\Lambda = 1.43$.

Another assuring evidence, that it is MRI which causes an "inflowing" jet, exists in the simulations (§3.2) with the ideal Couette state at the end caps, which does not have end plate effects thus does not have magnetic Ekman circulation at all (Fig. 3.13). From Fig. 3.13, the direction (clock-wise) of circulation is opposite to the usual Ekman circulation (anti-clock-wise) [47]. There is a clear "inflowing" jet near the inner cylinder in this case (see Fig. 3.14). This suggests that the poloidal circulation seen in the final state in the split-endcap cases (Fig. 3.6 (b)) is caused mainly by saturation of MRI rather than the magnetic Ekman circulation.

Angular momentum transport

Astrophysicists are interested in the angular momentum transport due to MRI since MRI is supposed to be the most probable mechanism to explain the fast accretion in the astrophysical disks. Fig. 3.15 displays the r-profiles of the radial advective, viscous, and magnetic angular momentum fluxes integrated over cylinders coaxial

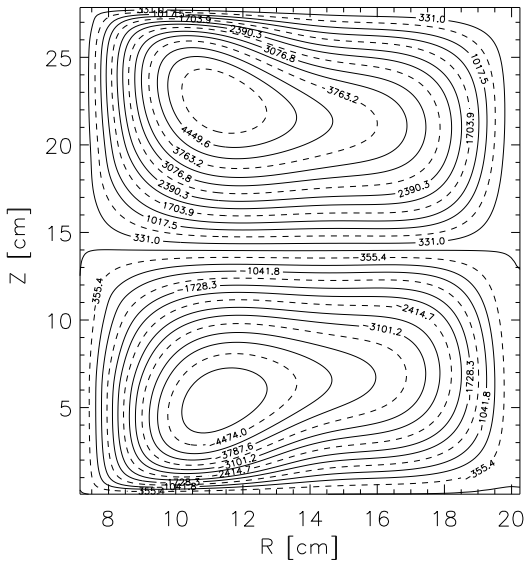

Figure 3.13: 100% rotation run (MRI unstable). Contour plots of poloidal stream function $\Phi\,(\mathrm{cm}^2\mathrm{s}^{-1})$ for $Re = 6400$ with ideal Couette state at the end caps. $I_\varphi = 1000$ A, $\Lambda = 0.36$.

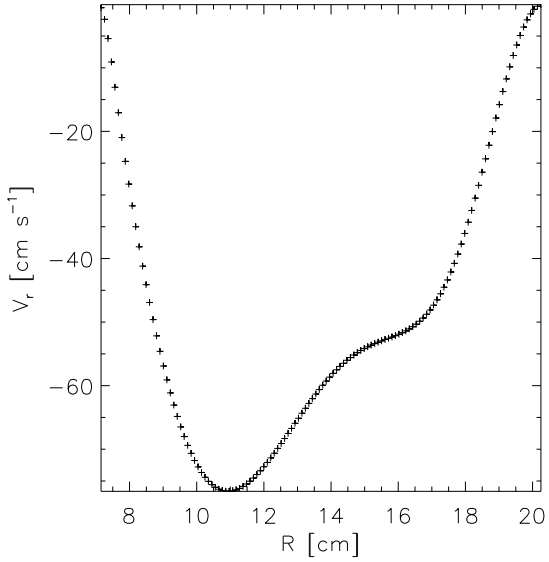

Figure 3.14: Corresponding to Fig. 3.13. 100% rotation run (MRI unstable). Time averaged v_r *vs.* radius r on the middle plane ($z = h/2$) for $Re = 6400$ with ideal Couette state at the end caps. $I_\varphi = 1000$ A, $\Lambda = 0.36$.

with the boundaries (thus they are radial advective, viscous, and magnetic torques respectively):

$$\Gamma_{\mathrm{advective,r}}(r) = \int_0^h dz\, \rho r^2 v_r v_\varphi \,, \tag{3.2}$$

$$\Gamma_{\mathrm{magnetic,r}}(r) = \int_0^h dz \left(-\frac{r^2 B_r B_\varphi}{4\pi} \right) , \tag{3.3}$$

$$\Gamma_{\mathrm{viscous,r}}(r) = \int_0^h dz \left[-r^3 \rho \nu \frac{\partial}{\partial r} \left(\frac{v_\varphi}{r} \right) \right] \tag{3.4}$$

$$\Gamma_{\mathrm{total,r}}(r) = \Gamma_{\mathrm{advective,r}}(r) + \Gamma_{\mathrm{magnetic,r}}(r) + \Gamma_{\mathrm{viscous,r}}(r) \,. \tag{3.5}$$

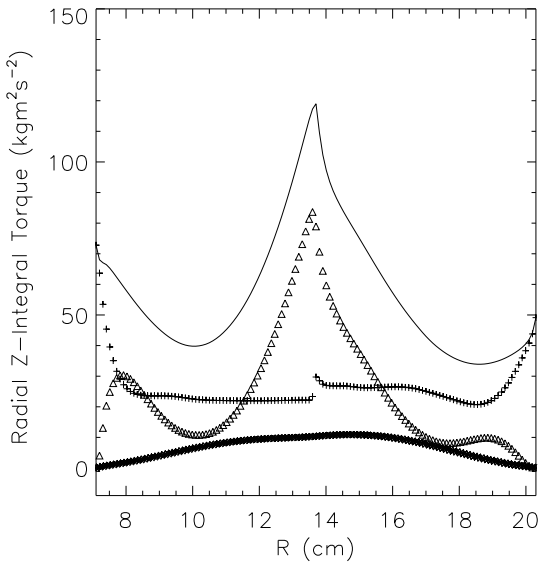

Figure 3.15: 100% run (MRI unstable). z-integrated radial angular momentum fluxes versus r at saturation. $Re = 6400$, $Re_m = 20$. $I_\varphi = 1000$ A, $\Lambda = 0.36$. $+$, viscous torque; $*$, magnetic torque; $\triangle$, advective torque; solid line, total torque.

In contrast to the final state for vertically periodic boundary conditions [73], the total radial torque is not constant with radius. Since our numerical scheme conserves angular momentum exactly, we can infer a vertical flux arising from exchange of angular momentum with the endcaps. From the gradients of the radial torque, we identify four Ekman circulation cells: where $d\Gamma_{\mathrm{total,r}}/dr > 0$ (< 0) , the fluid is losing

(gaining) angular momentum at the endcaps and the boundary-layer flow is therefore radially inward (outward). This is consistent with the discussion of the poloidal circulation pattern of the flow with two split rings in §3.2.2.The radial magnetic and advective torques vanish at r_1 and r_2 because of the boundary conditions but are important at intermediate radii especially the latter, which means the middle clockwise cell is enhanced and transport more angular momentum. All components of the radial torques are positive, which means that the angular momentum is transported radially outwards.

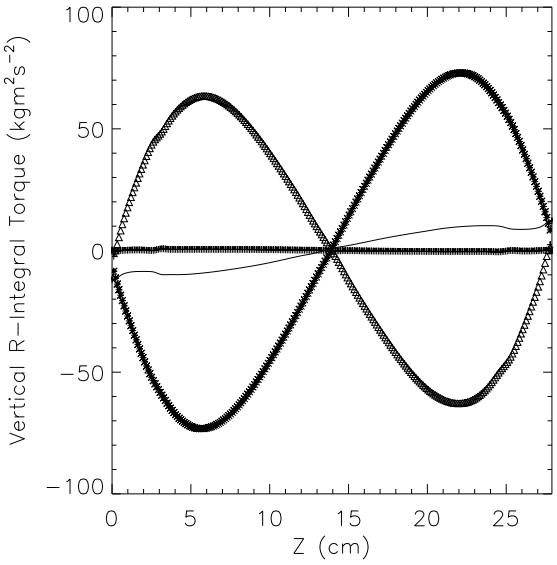

Figure 3.16: 100% run (MRI unstable). r-integrated vertical angular momentum fluxes versus z at saturation. $Re = 6400$, $Re_m = 20$. $I_\varphi = 1000$ A, $\Lambda = 0.36$. $+$, viscous torque; $*$, magnetic torque; $\triangle$, advective torque; solid line, total torque.

Fig. 3.16 displays the z-profiles of the vertical advective, viscous, and magnetic angular momentum fluxes integrated over radius (thus they are vertical advective,

viscous, and magnetic torques respecitvely):

$$\Gamma_{\mathrm{advective,z}}(z) = \int_{r_1}^{r_2} dr\, \rho r^2 v_z v_\varphi \,, \tag{3.6}$$

$$\Gamma_{\mathrm{magnetic,z}}(z) = \int_{r_1}^{r_2} dr \left(-\frac{r^2 B_z B_\varphi}{4\pi}\right) , \tag{3.7}$$

$$\Gamma_{\mathrm{viscous,z}}(z) = \int_{r_1}^{r-2} dr \left[-r^2 \rho \nu \frac{\partial}{\partial z}\left(v_\varphi\right)\right] \tag{3.8}$$

$$\Gamma_{\mathrm{total,z}}(z) = \Gamma_{\mathrm{advective,z}}(z) + \Gamma_{\mathrm{magnetic,z}}(z) + \Gamma_{\mathrm{viscous,z}}(z)\,. \tag{3.9}$$

From these two figures, we can see that the global angular momentum is entering from the inner cylinder then most of it is flowing out from the outer cylinder while the rest of it is flowing out at the two end caps.

Angular momentum is transported outward.

It is very interesting to derive the relationship of the total radial torque at the inner cylinder, which is supposed to be the source of the angular momentum, with Reynolds number Re and of the sum of total vertical torques at both endcaps with Reynolds number Re.

From Figure 3.17 (a), we infer the following scalings (100% run, $Re_m = 16$):

(1) $I_\varphi = 0$ A or $\Lambda = 0$, which can be regarded as the initial state of the experiment since the experiment would start from a purely hydrodynamical equilibrium state (100% run, $100 \lesssim Re \lesssim 25600$).

$$\Gamma_{\mathrm{initial},r}(r_1) \approx 2.69 \times 10^4 Re^{-0.691}\,; \tag{3.10}$$

(2) $I_\varphi = 1000$ A or $\Lambda = 0.36$, which can be regarded as the final state of the experiment (100% run, $100 \lesssim Re \lesssim 25600$).

$$\Gamma_{\mathrm{final},r}(r_1) \approx 1.98 \times 10^4 Re^{-0.639}\,. \tag{3.11}$$

From these two scaling laws, *the MRI indeed enhances the angular momentum transport at saturation*, though not conclusively (see discussion below).

If Eq. 3.10 and Eq. 3.11 also work at larger Reynolds number regime, that is, the total radial torque of the initial and final state at the inner cylinder can be calculated by extrapolation of Eq. 3.10 and Eq. 3.11 respectively to the experimental Reynolds number ($Re \approx 1.15 \times 10^7$, 100% run), then the total radial torque of the initial and final state at the inner cylinder may be as large as (100% run)

$$\Gamma_{\text{initial},r}(r_1) \approx 0.359 \text{ Newton m}$$

and

$$\Gamma_{\text{final},r}(r_1) \approx 0.611 \text{ Newton m}$$

respectively. Thus, the ratio of the increase of the torque over the initial torque is: $(0.611 - 0.356)/0.356 = 72\%$, which is quite measurable and indicates that at the experimental Reynolds number MRI would dominate the residual magnetic Ekman circulation in the point of view of transporting the angular momentum. There are, however, reasons for caution in accepting this estimate. For example, the experimental flow may be three-dimensional and turbulent, which might result in an even higher torque in the final state, and both the exponents seem to decrease at larger Reynolds number and the difference of these two exponents is small. These concerns all make the extrapolation of Eq. 3.10 and Eq. 3.11 to the experimental Reynolds number a bit risky. Nevertheless, we expect a noticeable torque enhancement in the MRI-unstable regime.

From Figure 3.17 (b), we can see that: (1) At larger Reynolds number, more angular momentum is transported vertically. This is reasonable since the Ekman circulation is more dominant when Reynolds number is larger; (2) In the MRI stable regime ($Re \lesssim 1600$), the magnetic field enhances the vertical transport of the angular

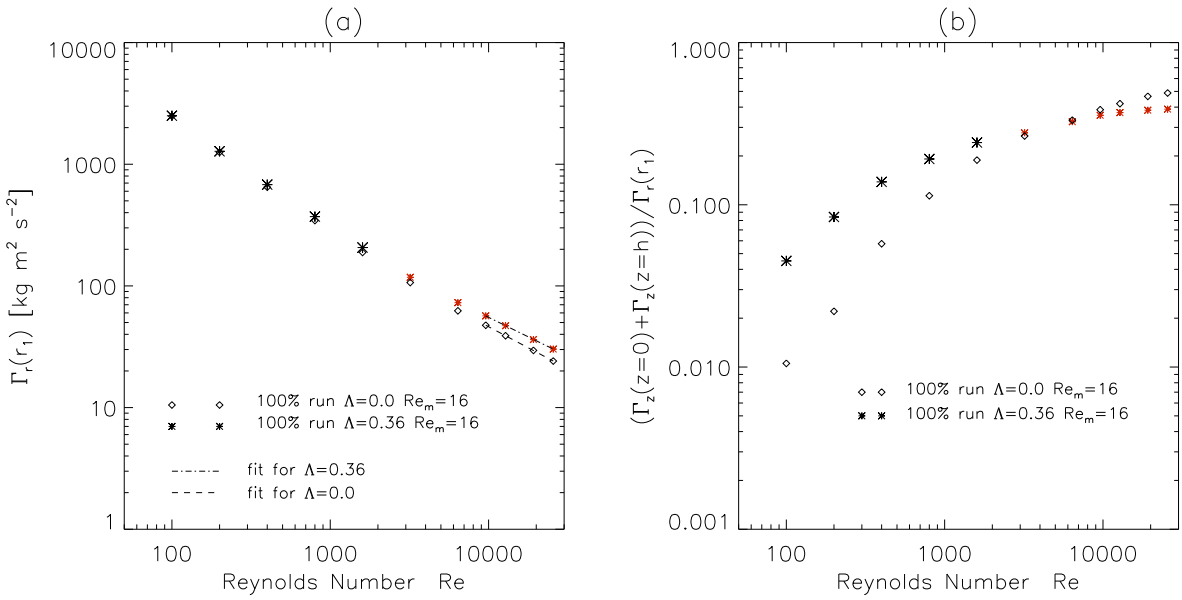

Figure 3.17: (a) Total radial torque at the inner cylinder (b) Sum of the total vertical torques at both endcaps *versus* *Re*. Note that in the simulations the magnetic diffusivity η is fixed to the experimental value $\eta = 2,430\ \text{cm}^2\ \text{s}^{-1}$ (Table.3.1), however the kinetic viscosity is changeable for the purpose of extrapolation. In both panel, red colors: MRI unstable; black color: MRI stable. In panel (a), dashed lines have slopes of -0.691 (initial state) and dash-dot lines -0.639 (final state).

momentum. This is also reasonable since the magnetic field would align the flow, thus having the cells elongating and penetrating deeper into the bulk. The middle cells are increased vertically by the residual magnetic Ekman circulation. (3) In the MRI unstable regime ($Re \gtrsim 3200$), the onset of the MRI results in more angular momentum transported radially outwards thus fewer angular momentum is transported vertically. The MRI would increase the scale of the middle cell horizontally. Therefore it transports more angular momentum radially outwards.

Strong Magnetic Field Suppresses MRI with two split rings

MRI essentially is a weak field instability. It is characteristic of MRI for a strong magnetic field to suppress this instability. Our experimental facility can only allow $I_\varphi \lesssim 1200$ A. Thus we need to try carefully to find one set of proper parameters

under which one growing mode is present with low I_φ while absent with larger I_φ. Fortunately simulations with 45% run demonstrate this property (Fig. 3.18).

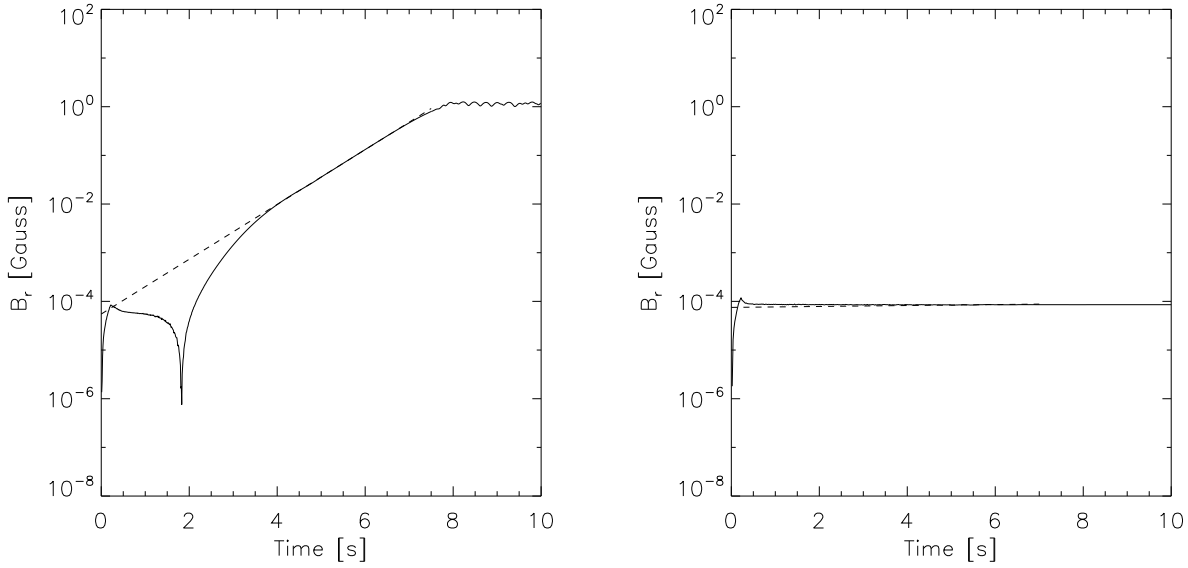

Figure 3.18: 45% run. B_r *vs.* time for $Re = 6400$, $Re_m = 7.3$ sampled outside at $z = 13.95$ cm, $r = 25.0$ cm."Bottom end cap" is located at $z = 0$. Height $h = 27.9$ cm. left panel: $I_\varphi = 750$ A, growth rate $\gamma = 1.3$ s^{-1}; right panel: $I_\varphi = 1200$ A, stable.

3.2.3 Summary of split rings studies

In conclusion of this section we have simulated the nonlinear development of magnetorotational instability in a nonideal magnetohydrodynamic Taylor-Couette flow. The simulations mimic an on-going experiment except that the conductivity of the stainless steel walls is neglected and the simulation is started from an ideal Couette state rather than an actual hydrodynamical equilibrium state with split end caps. We have also restricted our study to smaller fluid Reynolds number (Re) than in the experiment, however we have used exactly the same magnetic Reynolds number (Re_m). MRI grows from small amplitudes at rates in good agreement with linear analyses without the end cap effects.

Concerning the MRI simulations with two split independently rotating rings like the real experimental facility, we draw the following conclusions:

1. A clear linear phase is observed,

2. Differential rotation is reduced somewhat in the final state,

3. In the final state one inflowing "jet" opposite to the usual Ekman circulation "jet" [47] is found near the inner cylinder, a direct consequence of MRI rather than the residual Magnetic Ekman circulation (100% run),

4. The MRI enhances the angular momentum transport at saturation, though not conclusively. (100% run),

5. The final state contains horizontal fields about 6% as large as the initial poloidal field for $Re_m \approx 20$ (100% run),

6. Magnetized ($\Lambda > 0$) cases are steadier than pure hydrodynamic cases at the same Re.

3.3 Simulation with Partially Conducting Insulating Boundary Condition with modified Quiet Start

In this section we consider the influence from the partially conducting containers as shown in Fig. 3.1, where $\eta_I = \eta_{II} = \eta_{\text{Fe}} = 5.73 \times 10^3$ cm^{2}s^{-1} is the resistivity of the stainless steel and $\rho_I = \rho_{II} = \rho_{\text{Fe}} = 7.8$ gcm^3 is the density of the stainless steel. Since our experimental facility currently can only reach 60% run ($\Omega_1/2\pi = 2400$ rpm, $\Omega_2/2\pi = 319.8$ rpm, $\Omega_3/2\pi = 1092$ rpm, $\Omega_4/2\pi = 390$ rpm), in this whole section we will focus on 60% run simulations.

3.3.1 Partially Conducting Boundary Condition

If the container is not perfectly insulating, the radial magnetic angular momentum flux at the cylinders is no longer zero. This non-zero magnetic coupling of the fluid to the cylinders (steel walls) can modify the background state on which the instability grows. Thus a partially conducting boundary condition is an issue worthy of noting [46].

Fortunately, at the frequencies relevant to Princeton MRI experiment (60% run) ($f \sim 0.3\,\mathrm{Hz}$), the skin depth of stainless steel $\delta_w = \sqrt{\eta_{\mathrm{Fe}}/\pi f \mu_0} \approx 22\,\mathrm{cm}$, which is much larger than the thickness of the steel vessel surrounding the gallium in the experiment, $d_w \approx 1.0\,\mathrm{cm}$, so that the magnetic field diffuses rather easily into the boundary. If one considers axial currents, the gallium and the steel wall act as resistors in parallel; taking into account their conductivities and radial thickness, one finds that the resistances of steel walls are much larger than the resistance of the liquid gallium [$R_I : R_{II} : R_{III} = 65 : 1 : 21$; see Fig. 3.1 for the subscripts]. Therefore, the currents carried by the steel walls could be neglected for the toroidal field, and the boundary condition is very close to the perfectly insulating boundary condition as discussed before.

The linear growth rate and saturated final state based on partially conducting boundary condition differs slightly from the results based on perfectly insulating boundary condition (the linear growth rate is reduced from 3.3 s^{-1} with perfectly insulating walls to 3.1 s^{-1}) with partially conducting walls, which verifies our argument.

3.3.2 Adjusted Quiet Start

In the §3.2, all simulations are started from an ideal Couette state. However with two split end caps, this state is not the hydrodynamical equilibrium state of the system any more. In order to start with a hydrodynamic equilibrium state, we run the code

for 15 seconds (Basically it is Reynolds number dependent. The Ekman time is on the order of $h/(\nu\bar{\kappa})^{1/2}$. 15 seconds are long enough for $Re = 6400$ since the Ekman time is about 0.9 seconds given $Re = 6400$) without the magnetic field to wait the system to relax to an equilibrium state, just like in the experiment, after spinning the cylinders for about 2 minutes without any magnetic field, then suddenly turning on the magnetic field. This initial state is defined as *quiet start*

However, our pure hydrodynamical simulation shows that the initial equilibrium state of a 60% run has a large $\widetilde{v}_r$ near the outer cylinder which commences an initial jump and shortens, or even eliminates the linear phase (Fig. 3.19). This simulation result conflicts observation that the pure hydrodynamical final state has small v_r fluctuation with Reynolds number as high as 2×10^6 [26], thought the rotation profile of the end caps is not the one specified in the simulation. The difference between them might be because our simulations are 2-D and the Reynolds number is not so high that we have a laminar boundary layer (Reynolds number of the boundary layer $Re_\delta = \sqrt{Re} = 80$) [90], which under experimental parameters should be turbulent ($Re_\delta = \sqrt{Re} \gtrsim 10^3$).

In order to recover the linear phase, we adjust the rotation profile on the end caps a bit: $\Omega_1/2\pi = 2400$ rpm, $\Omega_2/2\pi = 319.8$ rpm, $\Omega_3/2\pi = 1001$ rpm, $\Omega_4/2\pi = 390$ rpm to have a small $\widetilde{v}_r$ near the outer cylinder (Fig. 3.20).

From Fig. 3.20, we can see that the magnitude and fluctuation level of v_r near the outer cylinder is much reduced while the azimuthal velocity is still quite close to the ideal Couette state. We will start the simulation from this state. This initial state is thus defined as *adjusted quiet start*

3.3.3 Linear phase

Fig. 3.21 displays the time evolution of B_r sampled outside the fluid. The linear phase is readily apparent. The growth rate γ is reduced from 3.1 s^{-1} starting from

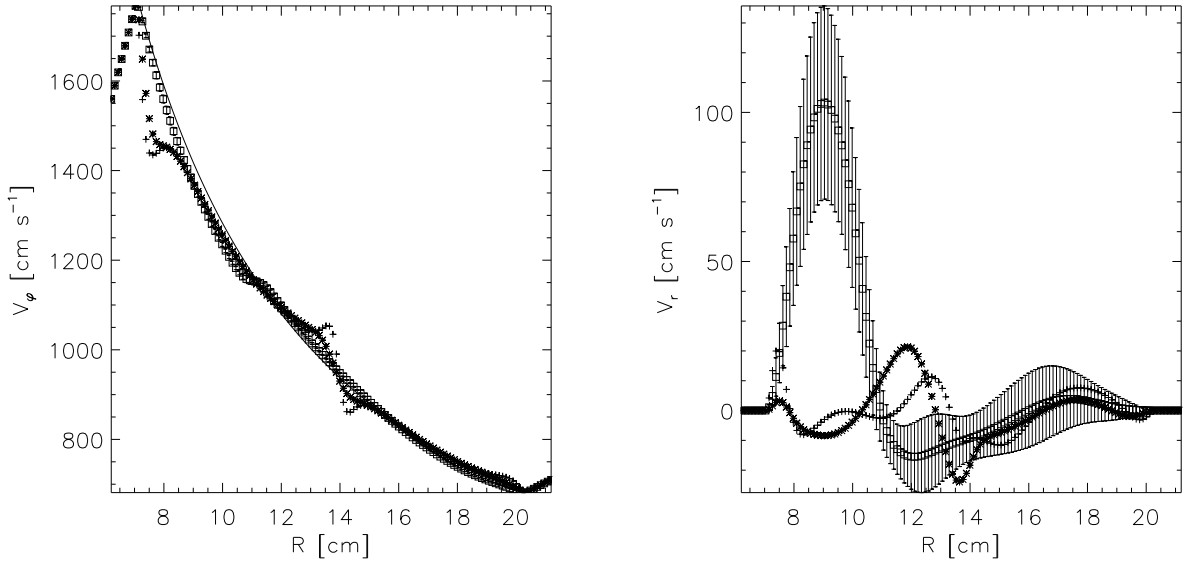

Figure 3.19: 60% pure hydrodynamic run. Initial azimuthal and radial velocity profile of the quiet start with $\Omega_1/2\pi = 2400$ rpm, $\Omega_2/2\pi = 319.8$ rpm, $\Omega_3/2\pi = 1092$ rpm, $\Omega_4/2\pi = 390$ rpm at several heights (cm), for $Re = 6400$. Solid line, ideal Couette state; $+$, 1.31 cm; $*$, 2.72 cm; $\Box$, 13.95 cm with error bars, which is the standard time-variation. "Bottom end cap" is located at $z = 0$. Height $h = 27.9$ cm. Left panal: V_φ; right panel: V_r.

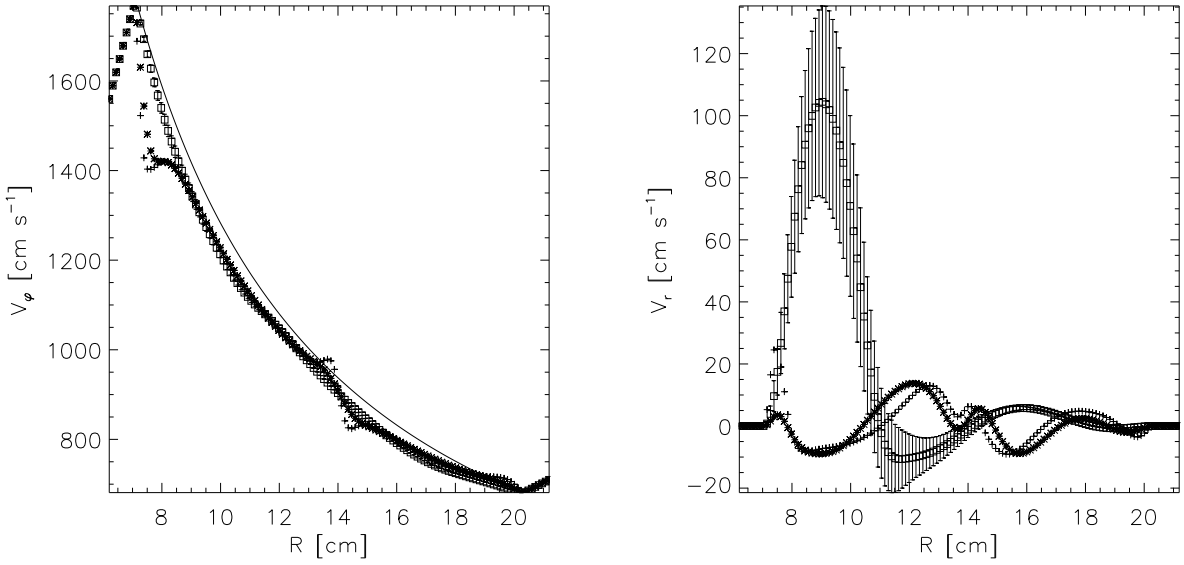

Figure 3.20: 60% pure hydrodynamic run. Initial azimuthal and radial velocity profile of the adjusted quiet start with $\Omega_1/2\pi = 2400$ rpm, $\Omega_2/2\pi = 319.8$ rpm, $\Omega_3/2\pi = 1001$ rpm, $\Omega_4/2\pi = 390$ rpm at several heights (cm), for $Re = 6400$. Solid line, ideal Couette state; $+$, 1.31 cm; $*$, 2.72 cm; $\Box$, 13.95 cm with error bars, which is the standard time-variation. "Bottom end cap" is located at $z = 0$. Height $h = 27.9$ cm.left panal: V_φ; right panel: V_r.

ideal Couette state ($\Omega_1/2\pi = 2400$ rpm, $\Omega_2/2\pi = 319.8$ rpm, $\Omega_3/2\pi = 1092$ rpm, $\Omega_4/2\pi = 390$ rpm) to 2.46 s^{-1} starting from the hydrodynamic equilibrium state with adjusted rotation profile ($\Omega_1/2\pi = 2400$ rpm, $\Omega_2/2\pi = 319.8$ rpm, $\Omega_3/2\pi = 1001$ rpm, $\Omega_4/2\pi = 390$ rpm), which is reasonable, provided that the background rotation flow profile has been modified.

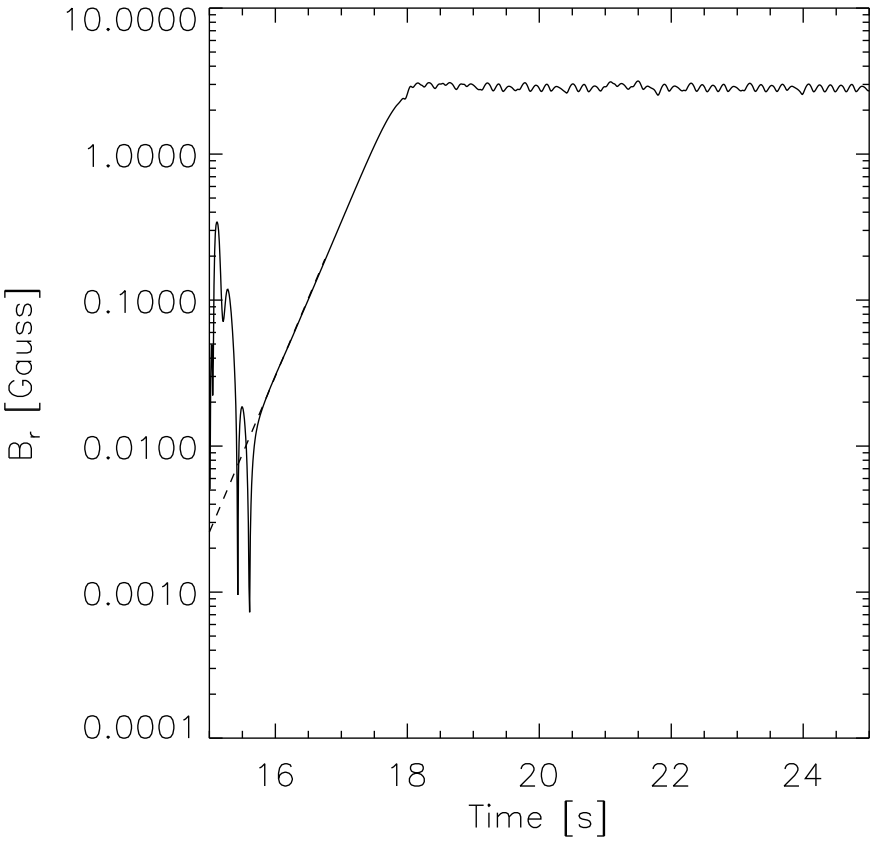

Figure 3.21: 60% run (MRI unstable) and $I_\varphi = 1000$ A. B_r *vs.* time for $Re = 6400$, $Re_m = 9.7$ sampled outside at $z = 13.95$ cm, $r = 25.0$ cm."Bottom end cap" is located at $z = 0$. Height $h = 27.9$ cm. Growth rate $\gamma = 2.46$ s^{-1}.

3.3.4 Structure of the final state

Fig. 3.22 shows the time averaged final state after saturation. Again one inflowing "jet" is observed though it is not as clear as Fig. 3.6 since the instability is much weaker. The horizontal field is perturbed about 2%: $B_{\varphi,\max} \approx 0.02 B_z$ ($Re_m = 9.7$, 60% run).

3.3.5 Angular momentum transport

Just as in §3.2.2, Fig. 3.23 displays the r-profiles of the radial advective, viscous, and magnetic angular momentum fluxes integrated over cylinders coaxial with the boundaries.

Again the profile of the total radial torque verifies our discussion of the poloidal circulation pattern of the flow (§3.2.2 and §3.2.2). Comparing to the initial state, which is before the magnetic field is applied (left panel of Fig. 3.23), the radial advective and viscous torques of the final state, especially the former, are significantly increased at intermediate radii (right panel of Fig. 3.23), which means the middle clockwise cell is even enhanced by the magnetic field and transports more angular momentum. All components of the radial torques of the final state are positive except near r_2. Note how small the radial magnetic torque is compared to the total torque. This indicates that for the 60% runs the influence of the magnetic field is negligible. Most of the angular momentum is possibly transported by the residual magnetic Ekman circulation rather than MRI.

Fig. 3.24 displays the z-profiles of the vertical advective, viscous, and magnetic angular momentum fluxes integrated over radius.

Again from these two figures, the global angular momentum is still transported from the inner cylinder to the outer cylinder and little is transported to the end caps, which is the same as the runs starting from an initial Couette profile and with perfectly insulating boundaries on all sides.

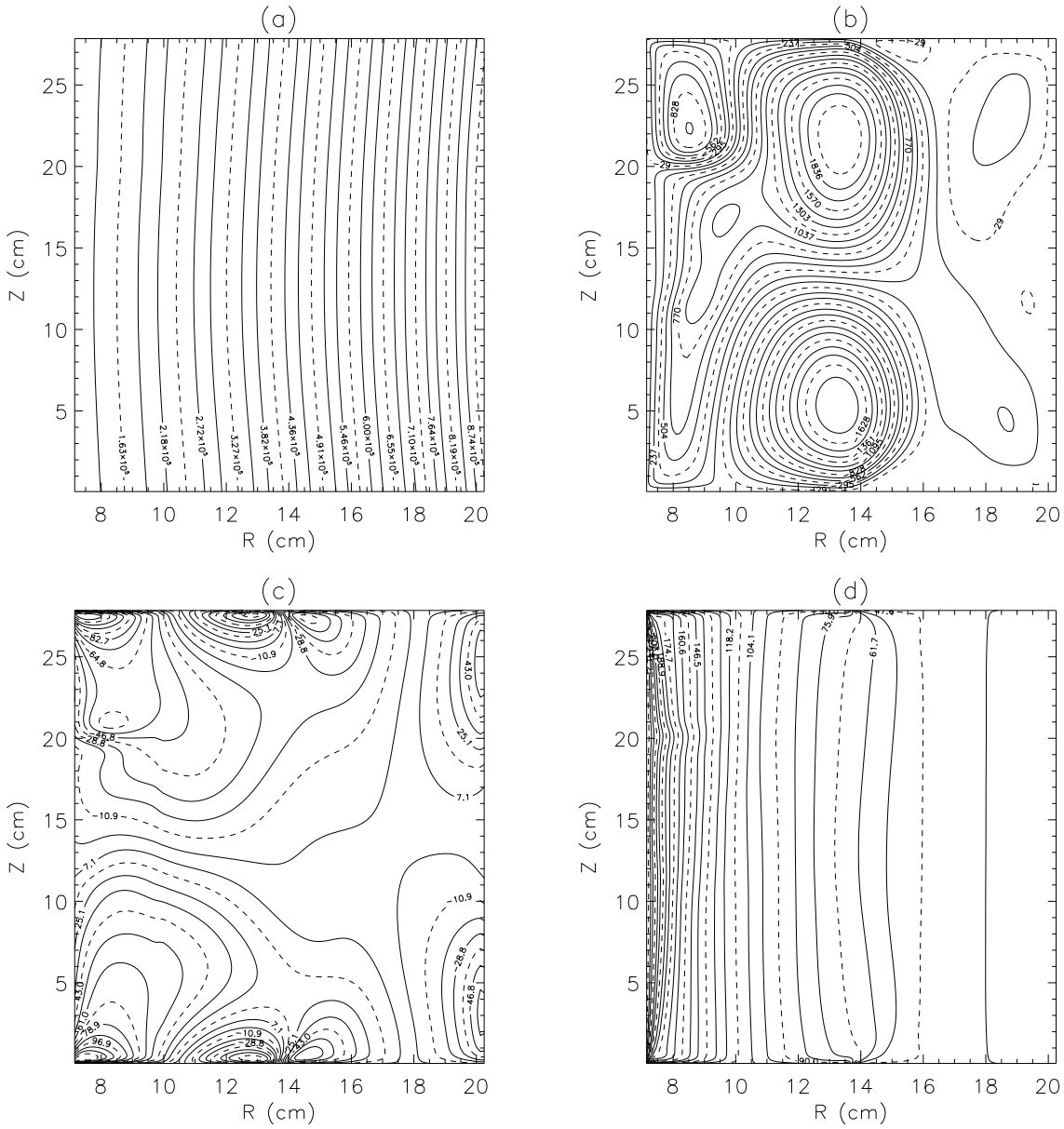

Figure 3.22: 60% run (MRI unstable) and $I_\varphi = 1000$ A. Contour plots of final-state velocities and fields. $Re = 6400$, $Re_m = 9.7$. (a) Poloidal flux function Ψ (Gauss cm^2) (b) Poloidal stream function $\Phi\,(\mathrm{cm^2 s^{-1}})$ (c) toroidal field B_φ (Gauss) (d) angular velocity $\Omega \equiv r^{-1}V_\varphi\,(\mathrm{rad\,s^{-1}})$

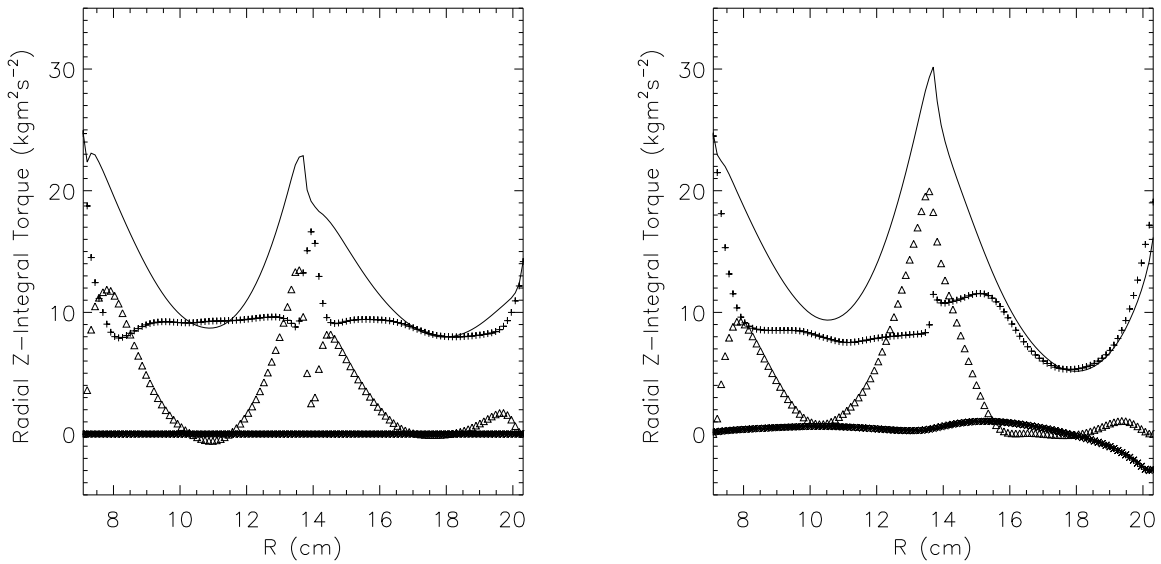

Figure 3.23: 60% (MRI unstable) and $I_\varphi = 1000$ A. z-integrated radial angular momentum fluxes versus r. $Re = 6400$, $Re_m = 9.7$. Left panel: initial state ($\Lambda = 0$); right: final state ($\Lambda = 0.59$). $+$, viscous torque; $*$, magnetic torque; $\triangle$, advective torque; solid line, total torque.

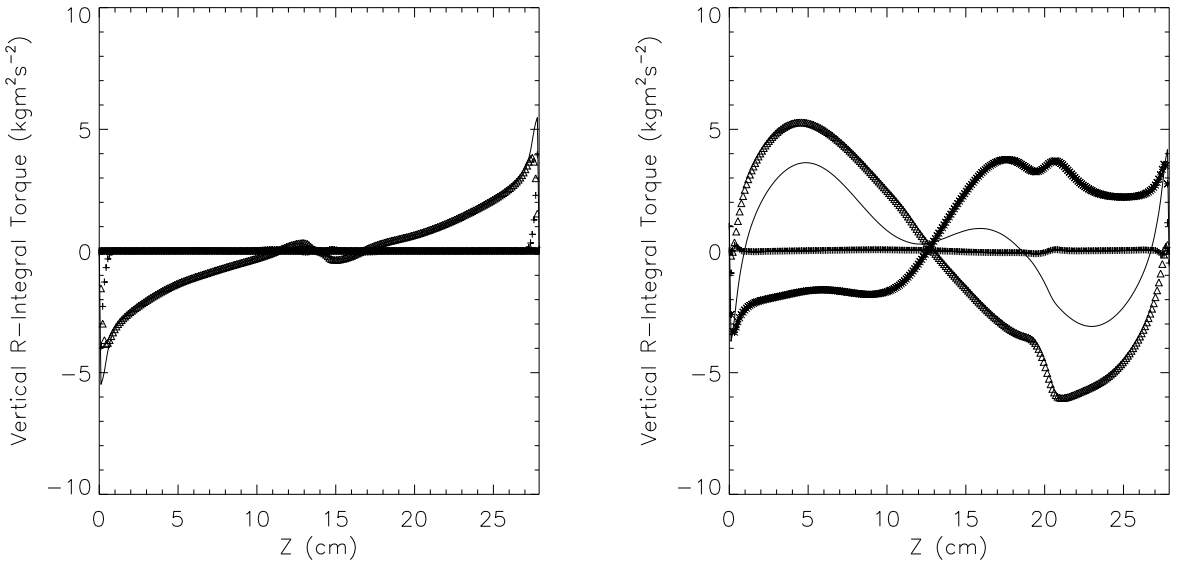

Figure 3.24: 60% run (MRI unstable) and $I_\varphi = 1000$ A. r-integrated vertical angular momentum fluxes versus z. $Re = 6400$, $Re_m = 9.7$. Left panel: initial state ($\Lambda = 0$); right: final state ($\Lambda = 0.59$). $+$, viscous torque; $*$, magnetic torque; $\triangle$, advective torque; solid line, total torque.

The left panel of Fig. 3.25 shows that for 60% runs even at the highest Reynolds number simulated, the magnetic field scarcely affects the total torque, and to the extent that there is an effect, it is a slight reduction. This implies that for the 60% runs the angular momentum transport in the system is mostly due to the residual magnetic Ekman circulation rather than MRI. However for 100% runs similar conclusions as in §3.2.2 are deduced, though the exponent of the initial state is increased from -0.691 to -0.665. Therefore a even smaller difference of the exponents is observed.

Combining the analysis of §3.2.2, we can summarize the conclusions about the angular momentum transport as follows: (a) At the Reynolds number Re available to the simulations and for the 60% runs, linear MRI can be seen at early times, but the contribution of MRI-driven turbulence (or circulation) to angular-momentum transport cannot be seen unambiguously in the final state. (b) 100% runs are more favorable in observing the angular momentum transport enhanced by MRI, though not conclusively.

3.3.6 Summary of adjusted quiet start studies with partially conducting boundary condition

In conclusion, in this section we have simulated the nonlinear development of magnetorotational instability in a nonideal magnetohydrodynamic Taylor-Couette flow. The simulations mimic an on-going experiment and include the conductivity of the stainless steel walls and start the simulation from an adjusted quiet state with split end caps. We have also restricted our study to smaller fluid Reynolds number (Re) than in the experiment, however we have used exactly the same magnetic Reynolds number (Re_m).

We derive the following conclusions:

1. The stainless steel wall is not important in this experiment.

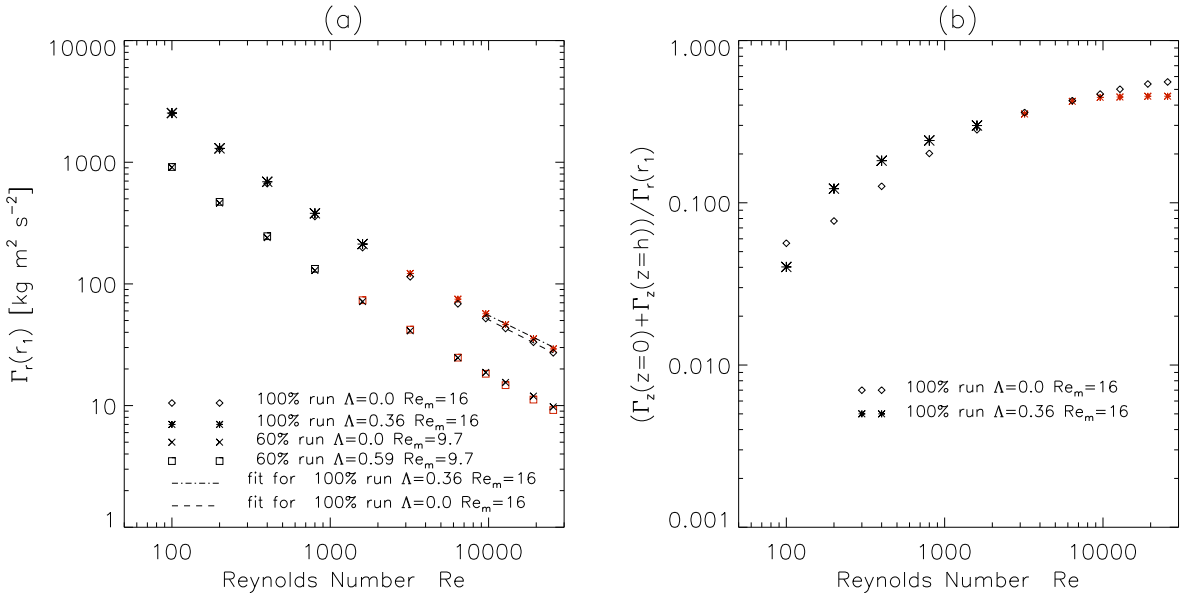

Figure 3.25: The same as Fig. 3.17. But the simulated results in this figure start from an hydrodynamical equilibrium state with adjusted rotation profile at the end caps, which is different from Fig. 3.17. Again in the simulations the magnetic diffusivity η is fixed to the experimental value $\eta = 2,430$ cm^2 s^{-1} (Table.3.1), however the kinetic viscosity is changeable for the purpose of extrapolation. In panel (a), dashed lines have slopes of -0.665 (initial state) and dash-dot lines -0.639 (final state).

2. A linear phase is recovered after the rotation profile is adjusted and the growth rate is reduced due to the adjusted background state (60% run).

3. In the final state one inflowing "jet" is also observed near the inner cylinder but not so clearly due to a weaker instability (60% run).

4. Angular momentum is transported outward. Compared to the initial hydrodynamic equilibrium state, the radial advective and viscous torques of the final state are significantly increased at intermediate radii, which is resulted from the enhanced middle cell. The middle cell is enhanced horizontally by MRI, vertically by the residual magnetic Ekman circulation.

5. The angular momentum transport is dominated by the residual magnetic Ekman circulation at least for 60% run with the Reynolds number accessible in the simulations. 100% runs are more favorable in observing the angular momentum transport enhanced by MRI.

6. The final state contains horizontal fields about 2% as large as the initial poloidal field for 60% run, $Re_m \approx 9.7$.

Chapter 4

Helical MRI[1]

As discussed in §1.4.1, the challenge for experimentation, however, is that liquid-metal flows are very far from ideal on laboratory scales. The experiment is complicated by this extremely large Reynolds number including Ekman circulation and Stewartson layers [50] even though the experimental apparatus has been designed to minimize the circulation (*e.g.* by the use of independently controlled split endcaps).

Recently, Hollerbach and collaborators (Fig. 4.1) have discovered that MRI-like modes may grow at much reduced Re_m and S in the presence of a helical background field, a current-free combination of axial and toroidal field [40, 41].

$$\boldsymbol{B}^{(0)} = B_z^{(0)} \left(\boldsymbol{e}_z + \beta \frac{r_1}{r} \boldsymbol{e}_\varphi \right) , \tag{4.1}$$

in cylindrical coordinates (r, φ, z), where $B_z^{(0)}$ and β are constants. (When it will not cause ambiguity, we will omit the superscript (0) from $\boldsymbol{B}$ and B_z hereafter.) Henceforth, "standard MRI" (SMRI) will refer to cases where the $\beta = 0$, and "helical MRI" (HMRI) to modes that require $\beta \neq 0$. In centrifugally stable flows—meaning that $d(r^2\Omega)^2/dr > 0$, where $\Omega = V_\varphi^{(0)}/r$ is the background angular velocity—SMRI exists only when Re_m and S exceed thresholds of order unity [52, 53]. Remarkably,

[1] inherited and modified from Liu et al. [45]

however, HMRI may persist in such flows even as both parameters tend to zero, though not independently: more precisely, the thresholds are $\ll 1$ and would vanish as long as Re is above a critical value. In a fixed geometry and flow profile, the resistive limit may be approached theoretically by increasing η with all other parameters held constant. The growth rate of inviscid HMRI is then $\propto \eta^{-1}$ so that the hydrodynamic case is approached continuously. The special case of toroidal-only magnetic field ($\beta = \infty$) is stable [91].

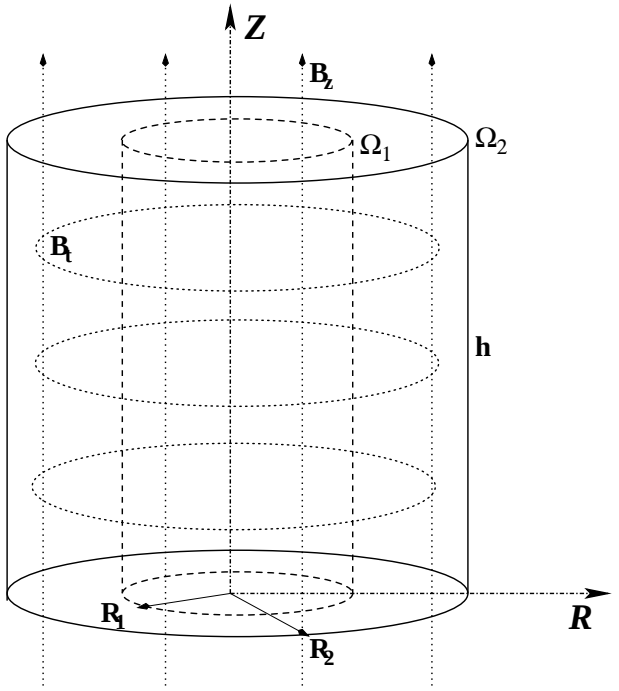

Figure 4.1: Diagram of Helical MRI. The radial boundaries are assumed to be electrically conducting while the vertical boundaries are assumed to be electrically insulating.

Our own interest in HMRI stems as much from astrophysical as from experimental considerations. Accretion disks composed of substantially ionized plasma tend to be in the ideal MHD limit: $Re_m \gg 1$ and $S \gg 1$; also $Pr_{\rm m} \gg 1$. The disks around protostars, in which planets form, are cool and very weakly ionized, however. If their ionization fractions followed thermal equilibrium, such disks would be far too resistive for SMRI, but the actual resistivity is uncertain because it involves stellar

X-rays and other non-thermal sources of ionization, as well as recombination rates that are sensitive to the unknown abundance of small dust grains [56, 92]. The fluid Reynolds number of protostellar disks is in any case very large, $Re \sim 10^{12}$, and therefore $Pr_{\rm m}$ is surely even smaller than in liquid metals.

A novel feature of the background state for HMRI is that there is a uniform axial flux of angular momentum carried by the field, $rT_{\varphi z}^{(\rm mag)} = -rB_\varphi B_z/\mu_0$ and an associated axial Poynting flux Ω times this. In an infinite or periodic cylinder, the question of the sources and sinks of these axial fluxes need not arise, but in an experimental device, a torque is exerted by the axial field on the radial sections of the coil that complete the circuit containing the axial current. Related to this perhaps, the dispersion relation for linear modes is sensitive to the sign of the axial wavenumber (k_z), and the instabilities of axially infinite or periodic cylinders are travelling rather than standing waves, as noted by Knobloch [30, 93]. This begs the question what should happen to the modes in finite cylinders, a question that has motivated much of our analysis.

Even the analysis for periodic cylinders implies two practical difficulties for an HMRI experiment. First, as will be seen, the typical growth rates tend to be smaller than those of SMRI except in regimes where SMRI would also be unstable. This is largely a consequence of looking for HMRI at lower rotation rates; when normalized to the rotation rates of the cylinders, the growth rates of HMRI and resistive SMRI can be comparable. In practice, the ease with which growth can be discerned probably depends less upon the ratio γ/Ω of growth rate to rotation rate than upon γt_E, where t_E is the Ekman circulation time. Since $\Omega t_E \propto Re^{1/2}$, Ekman circulation may be more problematic at the lower Reynolds numbers where HMRI is unstable but SMRI is not. A second difficulty is the axial current needed for the required toroidal fields tend to be quite large: $I[\,\mathrm{kA}] = 5B_\varphi r[\mathrm{kG\text{-}cm}]$. This is partly offset by the low Re and Re_m needed for HMRI, which permits a radially compact apparatus. Despite these

difficulties, experimental verification of HMRI has already been claimed in a recent paper[42].

4.1 Periodic cylinder

4.1.1 Linear theory for periodic cylinder

All magnetic fields are expressed as Alfvén speeds, in other words, units such that $\mu_0 = 1/\rho$ are used. Upper-case letters are used for the background magnetic field (4.1) and velocity $\boldsymbol{V} = r\Omega(r)\boldsymbol{e}_\varphi$, and lower-case $(\boldsymbol{b}, \boldsymbol{v})$ for perturbations. Frequently occurring derivatives are abbreviated by $\partial_r^\dagger \equiv \partial_r + r^{-1}$, $D \equiv \partial_r\partial_r^\dagger + \partial_z^2$. Incompressibility allows the use of stream functions for the poloidal components: $v_r = \partial_z\phi$, $v_z = -\partial_r^\dagger\phi$, $b_r = \partial_z\psi$, $b_z = -\partial_r^\dagger\psi$; note that these definitions differ by factors of r from the usual ones. The linearized inviscid MHD equations

$$\begin{aligned} \dot{\boldsymbol{B}} + \boldsymbol{V}\cdot\boldsymbol{\nabla}\boldsymbol{B} - \boldsymbol{B}\cdot\boldsymbol{\nabla}\boldsymbol{V} &= \eta\nabla^2\boldsymbol{B}\,, \\ \dot{\boldsymbol{V}} + \boldsymbol{V}\cdot\boldsymbol{\nabla}\boldsymbol{V} + \boldsymbol{\nabla}\frac{P}{\rho} + \boldsymbol{B}\times(\boldsymbol{\nabla}\times\boldsymbol{B}) &= 0\,. \end{aligned}$$

then become, since B_z and rB_φ are constant,

$$(\partial_t - \eta D)b_r - B_z\partial_z v_r = 0\,, \quad (4.2)$$

$$(\partial_t - \eta D)b_\theta - 2r^{-1}B_\theta v_r - b_r r\Omega' - B_z\partial_z v_\theta = 0\,, \quad (4.3)$$

$$\partial_r^\dagger b_r + \partial_z b_z = 0\,, \quad (4.4)$$

$$\partial_t v_r - 2\Omega v_\theta + \partial_r\left(\rho^{-1}p + B_\theta b_\theta\right) + 2r^{-1}B_\theta b_\theta + B_z(\partial_r b_z - \partial_z b_r) = 0\,, \quad (4.5)$$

$$\partial_t v_\theta + r^{-1}(r^2\Omega)' v_r - B_z\partial_z b_\theta = 0\,, \quad (4.6)$$

$$\partial_t v_z + \partial_z\left(\rho^{-1}p + B_\theta b_\theta\right) = 0\,, \quad (4.7)$$

$$\partial_r^\dagger v_r + \partial_z v_z = 0\,. \quad (4.8)$$

Eliminating v_z between (4.7) & (4.8) leads to

$$\partial_z^2 \left(\rho^{-1} p + B_\theta b_\theta\right) = \partial_r^\dagger \partial_t v_r \,,$$

which can be used to eliminate p from (4.5), and if one also eliminates b_z using (4.4), the result is:

$$(\underline{\partial_t} - \eta D)\psi = B_z \partial_z \phi \,, \tag{4.9}$$

$$(\underline{\partial_t} - \eta D) b_\varphi = \partial_z \left(\frac{2B_\varphi}{r}\phi + B_z v_\varphi + \underline{r\Omega'\psi} \right) \,, \tag{4.10}$$

$$\partial_t D\phi - 2\Omega \partial_z v_\varphi = B_z \partial_z D\psi - \frac{2B_\varphi}{r}\partial_z b_\varphi \,, \tag{4.11}$$

$$\partial_t v_\varphi + r^{-1}(r^2\Omega)' \partial_z \phi = B_z \partial_z b_\varphi \,. \tag{4.12}$$

The underlined terms above are negligible in the resistive limit, where $\boldsymbol{b}$ scales $\propto \eta^{-1}$ compared to $\boldsymbol{v}$. Neglecting these terms has been shown to suppress SMRI [53, 94], but not HMRI as will be seen.

Taking another time derivative of (4.11) and eliminating $\partial_t v_\varphi$ *via* (4.12) yields

$$\left(\partial_t^2 D + \kappa^2 \partial_z^2\right)\phi = B_z \partial_z \partial_t D\psi + 2\left(\Omega B_z \partial_z^2 - \frac{B_\varphi}{r}\partial_z \partial_t\right) b_\varphi \,, \tag{4.13}$$

in which $\kappa^2 \equiv r^{-3} d(r^2\Omega)^2/dr^2$ is the square of the epicyclic frequency. As $\eta \to \infty$, (4.13) reduces to

$$\left(\partial_r \partial_r^\dagger + \partial_z^2\right)\partial_t^2 \phi \; + \kappa^2(r)\partial_z^2 \phi = 0 \,. \tag{4.14}$$

4.1.2 WKB for infinite or periodic cylinders

If we take the gap to be narrow, $d \equiv r_2 - r_1 \ll r$, then it is reasonable to treat r, B_z, Ω, $r\Omega' = 2Ro\Omega$, and $r^{-1}(r^2\Omega)' = 2(1+Ro)\Omega = \kappa^2/2\Omega$ as constants, and to look for perturbations $\propto \exp(ik_r r + ik_z z - i\omega t)$. The Rossby number $Ro \equiv \frac{1}{2} d\ln\Omega / d\ln r$

has been introduced. In this case one expects to have WKB solutions with D replaced by $-(k_r^2 + k_z^2) \equiv K^2$, where the total wavenumber $K = O(d^{-1})$.

When applied to (4.14) (*i.e.* for $\eta \to \infty$) these prescriptions yield the dispersion relation for hydrodynamic inertial oscillations (hereafter IO),

$$\omega_{\rm IO}^2 = \kappa^2 \frac{k_z^2}{k_r^2 + k_z^2} \quad \text{where} \quad \kappa^2 = \frac{1}{r^3}\frac{d}{dr}(r^2\Omega)^2 = 4(1+Ro)\Omega^2. \tag{4.15}$$

IO exist only in the Rayleigh-stable regime $\kappa^2 > 0$, $Ro > -1$, and their frequencies lie between 0 and κ.

HMRI occurs at finite η when $B_\varphi/r \equiv \omega_\theta$ is comparable to $k_z B_z \equiv \omega_z$. Define $\omega_\eta \equiv \eta K^2$ and $\mu \equiv k_z/|K| \in [-1, 1]$. The dispersion relation corresponding to the system (4.9)-(4.12) is then

$$\begin{aligned} 0 = s^4 + 2\omega_\eta s^3 + \left[\omega_\eta^2 + 4\mu^2\omega_\theta^2 + 2\omega_z^2 + \mu^2\kappa^2\right] s^2 \\ + 2\left[2\omega_\eta\mu^2\omega_\theta^2 + \omega_\eta\omega_z^2 + \omega_\eta\mu^2\kappa^2 - 4i\mu^2\omega_\theta\omega_z\Omega\right] s \\ + \left[\omega_\eta^2\mu^2\kappa^2 - 4i\omega_\eta\omega_\theta\omega_z\mu^2\Omega(2+Ro) + \omega_z^4 + 4\mu^2\omega_z^2\Omega^2 Ro\right] , \end{aligned} \tag{4.16}$$

where the complex growth rate $s \equiv -i\omega$ has been used so that the coefficients are all real except for those linear in ω_θ. It is instructive to consider the limit in which ω_η is much larger than all of the other frequencies, including ω:

$$s^2 + \omega_{\rm IO}^2 \; + 2\omega_\eta^{-1}\left[s^3 + (2\mu^2\omega_\theta^2 + \omega_z^2 + \omega_{\rm IO}^2)s - 2i\omega_\theta\omega_z\mu^2\Omega(2+Ro)\right] \;\approx\; O(\omega_\eta^{-2})\,. \tag{4.17}$$

The replacement $\mu^2\kappa^2 \to \omega_{\rm IO}^2$ emphasizes that $\omega \approx \pm\omega_{\rm IO}$ in this limit. The roots are

$$\omega \approx \mp\omega_{\rm IO} \; + i\omega_\eta^{-1}\left[\pm 2\omega_\theta\omega_z\omega_{\rm IO}^{-1}\mu^2\Omega(2+Ro) \; - \left(2\mu^2\omega_\theta^2 + \omega_z^2\right)\right] \; + O(\omega_\eta^{-2})\,, \tag{4.18}$$

the bivalent signs being correlated. The other two roots of (4.16) represent rapidly

decaying magnetic perturbations, $s \approx -\omega_\eta$.

We conclude that *in highly resistive flow, HMRI reduces to a weakly destabilized inertial oscillation.* In the present inviscid approximation, instability persists to arbitrarily large resistivity, though with reduced growth rate. Furthermore, we note from (4.18) that instability [*i.e.* $\Im(\omega) > 0$] occurs only if the bivalent signs are chosen so that $\Omega B_\varphi B_z k_z / \Re(\omega) < 0$, which implies that *the unstable mode propagates axially with the same sense as the background Poynting flux.* [From (4.15), the group velocity $\partial\Re(\omega)/\partial k_z$ and phase velocity $\Re(\omega)/k_z$ have the same sign.] Although we have derived this propagation rule in the resistive limit, numerical evidence indicates that it is true of the full dispersion relation (4.16), as demonstrated by Figure. 4.2.

In terms of the original variables, the approximate growth rate ((4.18)) is

$$\mathrm{Real}(s) \approx \frac{k_z^2}{K^2}\frac{B_z^2}{\mu_0\rho\eta}\left[\frac{2+Ro}{\sqrt{1+Ro}}\left(\frac{|B_\theta/B_z|}{Kr}\right) \; -1 \; -2\left(\frac{|B_\theta/B_z|}{Kr}\right)^2\right]. \qquad (4.19)$$

Here $K = (k_r^2 + k_z^2)^{1/2}$, and for application to our experiment,

$$k_r \to \frac{\pi}{r_2 - r_1} \quad \bar{r} \to \frac{r_1 + r_2}{2} \quad k_z \to \frac{n\pi}{h}\,.$$

With our dimensions, $k_r \bar{r} \approx 1.04\pi$, so the above becomes, roughly,

$$660 B_z^2 \frac{n^2}{n^2+4.5}\left[\left(\frac{|B_\theta/B_z|}{\pi\sqrt{4.5n^2+1.1}}\right)\frac{2+Ro}{\sqrt{1+Ro}} \; -1 \; -2\left(\frac{|B_\theta/B_z|}{\pi\sqrt{4.5n^2+1.1}}\right)^2\right] \; \mathrm{s}^{-1}\,,$$

where B_z is in Tesla.

Instability requires the square brackets in (4.18) to be positive, whence

$$2(\mu\omega_\theta)^2 \; \pm \frac{2+Ro}{\sqrt{1+Ro}}\omega_z(\mu\omega_\theta) \; + \omega_z^2 \; < \; 0\,.$$

The inequality is possible if and only if the discriminant of the lefthand side, regarded

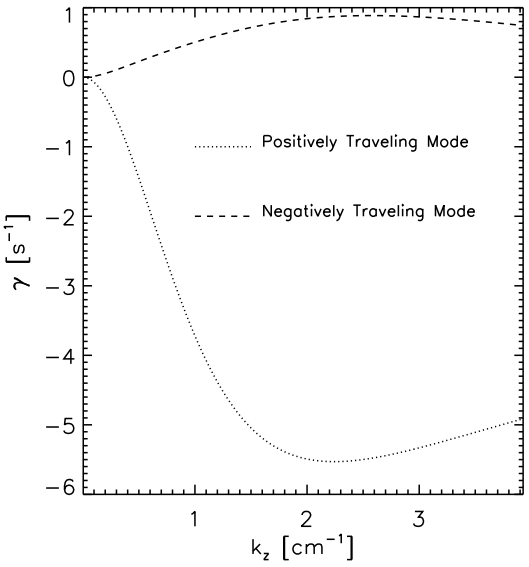

(a) Growth rate $\gamma = \Im\omega$ vs. wave number k_z

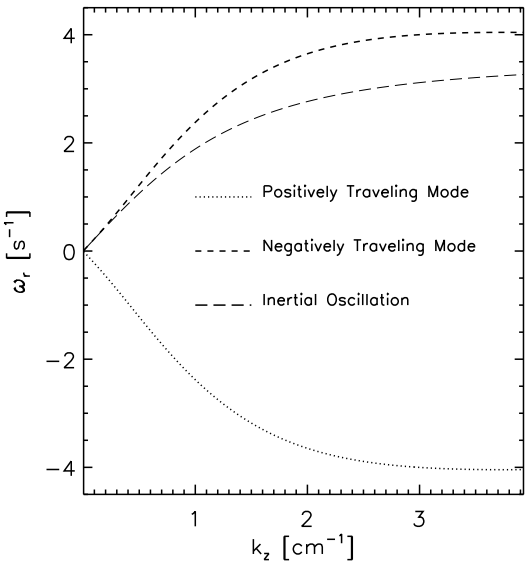

(b) Real frequency $\omega_r = \Re\omega$ vs. wave Number k_z

Figure 4.2: Selected roots of full dispersion relation (4.16) for $\eta = 2,000\,\mathrm{cm}^2\,\mathrm{s}^{-1}$ [gallium], $r_1 = 9\,\mathrm{cm}$, $r_2 = 11\,\mathrm{cm}$, vertical periodicity $2h = 16\,\mathrm{cm}$, $\Omega_1 = 100\,\mathrm{rpm}$, $\Omega_2 = 68.1\,\mathrm{rpm}$, $B_z = 500\,\mathrm{G}$, $B_\varphi = 10\,\mathrm{kG}$ at $r = (r_1 + r_2)/2$. The two rapidly damped modes are omitted.

as a quadratic equation in $\mu\omega_\theta$, is positive:

$$\frac{(2+Ro)^2}{1+Ro}\omega_z^2 \; - 8\omega_z^2 > 0\,,$$

which translates to

$$Ro < 2(1-\sqrt{2}) \approx -0.8284 \quad \underline{\text{or}} \quad Ro > 2(1+\sqrt{2}) \approx 4.8284\,. \tag{4.20}$$

Thus, within WKB, at least for highly resistive but inviscid flow ($Re_m, S \to 0^+$, $Re \to \infty$), *the Keplerian value $Ro = -3/4$ is excluded, as of course is uniform rotation ($Ro = 0$).* We say "of course" because, the background being current free, the only source of free energy is the shear.

Recently Rüdiger and Hollerbach [95] show that if at least one of the boundaries is sufficiently conducting, the HMRI does exist even for rotation profiles as flat as

Keplerian, which conflicts with the above conclusions. The loophole they have found is a small one, and unlikely to be important in astrophysics. However, it might be achieved in a low-plasma-beta but highly resistive (weakly ionized) plasma. Under the parameters used in the preprint [95] ($Re_m = 0$, $S = 0$, $Pr_{\rm m} = 0$ but finite Re), the authors are indeed taking the diffusivity to infinity. Note however that the combination $Ha^2/2Re = (V_A)^2/(2\Omega\eta)$, which is the Elsasser number. The authors consider Ha and Re to be constant as $Pr_{\rm m} \to 0$; thus if we think of Ω and ν as fixed, then the Alfven speed must scale like $\sqrt{\eta}$ as $\eta \to \infty$. So, the authors are considering a limit in which the Alfven speed is infinitely larger than the rotation speed but poorly coupled to the flow, whereas in this chapter we were thinking of the resistive limit as one in which the field strength and rotation speed were held fixed as the diffusivity became infinite ($Re_m = 0.1$, $S = 0.03$). In the language of the WKB analysis, the resistive frequency $\omega_\eta \gg \Omega$ while the Alfvenic frequencies ω_z and ω_θ are of order $\sqrt{\omega_\eta \Omega}$. From Eq. 4.16, the WKB HMRI growth rate has a finite nonzero value if the limit is taken in this way.

4.1.3 Numerical results for wide gaps in periodic cylinders

We have adapted a code developed by [53] to allow for a helical field. Vertical periodicity is assumed, but the radial equations are solved directly by finite differences with perfectly conducting boundary conditions. The underlined terms in eqs. (4.9)-(4.12) are retained, and viscous terms are added although their influence is small at Reynolds numbers of interest. The code reproduces published results for marginal stability [40, 41]. Table 4.1 compares the predictions of the WKB dispersion relation (4.16) with those of this code (labeled "Global"). The agreement is reasonably good, considering the crudeness of the WKB approximation. No unstable modes are found for the parameters of Figure 4.2 at $Ro(r_1) \geq -0.80$: the Keplerian value $Ro = -0.75$ is stable.

Astrophysical disks correspond to very wide gaps, $r_2 - r_1 \gg h$, as well as Keplerian rotation. Given $(Re_m, S) = (0.1, 0.03)$ and $r_2/r_1 = 2.0,\ 2.83,\ 5.0$, the maximum unstable Rossby numbers at the inner cylinder are found to be $Ro(r_1) = -0.88$, -0.92, and -0.95, respectively, from our radially global linear code. We conjecture that Keplerian flows—more precisely, flows in which $0 \geq Ro \geq -3/4$ at all radii—are stable for all gap widths. It would be interesting to prove this.

We have also estimated a few growth rates with our nonlinear, compressible non-ideal MHD code [73], which is a modified version of the astrophysical code ZEUS2D [96]. In this case, we use the wide-gap geometry of the Princeton MRI experiment [52, 53], except that the computation uses periodic vertical boundaries: $r_1 = 7.1\,\mathrm{cm}$, $r_2 = 20.3\,\mathrm{cm}$, $h = 27.9\,\mathrm{cm}$, $\Omega_1 = 400\,\mathrm{rpm}$, $\Omega_2 = 53.3\,\mathrm{rpm}$, $B_z = 500\,\mathrm{G}$, $B_\varphi(r_1) = 1\,\mathrm{kG}$; the material properties are again based on gallium: $\eta \approx 2000\,\mathrm{cm^2\,s^{-1}}$, $\nu \approx 3 \times 10^{-3}\,\mathrm{cm^2\,s^{-1}}$. The growth rate and real frequency from the ZEUS2D simulations are respectively $1.06\,\mathrm{s^{-1}}$ and $3.93\,\mathrm{s^{-1}}$, compared to $1.05\,\mathrm{s^{-1}}$ and $3.89\,\mathrm{s^{-1}}$ from the linear code. WKB yields $(\gamma, \omega_r) = (0.41, 3.90)\,\mathrm{s^{-1}}$—not an accurate result for the growth rate, but considering the width of the gap, the agreement is pleasing.

The growth rates in Table 4.1 are of order $1\,\mathrm{s^{-1}}$, as compared to $\sim 30\,\mathrm{s^{-1}}$ for SMRI in this geometry at the full rotation rate and field planned for the Princeton experiment [73]: $\Omega_1 = 4,000\,\mathrm{rpm}$, $\Omega_2 = 533\,\mathrm{rpm}$, $B_z = 5\,\mathrm{kG}$, and $B_\varphi = 0$.

4.2 Finite cylinder with insulating end caps

4.2.1 Finite cylinders: a perturbative approach

In finite nonperiodic cylinders with insulating or partially insulating endcaps, the MHD eigenfunctions are intrinsically two dimensional: they are not separable in r and z. (Separability could be achieved with perfectly conducting endcaps, but then the axial field would be attached to them. This would allow the boundary to exert

Table 4.1: Comparison between WKB and numerical growth rates in a vertically periodic Couette flow with the parameters of Figure 4.2 except for a nonzero viscosity like that of gallium: $\nu = 3.1 \times 10^{-3}$. The mode number $n \equiv k_z h/\pi$.

n	WKB γ $[s^{-1}]$	WKB ω_r $[s^{-1}]$	Global γ $[s^{-1}]$	Global ω_r $[s^{-1}]$
1	0.1612	0.9443	0.0965	1.4004
2	0.3911	1.9182	0.3465	2.5164
3	0.5878	2.7084	0.6031	3.2638
4	0.7387	3.2646	0.7907	3.7094
5	0.8356	3.6221	0.8960	3.9549
6	0.8805	3.8366	0.9339	4.0799
7	0.8829	3.9565	0.9241	4.1352
8	0.8543	4.0166	0.8831	4.1512
9	0.8049	4.0400	0.8227	4.1451

magnetic forces on the fluid, which seems undesirable and in any case is experimentally less realistic than insulating endcaps.) The purely hydrodynamic problem for $\eta = \infty$ *is* separable, however, if viscosity is neglected so that we may assume no-slip boundary conditions. This suggests a perturbative expansion of the eigenvalue problem in η^{-1}—more properly, $(Re_m, S) \to (\epsilon Re_m, \epsilon S)$, with ϵ a small parameter. The cylinders themselves are assumed infinitely long and perfectly conducting; although this is not realistic, it does not result in any attachment of the field to the boundaries, and it allows the magnetic field more easily to be matched onto vacuum solutions that decay as $|z| \to \infty$ in the regions above and below the fluid. The underlined terms in equations (4.9)-(4.12) will be neglected because they contribute to the eigenfrequency only at $O(\eta^{-2})$ and higher orders.

We begin with the zeroth-order problem, *i.e.* for $\eta = \infty$. As noted above, the hydrodynamic boundary conditions

$$\phi = 0 \text{ on } r = r_1, r_2 \text{ and on } z = 0, h\,, \tag{4.21}$$

and inertial-mode equation (4.14) are separable, so we look for an eigenmode of the

form

$$\phi(t,r,z) = e^{-i\omega t}\varphi(r)\sin kz, \qquad k = n\frac{\pi}{h} \equiv k_n\,. \tag{4.22}$$

The radial function $\varphi(r)$ satisfies

$$\frac{d^2\varphi}{dr^2} + \frac{1}{r}\frac{d\varphi}{dr} + \left[k^2\left(\frac{4\mathrm{a}^2}{\omega^2} - 1\right) + \frac{1}{r^2}\left(\frac{4\mathrm{ab}k^2}{\omega^2} - 1\right)\right]\varphi = 0\,, \tag{4.23}$$

assuming a Couette profile $\Omega(r) = \mathrm{a} + \mathrm{b}r^{-2}$ so that $\kappa^2 = 4\mathrm{a}\Omega$, which is satisfied by the Bessel functions $J_\nu(pr)$ & $Y_\nu(pr)$ if

$$\nu^2 \equiv 1 - \frac{4\mathrm{ab}k^2}{\omega^2}\,, \qquad p^2 \equiv k^2\left(\frac{4\mathrm{a}^2}{\omega^2} - 1\right)\,. \tag{4.24}$$

We may thus solve this problem exactly. However, for qualitative information, we notice that if we multiply (4.23) by r it becomes

$$\frac{d}{dr}\left(r\frac{d\varphi}{dr}\right) + \left[\frac{1}{\omega^2}\left(4\mathrm{a}^2k^2r + \frac{4\mathrm{ab}k^2}{r}\right) - \left(\frac{1}{r} + k^2r\right)\right]\varphi = 0\,.$$

This is the same form as the Sturm-Liouville problem

$$\frac{d}{dr}\left(P(r)\frac{d\varphi}{dr}\right) + \left[\lambda R(r) - Q\,(r)\right]\varphi = 0\,,$$

$$\varphi(r_1) = 0, \qquad \varphi(r_2) = 0,$$

where

$$\begin{aligned} P(r) &= r, \\ R(r) &= 4\mathrm{a}^2k^2r + \frac{4\mathrm{ab}k^2}{r} > 0, \\ Q(r) &= k^2r + \frac{1}{r} > 0, \\ \lambda &= 1/\omega^2. \end{aligned}$$

Therefore λ is real and positive ([97, Chapter X]); consequently the frequencies ω which we seek are all real. Furthermore $\lambda R - Q$ must be positive somewhere within the flow, whence $\omega^2 < \max[4a\Omega(r)/(1 + k^{-2}r^{-2})]$. There are no modes which grow in time. Thus we conclude that, *all inviscid axisymmetric modes are neutrally stable in the limit of infinite resistivity.* The coefficient $R(r) = \Psi(r)$, the Rayleigh discriminant, so this result is to be expected.

We may arrange for $\phi(r_1) = 0$ by taking

$$\varphi_{mn}(r) \equiv J_\nu(pr_1)Y_\nu(pr) - Y_\nu(pr_1)J_\nu(pr). \tag{4.25}$$

Since we also require $\phi(r_2) = 0$, the determinant

$$\Delta(\omega, k) \equiv J_\nu(pr_1)Y_\nu(pr_2) - J_\nu(pr_2)Y_\nu(pr_1) \tag{4.26}$$

must vanish. The condition $\Delta = 0$ defines a discrete set of eigenfrequencies $\omega_{1,n} > \omega_{2,n} > \ldots > \omega_{mn} \ldots > 0$ for each $k = k_n$. Let $\phi_{m,n}$ be the complete eigenfunction (4.22) corresponding to a given k_n & $\omega_{m,n}$. We define an inner product [here ϕ_{mn} is defined by (4.22) with $\varphi(r) \to \varphi_{mn}(r)$]

$$\langle \phi_{m'n'}, \phi_{mn} \rangle \equiv \int_0^h dz \int_{r_1}^{r_2} r dr \, \bar{\phi}_{m'n'} \phi_{mn}, \tag{4.27}$$

where the overbar denotes complex conjugation. The eigenfunctions are orthogonal in the sense that $\langle \phi_{mn}, \kappa^2 \phi_{m'n'} \rangle = 0$ if $\omega_{mn}^2 \neq \omega_{m'n'}^2$.

To get the $O(\eta^{-1})$ corrections to ω_{mn}, we must express the magnetic perturbations ψ and b_φ appearing on the righthand of (4.13) in terms of the zeroth-order eigenfunctions ϕ_{mn}. Neglecting the time derivative in (4.9) yields

$$D\psi = -\eta^{-1} B_z \partial_z \phi_{mn}. \tag{4.28}$$

To get b_φ from (4.10), we first use (4.12) to write $v_\varphi \approx (2\mathrm{a}/i\omega_{mn})\partial_z\phi_{mn}$, so that

$$b_\varphi \approx -2\eta^{-1}D_T^{-1}\left(\frac{B_\varphi}{r}\partial_z\phi_{mn} + \frac{iaB_zk_n^2}{\omega_{mn}}\phi_{mn}\right). \tag{4.29}$$

Note that we have replaced ∂_z^2 with $-k_n^2$; we may similarly replace any even power of ∂_z but not an odd power, which changes a $\sin k_n z$ to a multiple of $\cos k_n z$. The operator D_T^{-1} is the inverse of D with the boundary conditions appropriate to b_φ, which are different from those of ϕ [eq. (4.21)]:

$$\partial_r^\dagger b_\varphi = 0 \text{ at } r = r_1, r_2 \quad \text{and } b_\varphi = 0 \text{ at } z = 0, h. \tag{4.30}$$

Using (4.28) & (4.29) to eliminate $D\psi$ and b_φ from (4.13) results in

$$\begin{aligned}&\left(\partial_t^2 D + \kappa^2\partial_z^2\right)\phi = \\ &-i\omega_{mn}\eta^{-1}\left[(k_nB_z)^2 + 4\left(\frac{-iB_\varphi}{r}\partial_z + \frac{\Omega B_zk_n^2}{\omega_{mn}}\right)(-D_T^{-1})\left(\frac{-iB_\varphi}{r}\partial_z + \frac{\mathrm{a}B_zk_n^2}{\omega_{mn}}\right)\right]\phi_{mn}\,.\end{aligned} \tag{4.31}$$

On the righthand side of (4.31), the eigenmode and eigenfrequency have been evaluated to zeroth order in η^{-1}. On the lefthand side, we must consider that $\omega \to \omega_{mn} + \delta\omega$ and $\phi \to \phi_{mn} + \delta\phi$, where $\delta\omega$ and $\delta\phi$ are of first order in η^{-1}. We may obtain an expression for $\delta\omega$ by taking the inner product of (4.31) with ϕ_{mn} and replacing $i\partial_t \to \omega_{mn} + \delta\omega$ on the lefthand side. The single term involving $\delta\phi$ at $O(\eta^{-1})$ is $\langle\phi_{mn}, (\kappa^2 - \omega_{mn}^2 D)\delta\phi\rangle$, and this vanishes upon integration by parts. On the right side, it is convenient to define the self-adjoint operator

$$H \equiv 2\left(-\frac{B_\varphi}{r}i\partial_z + \frac{\mathrm{a}B_zk_n^2}{\omega_{mn}}\right) = H^\dagger. \tag{4.32}$$

At last, then,

$$
\begin{aligned}
&-\langle\phi_{mn},\, D\phi_{mn}\rangle\,\delta\omega = \\
&-\frac{i}{2\eta}\left[(k_nB_z)^2\,\langle\phi_{mn},\phi_{mn}\rangle - \left\langle H\phi_{mn}, D_T^{-1}H\phi_{mn}\right\rangle - \frac{2\mathrm{b}B_zk_n^2}{\omega_{mn}}\left\langle\phi_{mn},\, r^{-2}D_T^{-1}H\phi_{mn}\right\rangle\right].
\end{aligned}
\tag{4.33}
$$

Now D and D_T^{-1} are negative-definite operators. Therefore, the only term that can make a positive contribution to the growth rate $\Im(\delta\omega)$ is the last term on the righthand side, and specifically the part of H involving $B_\varphi\partial_z$ since $\mathrm{ab} > 0$.

To evaluate $\delta\omega$ from (4.33), we need explicit expressions for D and D_T^{-1}. The first is easy enough: it follows from (4.14) that $D\phi_{mn} = -(k_n^2\kappa^2(r)/\omega_{mn}^2)\phi_{mn}$. For D_T^{-1}, we construct the eigenfunctions of D with the boundary conditions (4.30):

$$D\chi_{jn}(r,z) = -(q_j^2 + k_n^2)\chi_{jn}(r,z), \tag{4.34}$$

$$\chi_{jn}(r,z) \equiv R_{jn}(r)\sin k_nz\,, \qquad k_n = n\frac{\pi}{h}\,, \tag{4.35}$$

$$\text{where}\quad R_{jn} = \begin{cases} J_0(q_jr_1)Y_1(q_jr) - Y_0(q_jr_1)J_1(q_jr), & \text{if } q_j \neq 0; \\ r^{-1} & \text{if } q_0 = 0; \end{cases} \tag{4.36}$$

$$\text{and } q_j \text{ satisfies}\quad J_0(q_jr_1)Y_0(q_jr_2) - Y_0(q_jr_1)J_0(q_jr_2) \equiv 0\,. \tag{4.37}$$

When applied to χ_{jn}, $D_T^{-1} \to (q_j^2 + k_n^2)^{-1}$. An arbitrary function $f(r,z)$ can be expanded in these eigenfunctions, so that

$$D_T^{-1}f(r,z) = -\sum_n\sum_j (q_j^2 + k_n^2)^{-1}\frac{\langle\chi_{jn}, f\rangle}{\langle\chi_{jn},\chi_{jn}\rangle}\,\chi_{jn}(r,z)\,. \tag{4.38}$$

The important point is that D_T^{-1} turns a function proportional to $\sin k_nz$ into another such. Therefore, $\langle\phi_{mn}, D_T^{-1}\partial_z\phi_{mn}\rangle = 0$, and so the part of H involving $r^{-1}B_\varphi i\partial_z$

does not contribute to the expression (4.33) for the first-order eigenfrequency. This, however, was the only term that might have made for a positive growth rate. We conclude that *at $O(\eta^{-1})$, HMRI does not grow in finite cylinders with insulating endcaps.*

The same perturbative method could have been used for periodic vertical boundary conditions; ϕ_{mn} and χ_{jn} would have involved $\exp(ik_z z)$ instead of $\sin k_n z$. The term involving $r^{-1}B_\varphi i\partial_z$ in eq. (4.33) would then have contributed to the growth rate with the same sign as $-(k_z/\omega_{mn})\Omega B_\varphi B_z$. Evaluating this term, we conclude that in highly resistive periodic flows, (i) unstable modes propagate axially in the direction of the background Poynting flux—as found in WKB; and (ii) the instability occurs only if $\beta > \mathrm{a}k_z r/\omega_{mn}$ somewhere within the gap. Given the upper bound on ω^2_{mn} noted above, it follows that $\beta^2 > \min[4\mathrm{a}/\Omega(r)]$.

We have written MATLAB procedures to evaluate eq. (4.33). The results confirm our conclusions above. When periodic boundary conditions are used, the perturbative result matches the growth rate found from our radially global linear code to three digits in sufficiently resistive cases: *e.g.,* $\gamma = 1.89\times10^{-3}\Omega_1$ in the Princeton geometry with $Re_m = 0.1$, $S = 0.043$, $\Omega_2/\Omega_1 = 0.1325$, $\beta = 2$. But when insulating endcaps are imposed, the perturbative estimate of the growth rate is always negative.

4.2.2 Finite cylinders: modified WKB analysis

Here we analyze finite cylinders by approximations that do not require large resistivity: by a variant of WKB, and by direct axisymmetric numerical simulations, which will be described in the next subsection.

In the modified WKB approach, perturbations are again assumed to vary as $\exp(ik_r + st)$ with a common complex growth rate $s \equiv -i\omega$ and radial wavenumber $k_r = \pi/(r_2 - r_1)$, but the vertical dependence is treated differently. With the t and r dependence factored out, the linearized equations of motion reduce to homoge-

neous ordinary differential equations with coefficients independent of z. Elementary solutions of these equations exist with exponential dependence on z; however, since the vertical boundaries are not translationally invariant, the wavenumber k_z needs not be real, and growing modes can be linear combinations of the elementary exponential solutions with the same ω but different k_z. The vertical magnetic boundary conditions require the fields to match onto a vacuum solution that decays exponentially as $|z| \to \infty$ in the space $r_1 \leq r \leq r_2$ between the extended conducting cylinders:

$$z = 0: \quad \phi = b_\varphi = 0,\ \partial_z \psi = |k_r|\psi; \qquad z = h: \quad \phi = b_\varphi = 0,\ \partial_z \psi = -|k_r|\psi. \tag{4.39}$$

We search iteratively for such modes as follows. Given a trial value for s, the dispersion relation (4.16) has six roots—in general complex—for the vertical wavenumber, which can be regarded as algebraic functions of the growth rate: $\{k_{z,\alpha}(s)\}$, $\alpha \in \{1, \ldots, 6\}$. We seek a mode in the finite cylinder of the form

$$\boldsymbol{q}(t, r, z) \equiv [\phi, v_\varphi, \psi, b_\varphi]^T = \ e^{st + ik_r r} \sum_{\alpha=1}^{6} Y_\alpha \boldsymbol{q}_\alpha \exp(ik_{z,\alpha} z). \tag{4.40}$$

Each term in the sum above is the elementary solution corresponding to a particular root $k_{z,\alpha}(s)$, with $\boldsymbol{q}_\alpha$ a 4-component column vector; these elementary solutions are superposed with constant weights $\{Y_\alpha\}$. Substitution into the boundary conditions (4.39) yields a sixth-order homogeneous linear system for the $\{Y_\alpha\}$. Nontrivial solutions exist only if the determinant $\mathcal{D}(s)$ of this system vanishes. The equation $\mathcal{D}(s) = 0$ is transcendental and we cannot solve it analytically, but a numerical nonlinear zero-finding algorithm recovers the roots for s.

We have checked this procedure by replacing (4.39) with periodic boundary conditions and comparing the results with direct solutions of the dispersion relation (4.16). Also, we find reasonably good agreement with growth rates determined from ZEUS2D simulations of a narrow-gap configuration with insulating boundaries (see

below). However, for sufficiently large resistivity, no roots with positive $\Re(s)$ are found, in agreement with the perturbative results of Section 4.2.1.

4.2.3 Finite cylinder: nonlinear simulation

For the ZEUS2D simulations, we represent the poloidal magnetic field at $z \leq 0$ and $z \geq h$ by flux functions $\Psi_{\pm}(r,z)$ satisfying $b_r \boldsymbol{e}_r + b_z \boldsymbol{e}_z = r^{-1} \boldsymbol{e}_\varphi \times \boldsymbol{\nabla}\Psi$ and $\boldsymbol{\nabla} \times \boldsymbol{b} = 0$. The latter implies $r\partial_r(r^{-1}\partial_r\Psi) + \partial_z^2\Psi = 0$, which is solvable by separation of variables since we require $\Psi = 0$ on the vertically extended conducting cylinders. The elementary solutions are

$$\Psi_k(r,z) \propto r e^{-k|z-z_0|} \left[Y_1(kr_1) J_1(kr) - J_1(kr_1) Y_1(kr) \right] ,$$

for an infinite discrete set of nonnegative values of k determined by $\Psi_k(r_2,z) = 0$. At each endcap, we match the vertical field b_z protruding from the fluid with a superposition of vacuum solutions of this form, and thereby obtain a boundary condition relating b_z and b_r. Of course $b_\varphi = 0$ at these boundaries since the current along the axis is constant.

We have performed simulations with insulating endcaps for the parameters of Figure 4.2. We find a complex growth rate $s \approx 0.51 + 4.18i \ \mathrm{s}^{-1}$, as compared to $s \approx 0.37 + 3.68i \ \mathrm{s}^{-1}$ from the modified WKB approach (4.39)-(4.40) above. Considering the approximate nature of the latter approach, the agreement is satisfactory. We have also carried out ZEUS2D simulations with insulating endcaps in the wide-gap experimental geometry $[(r_1, r_2, h) = (7.1, 20.3, 28)\,\mathrm{cm}]$. Here we find a growth rate $\sim 0.27\,\mathrm{s}^{-1}$, as opposed to $\sim 1.06\,\mathrm{s}^{-1}$ with periodic boundaries. We conclude that insulating endcaps lower the growth rate, even in flows of moderate (Re_m, S).

A limitation of our direct simulations is that since we use explicit time stepping, we cannot explore very large resistivities [73]. The modified WKB approach does not

suffer from any restriction on η, but it is not trustworthy for wide gaps. The concordance between the two approaches where both are applicable—namely for narrow gaps and moderate (Re_m, S)—inclines us to trust results obtained from one of these approaches in regimes where the other is not applicable. In particular, the modified WKB method predicts that highly resistive flows are completely stable in finite cylinders, at least for narrow gaps. The perturbative analysis of Section 4.2.1 reaches the same conclusion for gaps of any width, but that analysis is valid at $O(\eta^{-1})$ only.

4.3 Discussion

We have analyzed the linear development of helical magnetorotational instability in a non-ideal magnetohydrodynamic Taylor-Couette flow, paying particular attention to the effects of the axial boundary conditions. A number of complementary approximations and numerical methods have been used.

For infinitely long or periodic cylinders, we confirm that there is an axisymmetric MHD instability that persists to smaller magnetic Reynolds number and Lundquist number in the presence of *both* axial and toroidal background magnetic field than the standard MRI that exists for axial field alone. The new mode is an overstability and propagates axially in the direction of the background Poynting flux $-r\Omega B_\varphi B_z/\mu_0$. In highly resistive flows, the new mode is a weakly destabilized hydrodynamic inertial oscillation. Growth depends also on the ratio of shear to rotation, *i.e.* Rossby number: for all aspect ratios r_2/r_1 that we have explored, and certainly for narrow gaps, the Keplerian Rossby number is stable.

We have also considered finite cylinders with insulating endcaps, which are closer to experimental reality but which do not permit traveling modes that propagate indefinitely along the axis. Astrophysical disks also have limited vertical thickness. These boundary conditions reduce the growth rate of the helical mode, and stabilize highly

resistive flows entirely, at least in the absence of viscosity and viscous boundary-layer effects.

Here some comments are in order regarding a recent paper that claims to have observed HMRI in the Potsdam PROMISE experiment [42]. It is reported that when the axial current lay in the range where HMRI was expected (based on an analysis of infinite cylinders), persistent fluctuations were measured by ultrasonic velocimetry that appeared to form axially travelling waves, consistent with expectations for HMRI.

These claims do not necessarily contradict our analysis. An exponential growth rate has not been reported, which would have been a clear signature of a discrete linear unstable mode. Rather than a global instability, we suspect that the observed fluctuations represent excitation by processes outside our inviscid analysis, followed by transient magnetic amplification as the disturbances propagate along the axis. This is what one might expect, given an appropriate source of excitation, when the local WKB dispersion relation predicts instability but the boundary conditions are not compatible with a global mode. Data given in [42] clearly show vibrations at the rotation frequencies of the cylinders themselves; these or other experimental imperfections might have excited the waves, although the peaks in the temporal power spectrum attibuted to the waves appear to be broader than those at the cylinder frequencies and are distinct from them. Further evidence that may bear on the excitation mechanism comes from another recent publication [98], which reports numerical axisymmetric simulations for parameters approximating the experiment but for both axially infinite (actually periodic) and finite cylinders. External vibrations, roughness, and magnetic interaction with the boundary need not exist in the simulations, but since no-slip conditions are applied at the endcaps, which rotate as in the experiment, viscous boundary layers should exist in the finite cylinders. In [98], a clear vertically travelling mode is seen in the infinite cylinders, but in the finite ones, the velocity fluctuations, though sustained, appear to be unsteady and to have

a fluctuating spatial pattern. At the Reynolds numbers where these fluctuations were reported, $Re \geq 900$, Ekman circulation in purely hydrodynamic simulations by [47] was also unsteady.

The above speculations aside, the fact remains that the inviscid analyses of the present chapter do not apply to situations where viscosity may be important, as they probably are in the PROMISE experiment. Viscous effects must be included to model such experiments reliably. On the other hand, viscous boundary layers lead to an exchange of angular momentum between the fluid and its container. Such exchanges are not expected to be important in astrophysical disks, so it may be appropriate to neglect viscosity when one is interested in astrophysically important modes.

Thus the relevance of HMRI to astrophysical disks is questionable, although it may be relevant to stellar interiors and jets, where the magnetic geometry and the Rossby number may be more favorable. Also, HMRI may have theoretical significance that goes beyond its direct applications. It is not understood why linearly and axisymmetrically stable rotating flows are often also nonlinearly and nonaxisymmetrically unstable, especially since subcritical transition does occur at some Rossby numbers [99]. The fact that even a very poorly coupled magnetic field can sometimes linearly destabilize such flows hints that it might also affect nonlinear transition.

Chapter 5

Germany PROMISE Experiment[1]

5.1 Experimental apparatus

The Potsdam Rossendorf Magnetic Instability Experiment (PROMISE) group have claimed to observe HMRI experimentally [42–44]. PROMISE facility is a cylindrical vessel made of copper (Fig. 5.1). The vessel is filled with the liquid alloy $Ga^{67}In^{20.5}Sn^{12.5}$. The dimensions are: $r_1 = 4.0$ cm, $r_2 = 8.0$ cm and $h = 40.0$ cm. The inner cylinder and outer cylinder are rotating differentially with $\Omega_1/s\pi = 3.6$ rpm and $\Omega_2/s\pi = 0.972$ rpm. The bottom endcap is co-rotating with the outer cylinder while the top endcap is stationary. More details of the facility could be found in Stefani et al. [42].

At magnetic and flow parameters where linear analysis predicts instability, persistent fluctuations were measured that appeared to form axially traveling waves, consistent with expectations for HMRI. Similar behavior has been seen in nonlinear numerical simulations that approximate the experimental conditions, including realistic viscous boundary conditions for the velocities, but simplified ones for the magnetic field: perfectly conducting cylinders, and pseudo-vacuum conditions at the endcaps for which $b_r = b_\varphi = \partial_z b_z = 0$ at both the end caps $z = 0,\ h$ (where b_r, b_φ and b_z

[1] inherited and modified from Liu et al. [46]

are the induced magnetic field components), when present [44, 98]. Both axially periodic and finite cylinders showed unsteady flow, the former case being more regular. However, the nonlinear simulations in [44, 98] used somewhat different values for the cylinder rotation rates and other parameters than those reported in [42].

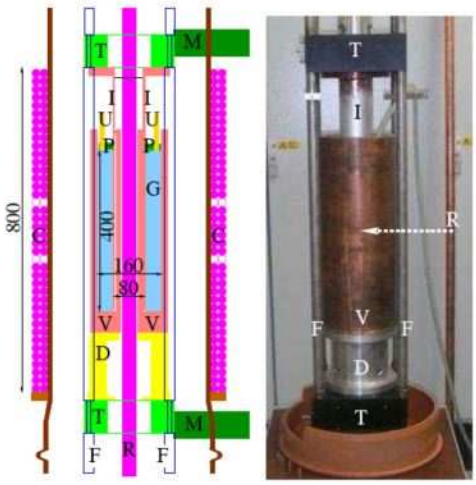

Figure 5.1: Figure courtesy of Stefani et al. "Sketch (left) and photograph (right) of the PROMISE facility. V - Copper vessel, I - Inner cylinder, G - GaInSn, U - Two ultrasonic transducers, P - Plexiglass lid, T - High precision turntables, M - Motors, F - Frame, C - Coil, R - Central rod. The dimensions are in mm."[2]

In Chap. 4, however, we have raised doubts about both the experimental realizability of HMRI and its astrophysical relevance[45]. Finite cylinders with insulating endcaps were shown to reduce the growth rate and to stabilize highly resistive flows entirely, at least inviscid ones.

Here we report nonlinear simulations with the ZEUS-MP 2.0 code [100], which is a time-explicit, compressible, astrophysical ideal MHD parallel 3D code, to which we have added viscosity, resistivity (with subcycling to reduce the cost of the induction equation), and vacuum boundary conditions, for axisymmetric flows in cylindrical coordinates (r, φ, z)[73]. The parameters of PROMISE as reported in or inferred from [42] are used: gallium density $\rho = 6.35\,\mathrm{g\,cm^{-3}}$, magnetic diffusivity $\eta = 2.43 \times$

[2]excerpt from the caption of Fig. 1 of Stefani et al. [42]

$10^3\,\mathrm{cm}^2\,\mathrm{s}^{-1}$, magnetic Prandtl number $Pr_\mathrm{m} \equiv \nu/\eta = 1.40 \times 10^{-6}$; Reynolds number $Re \equiv \Omega_1 r_1(r_2 - r_1)/\nu = 1775$; axial current $I_z = 6000\,\mathrm{A}$; toroidal-coil currents $I_\varphi = 0, 50, 75, 120\,\mathrm{A}$; and dimensions as in Fig. 5.2. The finite conductivity and thickness of the copper vessel are allowed for ($\eta_\mathrm{Cu} = 1.335 \times 10^2\,\mathrm{cm}^2\mathrm{s}^{-1}$), and this noticeably improves agreement with the measurements compared to previous linear calculations with radially perfectly conducting, axially periodic boundaries [42, 43]. Please note the difference of the direction of Ω, B_z and B_φ (components measured in a right handed coordinate system) between this chapter, where they are all assumed to be positive, and the experimental setup presented in [42], where they are all negative (private communication). The direction of the traveling wave depends on the sign of the Poynting flux defined as $-r\Omega B_\varphi B_z/\mu_0$ [45]. Thus the direction of the traveling wave reported here is opposite as reported in [42].

5.2 The necessities of Partial Conducting Boundary in PROMISE

At the low frequencies relevant to PROMISE ($f \sim 0.01\,\mathrm{Hz}$), the skin depth of Copper $\delta_w = \sqrt{\eta_\mathrm{Cu}/\pi f \mu_0} \approx 19\,\mathrm{cm}$, which is much larger than the thickness of the copper vessel surrounding the gallium in the PROMISE experiment, $d_w \approx 1.0\,\mathrm{cm}$, so that the magnetic field diffuses rather easily into the boundary. On the other hand, if one considers axial currents, the gallium and the copper wall act as resistors in parallel; taking into account their conductivities and radial thickness, one finds that their resistances are comparable [$R_I : R_{II} : R_{III} = 3 : 1 : 9$; see Fig. 5.2 for the subscripts]. Therefore, the currents carried by the copper walls could be important for the toroidal field, and a perfectly insulating boundary condition is also inappropriate.

We have adapted a linear axisymmetric code developed by [45, 53] to allow for a helical field. Vertical periodicity is assumed, to allow separation of variables, but

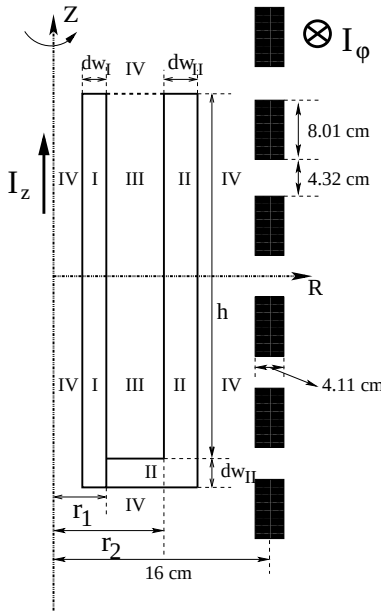

Figure 5.2: Computational domain for simulations of PROMISE experiment. Region (I): Inner copper cylinder, angular velocity Ω_1. (II): outer copper cylinder and bottom endcap, Ω_2. (III): liquid gallium; (IV): vacuum. Thick dashed line: insulating upper endcap, $\Omega = 0$. Dimensions: $r_1 = 4.0\,\mathrm{cm}$; $r_2 = 8.0\,\mathrm{cm}$; $h = 40.0\,\mathrm{cm}$; $d_{wI} = 1.0\,\mathrm{cm}$; $d_{wII} = 1.5\,\mathrm{cm}$; $\Omega_1/2\pi = 3.6\,\mathrm{rpm}$; $\Omega_2/2\pi = 0.972\,\mathrm{rpm}$. The exact configuration of the toroidal coils being unavailable to us, six coils (black rectangles) with dimensions as shown were used, with 67 turns in the two coils nearest the midplane and 72 in the rest. Currents I_φ were adjusted to reproduce the reported Hartmann numbers $Ha \equiv B_z^0 r_1/\sqrt{\rho\mu_0\eta\nu}$.

the full viscous and resistive radial equations are solved using finite differences, and a variety of radial boundary conditions can be imposed. For perfectly conducting boundaries and $I_\varphi = 75\,\mathrm{A}$, where [42] report persistent waves, our code indeed finds a complex growth rate: $s \approx 0.0057 + 0.057i\,\mathrm{s}^{-1}$. But for insulating boundaries, the same parameters yield stability.

This analysis points to the need for boundary conditions that accurately represent the influence of the copper vessels on the field. In the linear code just mentioned, we use the thin-wall approximation of [101], which in effect treats the cylinders as insulating for the poloidal field but conducting for the toroidal field. The errors of this approximation increase with the ratio of wall thickness to gap width, which is not very small (≈ 0.25) in our case. Growth is predicted, but at a smaller rate than for perfectly conducting walls, $s \approx 0.0052 + 0.056\,i\ \mathrm{s}^{-1}$. The insensitivity of the imaginary part to the magnetic boundaries supports the interpretation that these modes are hydrodynamic inertial oscillations weakly destabilized by the helical field [45].

In our nonlinear simulations, we include the copper walls (regions I and II) in the computational domain (Fig. 5.2), but not the external coils themselves, whose inductive effects are therefore neglected. Outside the walls (region IV) we match onto a vacuum field $\boldsymbol{B}_{\mathrm{ext}} = \boldsymbol{\nabla}\Psi$ vanishing at infinity. This is relatively straightforward in spherical geometry (used by many geodynamo experiments) because Laplace's equation separates. Our case is more difficult, because while Laplace's equation separates in cylindrical coordinates when the boundary is an infinite cylinder, it does not fully separate outside a *finite* cylinder. Therefore we use an integral formulation that does not assume separability. The idea, called von Hagenow's method [102], is to find a surface current on the boundary that is equivalent to the current density in the interior as the source for $\boldsymbol{B}_{\mathrm{ext}}$ *via* the free-space Green's function. The surface current is obtained by first solving the Grad-Shafranov equation [103, 104] in the interior with

conducting boundary conditions, a problem that *is* separable in our case and is solved efficiently by combining FFTs along z with tridiagonal matrix inversion along r.

5.3 Results and Discussion

We start with purely hydrodynamic (unmagnetized) simulations. For $\mu \equiv \Omega_2/\Omega_1 = 0.27$, what we see is simply an Ekman flow driven by the top and bottom end plates. Due to the stronger pumping at the upper, stationary lid, the two Ekman cells are of unequal size. They are separated vertically by a narrow, intense radial outflow, hereafter the "jet", lying at about 11 cm above the bottom endcap. As discussed in [47], the jet is unsteady at $Re \gtrsim 10^3$; it flaps or wanders rapidly in the poloidal plane. This has been verified by the PROMISE group (private communication). The amplitude of the flapping is $\pm 0.4\,\mathrm{mm\ s^{-1}}$.

Background states with purely axial or purely azimuthal magnetic fields are symmetric under reflection $z \to -z$, but a helical field breaks this symmetry[93]. As a result, growing modes in vertically infinite or periodic cylinders propagate axially in a unique direction: that of the background Poynting flux $-r\Omega B_\theta B_z/\mu_0$ [45]. Fig. 5.3 displays vertical velocities near the outer cylinder in simulations corresponding to the experimental runs of [42] for several values of the toroidal current, I_φ. A wave pattern very similar to that in the experimental data is seen. It is most obvious for $I_\varphi = 75\,\mathrm{A}$, just as in the experiment. Considering that we do not use exactly the same external coil configuration as PROMISE, the agreement is remarkably good (Table. 5.1).

Interestingly, the jet becomes nearly steady when $I_\varphi \geq 50\,\mathrm{A}$. It is known that Ekman circulation is significantly modified when the Elsasser number $\Lambda \equiv B^2/(\mu_0\rho\eta\Omega) \gtrsim 1$[79]. If we use $|\boldsymbol{B}(r_1)|$ for the field strength and Ω_2 for Ω in this expression, then $\Lambda = 4.8$ at $I_\varphi = 75\,\mathrm{A}$.

On the other hand, the magnetic field clearly promotes unsteadiness in the in-

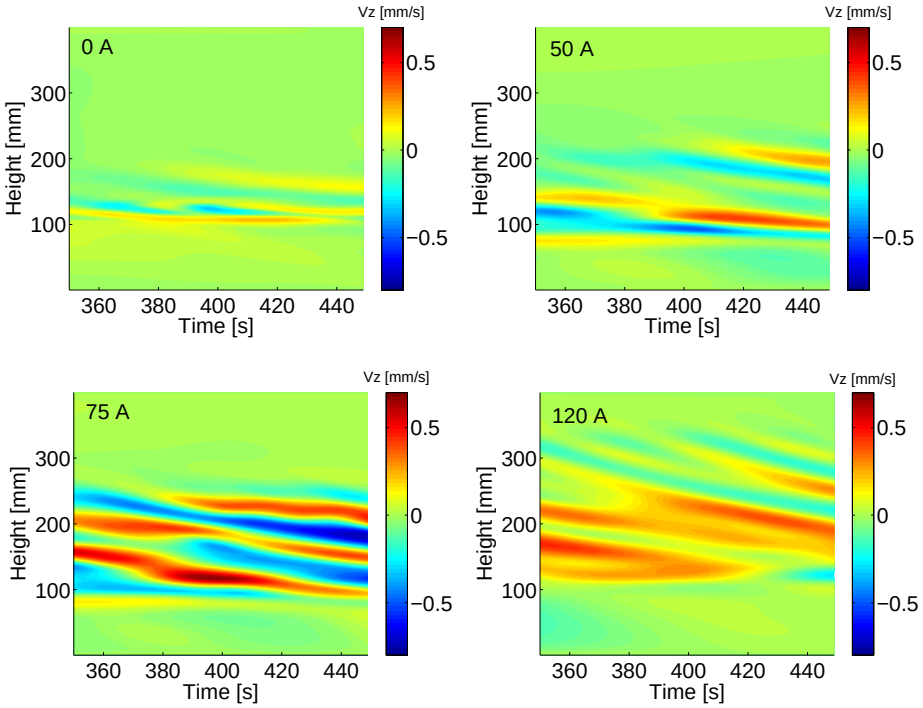

Figure 5.3: (color). Axial velocities [mm s^{-1}] versus time and depth sampled 1.5 cm from the outer cylinder, for the parameters of the PROMISE experiment with toroidal currents I_φ as marked. Note height increases upward from the bottom endcap. No-slip velocity boundary conditions are imposed at the rigidly rotating endcaps, but the steady part of the resulting Ekman circulation is suppressed in these plots by subtracting the time average at each height. The waves appear to be absorbed near the Ekman jet, at $z \approx 100$ mm.

	Calculation of [42, 43]	Experiment	Our Simulation
$f_{\rm wave}/f_1$	~ 0.14	~ 0.15	0.15
λ_{wave} [cm]	~ 12	6	6
v_p[mm s^{-1}]	1.1	0.8	0.7
A[mm s^{-1}]	unavailable	$\gtrsim 0.4$	$\gtrsim 0.6$

Table 5.1: Comparison of results for the frequency, wavelength, axial phase speed, and amplitude obtained from simulation and experiment for the case $I_\varphi = 75$ A. $f_1 \equiv \Omega_1/2\pi$ is rotation frequency of inner cylinder.

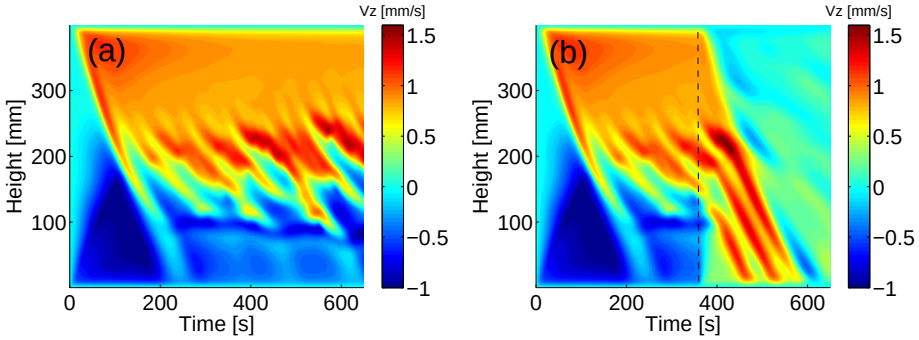

Figure 5.4: (color). Panel (a): An extended version of the case $I_\varphi = 75\,\mathrm{A}$ shown in Fig. 5.3 but without subtraction of the time average. The two Ekman cells are visible as the upflow (orange) at $z > 100\,\mathrm{mm}$ and downflow (blue) at $z < 100\,\mathrm{mm}$; these are the expected directions of flow near the outer cylinder. Panel (b): The same case again, except that after $t = 360\,\mathrm{s}$, the no-slip boundary condition at both endcaps is changed to an ideal Couette profile, *i.e.* $\Omega(r) = a + br^{-2}$ with a and b chosen to make Ω continuous at both cylinders; this eliminates Ekman circulation. Thereafter, the wave seems to be absorbed near the bottom ($z \approx 0\,\mathrm{mm}$) rather than the jet ($z \approx 100\,\mathrm{mm}$), which itself dies out after $t \approx 395\,\mathrm{s}$.

terior flow. The waves seen in Fig. 5.3 are probably related to HMRI, but we do not believe that they arise from a global instability of the experimental Couette flow. To demonstrate this, we have repeated the third ($I_\varphi = 75\,\mathrm{A}$) simulation shown in Fig. 5.3 with different velocity boundary conditions. First, when we replace the rigidly rotating endcaps with differentially rotating ones that follow the ideal angular velocity profile of an infinitely long Taylor-Couette flow, then instead of the persistent travelling waves seen in Fig. 5.3, we see slowly damping standing waves, which we interpret as inertial oscillations excited by a small numerical force imbalance in the inital conditions[45]. Second, we perform a simulation that begins with the experimental boundary conditions until the traveling waves are well established, and then switches abruptly to ideal-Couette endcaps. After the switch, the Ekman circulation stops and the traveling waves disappear after one axial propagation time, as if they had been emitted by the Ekman layer at the upper endcap or by the layers on the upper part of the cylinders (Fig. 5.4). After the switch in boundary conditions but

before the waves fully disappear, their vertical phase speed increases from $-0.7\,\mathrm{cm\ s^{-1}}$ to $-1.1\,\mathrm{cm\ s^{-1}}$; the latter is the speed predicted by linear analysis for axially periodic flow [43] (Fig. 5.4). Both numerical tests support the interpretation that the wave pattern observed in the simulation and in the experiment is not a global HMRI mode but rather a transient disturbance that is somehow excited by the Ekman circulation and then transiently amplified as it propagates along the background axial Poynting flux, but is then absorbed once it reaches the jet or the bottom end cap.

Chapter 6

Magnetic Ekman Layer[1]

From the discussion of the previous chapters, understanding the role of the boundary layer is essential to this research. In order to explain how the boundary layer is affected by the magnetic field, we present this separate chapter. This chapter concentrates only on magnetic Ekman circulation (the rotation speed profile is chosen appropriately so that the system is MRI stable). The liquid metal is confined in a limited region ($r_1 \leqslant r \leqslant r_2,\ z_{min} = 0 \leqslant z \leqslant z_{max} = h$). However the cylinders are presumed infinitely long and perfectly conducting (of course this is not realistic); these magnetic boundary conditions prevent the field lines from attaching to the cylinders and allow the magnetic field to be matched onto vacuum solutions easily that decay as $|z| \to \infty$ in the regions on the top of and underneath the fluid (Fig. 6.1). It is known that Ekman circulation is significantly modified when the Elsasser number [79] exceeds unity:

$$\Lambda = B_\infty^2/(8\pi\rho\eta\Omega) \gtrsim 1\,,$$

where B_∞ is the axial magnetic field far away from the end cap and $\Omega = \Omega_2$ rather than $\sqrt{\Omega_1\Omega_2}$ used in Chap. 3. is the characteristic rotation frequency. The Elsasser number Λ is a dimensionless parameter that measures the relative importance of

[1] inherited and modified from Liu et al. [76]

the magnetic field. The implementation of the radial conducting, vertical insulating boundary condition is introduced in Appendix.A.2.3.

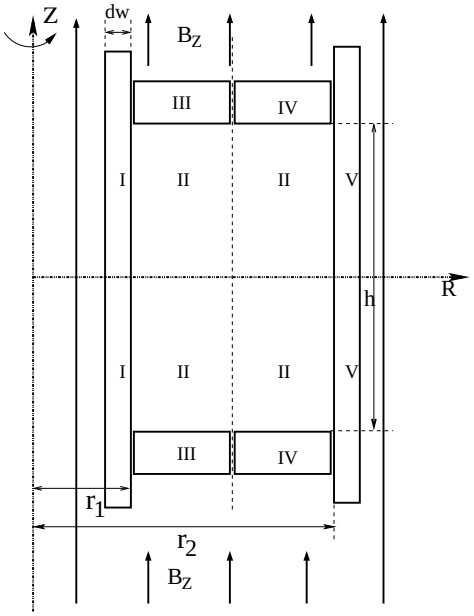

Figure 6.1: Computational domain for studies of magnetic Ekman layer. Region (I): Perfect conducting inner cylinder, angular velocity Ω_1, infinitely long. (II): Liquid metal, $\rho \approx 6.0$ cm^2 s^{-1}, $\eta \approx 2.0 \times 10^3$ cm^2 s^{-1}. (III): Perfectly insulating inner ring, Ω_3, extends to infinity; (IV): Perfectly insulating outer ring, Ω_4, extend to infinity; (V): Perfectly conducting outer cylinder, Ω_2, infinitely long. Thin dash line: the middle plane. B_z is the initial background vertical uniform magnetic field. Dimensions are: $r_1 = 7.1\,\mathrm{cm}$, $r_2 = 20.3\,\mathrm{cm}$, $h = 27.9\,\mathrm{cm}$, $d_w \to \infty$ except stated explicitly. Ω_1, Ω_2, Ω_3, Ω_4 and B_z are adjusted accordingly.

6.1 Standard Magnetic Ekman Layer with infinitesimal differential rotation[2]

This section is inherited and modified from Jeremy Goodman's notes (unpublished).

The imposition of no-slip conditions at finite endcaps introduces important complications to the basic state, including Ekman circulation and Stewartson layers [51]. There has been research done in the past considering the MHD Ekman layers (or

[2]inherited and modified from Jeremy Goodman's unpublished notes

Ekman-Hartmann layers as sometimes refered to in the literature) [77, 78, 80, 81]. However there has been little work aside from Pariev [90] on differential rotation, and even less on Stewartson layers [51] with magnetic field.

For a first attack on this problem, the hydromagnetic Ekman boundary is set up to study how the Ekman layer thickness and mass flux are affected by magnetic fields. The problem treated consists of a viscous (kinetic viscosity ν), incompressible, conducting (magnetic diffusivity η) fluid in the presence of an infinite, flat, insulating boundary which rotates at speed Ω. Outside the boundary, the fluid rotates uniformly with speed $\Omega' = \Omega(1 + Ro)$, where Ro is the Rossby number which measures the differential rotation. A uniform magnetic field aligned with the rotation axis is imposed. The boundary is horizontal ($z = 0$ plane), *i.e.* perpendicular to $\Omega = \Omega \mathbf{e_z}$. In the analysis of Gilman and Benton [77], an expansion in powers of Ro, together with von Kármán similarity [105, 106], leads to an exact solution which is accurate to first order in Ro. In the limit of $Ro \ll 1$, or infinitesimal differential rotation, increasing Λ results in a continuous transition between pure Ekman flow and a rotating analog of Hartmann flow.

Here one different approach similar to the one used in §4.2.2 is presented. This method is essentially a modified steady state WKB analysis rather than an expansion of von Kármán similarity variables used in Gilman and Benton [77]. With the t and r dependence factored out, the linearized equations of motion reduce to homogeneous ordinary differential equations with coefficients independent of z. Elementary solutions of these equations exist with exponential dependence on z; however, since the vertical boundaries are not translationally invariant, the wavenumber k needs not be real, and the final solution can be linear combinations of the elementary modes and one particular mode, which satisfies the boundary conditions at $z = \infty$ but not at $z = 0$. The vertical magnetic boundary conditions require the fields to match onto a vacuum solution at the end plate.

As in the standard Ekman problem, there is a constant pressure gradient parallel to the boundary, which we may take in the x direction: $\bigtriangledown p = \rho g \mathbf{e_x}$, where the acceleration g is a constant. To balance this at large z where viscosity is not important, there is a geostrophic flow:

$$\mathbf{v} \rightarrow \frac{g}{2\Omega}\mathbf{e_y} \quad \text{as} \quad z \rightarrow \infty \tag{6.1}$$

$$\mathbf{v} \rightarrow 0 \quad \text{as} \quad z \rightarrow 0 \tag{6.2}$$

so that $2\Omega \times \mathbf{v} = - \bigtriangledown p/\rho$ at large z. Henceforth we write V_∞ for $g/2\Omega$. The second line is the no-slip condition at the boundary, which is assumed to rotate at Ω. The velocity field $\mathbf{v}$ is assumed to be a function of z only, and $\mathbf{v_z} = 0$ at all z.

The new element in the problem is the magnetic field. We suppose that

$$\mathbf{B} \rightarrow B_\infty \mathbf{e_z} \quad z \rightarrow \infty \tag{6.3}$$

where B_∞ is a constant, so that the field is perpendicular to the boundary at large distances from it. Various boundary conditions can be applied at $z = 0$. For insulating boundaries, the condition $J_\perp = 0$ is automatically satisfied since we assume that $\mathbf{B}$ is a function of z only. B_z is independent of z as a consequence of $\bigtriangledown \cdot \mathbf{B} = dB_z/dz = 0$.

The Euler and induction equations reduce to (primes mean d/dz)

$$\begin{aligned} -2\Omega v_y + \frac{B_\infty}{4\pi\rho} B_x^{'} + \nu v_x^{''} &= -g \\ 2\Omega v_x + \frac{B_\infty}{4\pi\rho} B_y^{'} + \nu v_y^{''} &= 0 \\ B_\infty v_x^{'} + \eta B_x^{"} &= 0 \\ B_\infty v_y^{'} + \eta B_y^{"} &= 0 \end{aligned} \tag{6.4}$$

This is an in-homogeneous linear system with constant coefficient. The general solu-

tion is

$$\begin{pmatrix} v_x \\ v_y \\ B_x \\ B_y \end{pmatrix} = \begin{pmatrix} 0 \\ V_\infty \\ 0 \\ 0 \end{pmatrix} + \sum_{n=1}^{8} C_n \begin{pmatrix} v_{x,n} \\ v_{y,n} \\ B_{x,n} \\ B_{y,n} \end{pmatrix} \exp[k_n z] \tag{6.5}$$

The first column vector on the right-hand side is the particular solution, which satisfies the boundary conditions at $z = \infty$ but not at $z = 0$. The column vectors $(v_{x,n}, \ldots, B_{y,n})^T$ are constant, and the terms of the summation are solutions of the homogenous version of Eqn 6.4 for $g = 0$. Their amplitudes $\{C_n\}$ must be chosen to satisfy the boundary condition. The 8 values of the wavenumber $\{k_n\}$ are the roots

$$det \begin{vmatrix} \nu k^2 & -2\Omega & kB_\infty/4\pi\rho & 0 \\ 2\Omega & \nu k^2 & 0 & kB_\infty/4\pi\rho \\ kB_\infty & 0 & \eta k^2 & 0 \\ 0 & kB_\infty & 0 & \eta k^2 \end{vmatrix} = 0 \tag{6.6}$$

In term of the Alfvén speed $V_A = B_\infty/\sqrt{4\pi\rho}$, this becomes

$$k^4[(\eta\nu)^2 k^4 + 2\eta\nu V_A^2 k^2 + (V_A^4 + 4\Omega^2\eta^2)] = 0\,, \tag{6.7}$$

Only the nonzero roots of this equation are of interest since they determine the boundary-layer thickness. The quadruple root $k = 0$ can thus be neglected. The rest of the roots are

$$k^2 = \frac{V_A^2}{\eta\nu} \pm \frac{2\Omega i}{\nu}\,. \tag{6.8}$$

The boundary-layer thickness can be singled out as $\delta = |\mathbb{R}(k)|^{-1}$, which is the same for all four roots. ["$\mathbb{R}(\ldots)$" means "real part of $(\ldots)$".] The solutions that behave

acceptably as $z \to \infty$ are the ones with $\mathbb{R}(\dots) < 0$. Thus

$$\delta = \delta_E \frac{1}{\sqrt{\sqrt{\Lambda^2+1}+\Lambda}} \approx \delta_E \times \begin{cases} 1-\Lambda/2 & \text{if } \Lambda \ll 1\,; \\ 1/\sqrt{2\Lambda} & \text{if } \Lambda \gg 1\,. \end{cases} \tag{6.9}$$

Here $\delta_E = \sqrt{\nu/\Omega}$ is the purely hydrodynamical Ekman-layer thickness. Noticeably, Λ has nothing to do with ν. Hence even if the boundary layer were turbulent, having the laminar viscosity ν enhanced by an effective turbulent viscosity ν_T and the thickness increased by $O[(\nu_T/\nu)^{1/2}]$, the magnetic field would be at least as consequential as in the laminar case. The field would result in a more stable layer and push the onset of turbulence to larger Reynolds numbers. In the limit of $\Lambda \to \infty$, $\delta \to \sqrt{\nu\eta}/V_A$: this is the Hartmann-layer thickness which does not depend upon Ω. For gallium,

$$\Lambda \approx 3.2(\frac{B}{\text{Tesla}})^2(\frac{1000\ \text{rpm}}{\Omega})\,. \tag{6.10}$$

Adopting the parameters used in the experiment, $\Omega = \Omega_2 = 533$ rpm, $B = 5000$ Gauss, immediately leads to $\Lambda \sim 1.5$. Hence the magnetic Ekman layer should be relevant in our case.

The two "acceptable" nonzero roots of Eqn 6.8, satisfying the boundary conditions ($v_x = v_y = 0$ at $z = 0$, and $v_x \to 0$ and $v_y \to V_\infty$ at $z \to \infty$) for k are $k_\pm = -(k_R \pm i k_I)$, where $k_R = \delta^{-1}$ as given by Eqn 6.9, so that

$$v_x = -V_\infty e^{-k_R z} \sin k_I z\,, \tag{6.11}$$

$$v_y = V_\infty (1 - e^{-k_R z} \cos k_I z)\,, \tag{6.12}$$

where V_∞ is the velocity far away from the end plate and k_I is related to k_R by

$$\frac{k_I}{k_R} = \sqrt{1+\Lambda^2} - \Lambda\,.$$

The mass flux is:

$$\rho \int_0^\infty v_x dz = -\frac{\rho V_\infty \delta}{2\sqrt{\Lambda^2+1}} \approx -\frac{\rho V_\infty \delta_E}{2} \times \begin{cases} 1-\Lambda/2 & \text{if } \Lambda \ll 1; \\ 1/\Lambda\sqrt{2} & \text{if } \Lambda \gg 1. \end{cases} \tag{6.13}$$

Compared to Eqn 6.9, the mass flux diminishes more rapidly than the boundary-layer thickness as $\Lambda \to \infty$.

The above theoretical results can serve to benchmark our code (Fig. 6.2). The thickness of the layer could be refined by fitting the simulated data using Eq. 6.11 (choosing the simulated data at $r = (r_1 + r_2)/2$ to minimize the radial boundary effects). The reciprocal of the fitted k_R is the Ekman layer width. The simulated result fits the theoretical line nicely.

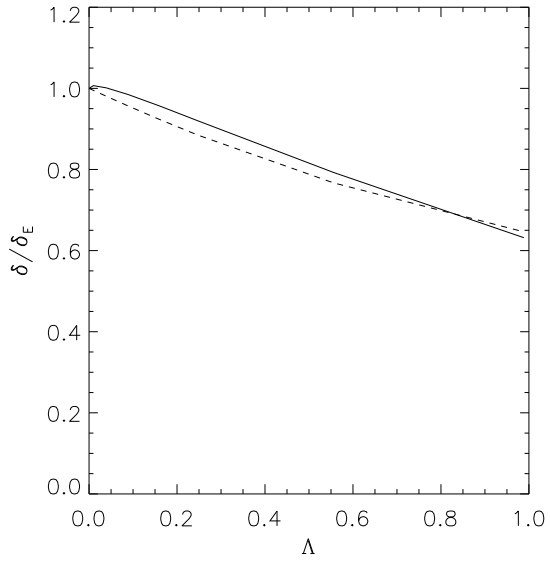

Figure 6.2: The thickness of the Ekman layer δ versus Elssaser Number Λ for $Re = 1600$, $Re_m = 5$, $Ro = 0.01$. $\Omega_1/2\pi = 1000$ rpm, $\Omega_2/2\pi = 1000$ rpm, $\Omega_3/2\pi = 1010$ rpm, $\Omega_4/2\pi = 1010$ rpm. $r_1 = 15$ cm, $r_2 = 35$ cm and $h = 20$ cm. The data is measured at $r = (r_1 + r_2)/2 = 20$ cm. The dashed line is the theoretical result. The solid line is the one obtained from modified ZEUS-2D simulations. Here in order to minimize the effects of curvilinear streamlines, one larger radius is chosen. And also in order to minimize the effect of the top end cap, one large height $h \gg 10\ \delta_E$ is chosen.

6.2 Magnetic Ekman Layer with finite differential rotation

Aside from the standard magnetic Ekman circulation ($Ro \ll 1$), there is large differential rotation in the experiment. As a further step, we develop the problem with the end plates corotating with the outer cylinder ($\Omega_1/2\pi = 500$ rpm, $\Omega_2 = \Omega_3 = \Omega_4 = 66.625$ rpm). In the next section, the problem is delved further by splitting the end plates into two rings as in the experiment. The new boundary condition (vertically insulating finite height) introduced in §A.2.3 and benchmarked by the above analysis is employed to explore these two problems.

The geometry models the Princeton MRI experiment ($r_1 = 7.1$ cm, $r_2 = 20.3$ cm, $h = 27.9$ cm). There has been some analytical work done already to further the previous studies [77] accounting for the differential rotation of the liquid in the vessel [90] with the end plates co-rotating as a solid body with the angular velocity Ω_2 while the rotational profile far from the end plate is assumed to be ideal Couette. This section is based on the framework laid out in Pariev [90].

The Reynolds number for the flow in the Ekman layer is [90]:

$$Re_\delta \approx \frac{r_2\Omega_2\delta}{\nu} \approx Re^{1/2} \sim 3 \times 10^3\,, \tag{6.14}$$

for 100% run in the Princeton MRI experiment. At this Reynolds number the boundary layer is turbulent. However in the simulations, the Reynolds number is taken to be 6400, thus $Re_\delta = 80$, so that in the simulations the boundary layer is laminar. Our consideration below is grounded on the equations of laminar flows, which is also the case in the analysis of [90].

The magnetic Reynolds number in the boundary layer based on the thickness of

the Ekman layer is defined as:

$$Rm_\delta = \frac{\delta U_0}{\eta} \approx \frac{Re_m}{\sqrt{Re}}\,, \tag{6.15}$$

where U_0 is the characteristic speed. For $Re = 6400$ and $Re_m = 2.5$ realized in the simulations, $Rm_\delta \approx 3.125 \times 10^{-2}$, As soon as $Rm_\delta \ll 1$ and $|(\Omega - \Omega_2)/\Omega_2| \ll 1$, the following linear equation is derived [90]:

$$\frac{\partial^2 \zeta}{\partial z_*^2} - 2(\Lambda + i)\zeta + \frac{d\omega}{dr_*}\frac{i}{2} r_*(\bar{\zeta} - \zeta) = 0\,, \tag{6.16}$$

where the complex variable ζ is defined as:

$$\zeta = u_\varphi - i u_r\,,$$

and $\bar{\zeta}$ is the complex conjugate of ζ, u_φ, u_r are the relative flow speed compared to the background pure azimuthal rotating ideal Couette state, ω is normalized relative rotation speed expressed as:

$$\omega = (\Omega - \Omega_2)/\Omega_2\,,$$

and r_*, z_* are normalized by r_2, δ_E respectively. For any given r_*, Eq. 6.16 is a forth order linear ordinary differential equation with constant coefficients. This equation has the solutions which have the form of $u_r \propto e^{\alpha z_*}$, $u_\varphi \propto e^{\alpha z_*}$. It gives: [90]

$$\alpha^4 - 4\Lambda\alpha^2 + (4 + 4\Lambda^2 + 2r_*\frac{d\omega}{dr_*}) = 0\,.$$

For small ω, the quantity $1 + (1/2)r_* d\omega/dr_* = 1/(2\Omega_2 r)d(r^2\Omega)/dr = a/\Omega_2 > 0$, which is the ratio of vorticity to rotation speed. Thus, we have [90]

$$\alpha_1 = \alpha_1^{'} + i\alpha_1^{''}, \quad \alpha_2 = -\alpha_1, \quad \alpha_3 = \bar{\alpha}_1, \quad \alpha_4 = -\bar{\alpha}_1\,,$$

where $\alpha_1^{'}$ and $\alpha_1^{''}$ are real, and $\alpha_1^{'} > \alpha_1^{''} > 0$. They are expressed as: [90]:

$$\alpha_1^{'} = \sqrt{\sqrt{\Lambda^2 + 1 + \frac{1}{2} r_* \frac{d\omega}{dr_*}} + \Lambda}\,, \tag{6.17}$$

$$\alpha_1^{''} = \sqrt{\sqrt{\Lambda^2 + 1 + \frac{1}{2} r_* \frac{d\omega}{dr_*}} - \Lambda}\,. \tag{6.18}$$

The boundary condition $\zeta \to 0$ for $z_* \to \infty$ requires that only the terms $\propto e^{\alpha_2 z_*}$ and $\propto e^{\alpha_4 z_*}$ would remain. The following solutions are obtained, satisfying boundary conditions at $z_* = 0$ [90]

$$u_r = -\frac{r_* \omega}{\sqrt{1 + \frac{1}{2} r_* \frac{d\omega}{dr_*}}} e^{-\alpha_1^{'} z_*} \sin(\alpha_1^{''} z_*)\,, \tag{6.19}$$

$$u_\varphi = -r_* \omega e^{-\alpha_1^{'} z_*} \cos(\alpha_1^{''} z_*)\,. \tag{6.20}$$

The solution is oscillating and exponentially decaying to zero for $z \to \infty$, which is the classical picture of the Ekman layer. Hence the Ekman layer thickness δ is given by:

$$\delta = \delta_E (\alpha_1^{'})^{-1} = \delta_E \frac{1}{\sqrt{\sqrt{\Lambda^2 + 1 + \frac{1}{2} r_* \frac{d\omega}{dr_*}} + \Lambda}}\,. \tag{6.21}$$

The Eq. 6.19, Eq. 6.20 and Eq. 6.21 reproduce Eq. 6.11, Eq. 6.12 and Eq. 6.9 if there is no differential rotation ($d\omega/dr_* \to 0$).

It is worth emphasizing that the above derivation is fully based on a small ω, or $(\Omega - \Omega_2)/\Omega_2 \ll 1$. Such a rotation profile develops a very thin Ekman layer and the required resolution is beyond the capability of the current ZEUS code. Given a finite ω ($\Omega_1 = 500$ rpm $> \Omega_2 = 66.625$ rpm), putting aside the nonlinear effects due to this finite ω which is ignored in Eq. 6.16 and following the analyses of Pariev [90], we have the following conclusions.

The quantity of $1+(1/2)r_*d\omega/dr_*$ could be expressed as with a finite ω:

$$1+\frac{1}{2}r_*\frac{d\omega}{dr_*}=\frac{1}{(2\Omega r)}\frac{d(r^2\Omega)}{dr}\,,$$

in which the ideal Couette state is $\Omega=a+b/r^2$, $a=(\Omega_2 r_2^2-\Omega_1 r_1^2)/(r_2^2-r_1^2)$ and $b=r_1^2r_2^2(\Omega_1-\Omega_2)/(r_2^2-r_1^2)$. Thus the value of the quantity is dependent on radius r, rather than a positive constant (a/Ω_2) as in the limit of $\omega\ll 1$. At some radius r there could exist some reason, such as, the deviation of the background flow profile to the ideal Couette state, which causes the quantity to change sign. The negative quality $1+(1/2)r_*d\omega/dr_*$ results in three sub-cases, which could be classified by the critical Elsasser number $\Lambda_{\rm crit}=\sqrt{-1-(1/2)r_*d\omega/dr_*}$ [90]:

(1) If $\Lambda>\Lambda_{\rm crit}$,

$$u_r = \frac{r_*\omega}{2\Lambda_{\rm crit}}(e^{-\alpha_3 z_*}-e^{-\alpha_1 z_*})\,, \tag{6.22}$$

$$u_\varphi = -\frac{r_*\omega}{2}(e^{-\alpha_1 z_*}+e^{-\alpha_3 z_*})\,, \tag{6.23}$$

where

$$\alpha_1 = \sqrt{2\Lambda-2\Lambda_{\rm crit}}\,, \tag{6.24}$$

$$\alpha_3 = \sqrt{2\Lambda+2\Lambda_{\rm crit}}\,. \tag{6.25}$$

The solution is purely exponentially decaying away from the end plate.

(2) If $\Lambda=\Lambda_{\rm crit}$, the width of Ekman layer increases to infinity.

(3) If $\Lambda<\Lambda_{\rm crit}$ (relaxing the boundary condition to have finite velocity components far from the end plate, rather than zero),

$$u_r = \frac{r_*\omega}{2\Lambda_{\rm crit}}(e^{-\alpha_3 z_*}-\cos(\alpha_1^{''}z_*))+C_2\sin(\alpha_1^{''}z_*)\,, \tag{6.26}$$

$$u_\varphi = -\frac{r_*\omega}{2}(\cos(\alpha_1^{''}z_*)+e^{-\alpha_3 z_*})+C_2\Lambda_{\rm crit}\sin(\alpha_1^{''}z_*)\,, \tag{6.27}$$

where

$$\alpha_1^{''} = \sqrt{2\Lambda_{\rm crit} - 2\Lambda}\,,$$

and the constant C_2 remains undetermined. The solution is purely oscillating, which should be subject to the *Kelvin-Helmholtz instability* and should quickly evolve into a turbulent state. However whichever case it is, *the strong magnetic field causes the Ekman layer to become thinner.* More details are given by Pariev [90]. Therefore our problem with finite ω is much more complicated than the analyses presented before in this section, even though the nonlinear effects are not considered.

Nonlinear simulations using ZEUS with vertically insulating, radially conducting boundary conditions have been performed for the computational domain shown as Fig. 6.1. Dimensions are $r_1 = 7.1$ cm, $r_2 = 20.3$ cm and $h = 27.9$ cm with $Re = 6400$ and $Re_m = 2.5$. The rotational profile is: $\Omega_1/2\pi = 500$ rpm, $\Omega_2 = \Omega_3 = \Omega_4 = 66.625$ rpm. The simulation approaches the condition of the above linear theory except that: (1) the radial boundary condition is conducting rather than insulating(a magnetic Ekman layer with fully insulating boundaries on all sides is the next step for this problem and will be included in a forthcoming paper); (2) the flow profile far away from the end plate is modified, though not significantly; thus it is not Couette any more; (3) $|(\Omega - \Omega_2)/\Omega_2| \ll 1$ is not satisfied except near the outer cylinder, where the flow is governed by the conducting boundary.

Therefore in the analysis of the nonlinear simulation results, $r_d = (r_1 + r_2)/2$ is chosen to minimize the influence of both conducting cylinders, but keeping in mind that $|(\Omega(r_d) - \Omega_2)/\Omega_2| = 1.08 \sim 1$, some nonlinear effects neglected in Eq. 6.16 could be important and the quantity $1 + (1/2)r_* d\omega/dr_*$, which is nonlocal, could be either positive or negative, thus complicating the problem.

The magnetic Ekman layer thickness is discerned by fitting the simulated v_r according to Eq. 6.19 on the assumption of the classical Ekman layer picture, where $\alpha_1^{'}$ is supposed to the reciprocal of the thickness. From Fig. 6.3, we confirm that the

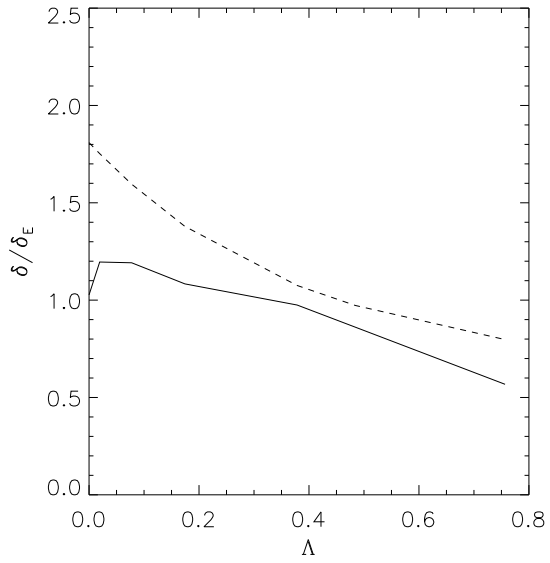

Figure 6.3: The thickness of the Ekman layer δ versus Elssaser Number Λ for $Re = 6400$, $Re_m = 2.5$. $\Omega_1/2\pi = 500$ rpm, $\Omega_2/2\pi = \Omega_3/2\pi = \Omega_4/2\pi = 66.625$ rpm. $r_1 = 7.1$ cm, $r_2 = 20.3$ cm and $h = 27.9$ cm. The data are measured at $r = (r_1 + r_2)/2 = 13.7$ cm. The dashed line is from the linear analysis. The solid line is obtained from modified ZEUS-2D simulations. These parameters make the MRI stable.

axial magnetic field does reduce the Ekman layer thickness. Though the simulated curve does not match the theoretical result very well, it is reasonably good given the approximations mentioned above.

For $Re = 6400$, the final state is not steady. Typical (instantaneous) flow and field patterns are shown in Fig. 6.4. The poloidal flux and stream functions are defined so that

$$\boldsymbol{V}_P \equiv V_r \boldsymbol{e}_r + V_z \boldsymbol{e}_z = r^{-1} \boldsymbol{e}_\varphi \times \boldsymbol{\nabla}\, \Phi, \qquad \boldsymbol{B}_P \equiv B_r \boldsymbol{e}_r + B_z \boldsymbol{e}_z = r^{-1} \boldsymbol{e}_\varphi \times \boldsymbol{\nabla}\, \Psi, \quad (6.28)$$

which imply $\boldsymbol{\nabla} \cdot \boldsymbol{V}_P = 0$ and $\boldsymbol{\nabla} \cdot \boldsymbol{B}_P = 0$.

The most noticeable feature of the final state of the magnetic Ekman circulation is the presence of an area of solid body rotation near the outer cylinder (Fig. 6.4 (d)). And the larger the Elsasser number is, the larger this area is; the strong axial magnetic field squeezes the dynamically active area to the inner cylinder (Fig. 6.5). When $\Lambda = 1.5$, almost half of the liquid metal is rotating with the outer cylinder.

6.3 Magnetic Ekman layer with two split rings

The existence of Ekman circulation alters the system profile dramatically, and it is unfavorable for the proposed MRI experiments [47]. To minimize this circulation in the MRI experiment, endcaps consisting of two differentially rotating rings are proposed [47]. Though pure hydrodynamic simulations predict that an adequate approximation to the ideal Couette profile can be obtained with a few rings, the modification by the axial magnetic field has to be studied. The introduction of rings complicates the problem by resulting in a so-called "Stewartson" layer [51], which lies between the rings.

We have brought the computation closer to the experimental conditions by adding two independent rotating rings (Fig. 6.1), where $\Omega_1/2\pi = 500$ rpm, $\Omega_2/2\pi = 66.625$ rpm,

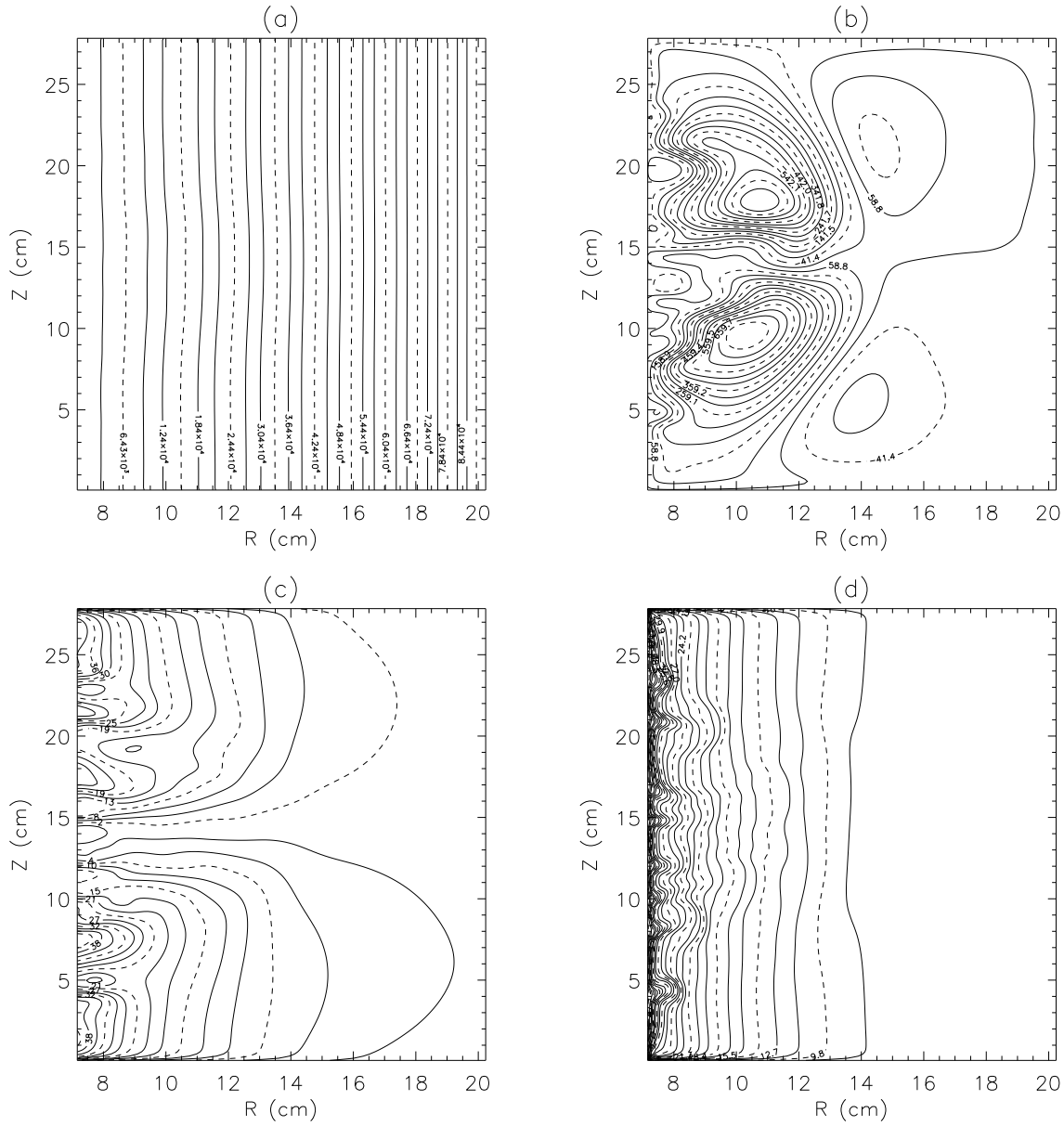

Figure 6.4: Contour plots of final-state velocities and fields. $Re = 6400$, $Re_m = 2.5$ with $B_z = 1500$ Gauss or $\Lambda = 1.09$. $\Omega_1/2\pi = 500$ rpm, $\Omega_2/2\pi = \Omega_3/2\pi = \Omega_4/2\pi = 66.625$ rpm. $r_1 = 7.1$ cm, $r_2 = 20.3$ cm and $h = 27.9$ cm. (a) Poloidal flux function Ψ (Gauss cm^2) (b) Poloidal stream function Φ (cm^{2}s^{-1}) (c) toroidal field B_φ (Gauss) (d) angular velocity $\Omega \equiv r^{-1}V_\varphi$ (rad s^{-1}).

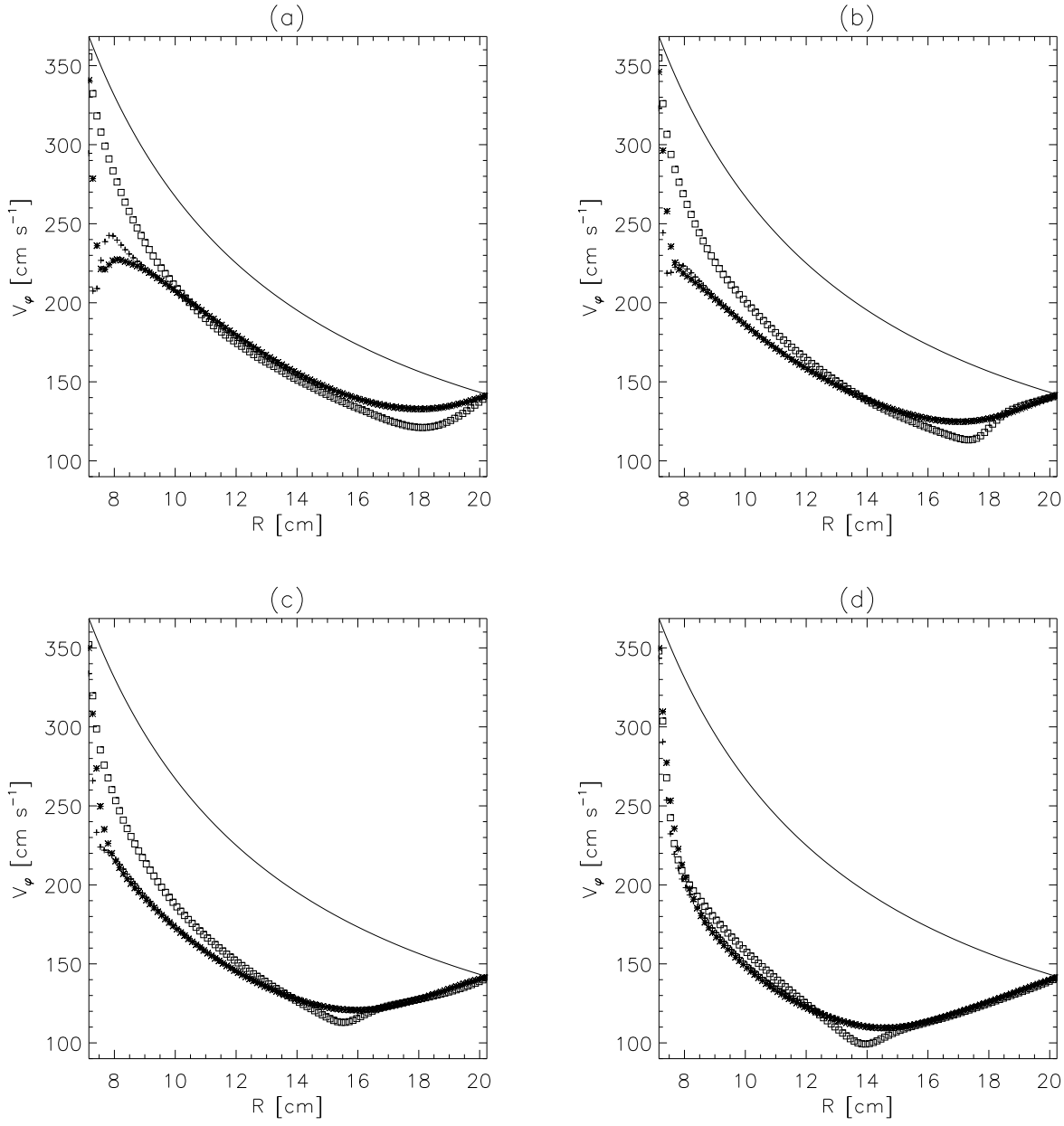

Figure 6.5: Azimuthal velocity v_φ versus radius r at different height with $Re_m = 2.5$, $Re = 6400$. $\Omega_1/2\pi = 500$ rpm, $\Omega_2/2\pi = \Omega_3/2\pi = \Omega_4/2\pi = 66.625$ rpm. $r_1 = 7.1$ cm, $r_2 = 20.3$ cm and $h = 27.9$ cm. solid line, ideal Couette state; + , 1.33 cm; $*$,2.79 cm; □ ,13.95 cm. (a) $\Lambda = 0$; (b) $\Lambda = 0.38$; (c) $\Lambda = 0.76$; (d) $\Lambda = 1.5$.

$\Omega_3/2\pi = 227.5$ rpm, $\Omega_4/2\pi = 81.25$ rpm. The dimensions are still $r_1 = 7.1\,\mathrm{cm}$, $r_2 = 20.3\,\mathrm{cm}$, $h = 27.9\,\mathrm{cm}$.

For $Re = 6400$, the final state is not steady. Typical (instantaneous) flow and field patterns are shown in Fig. 6.6.

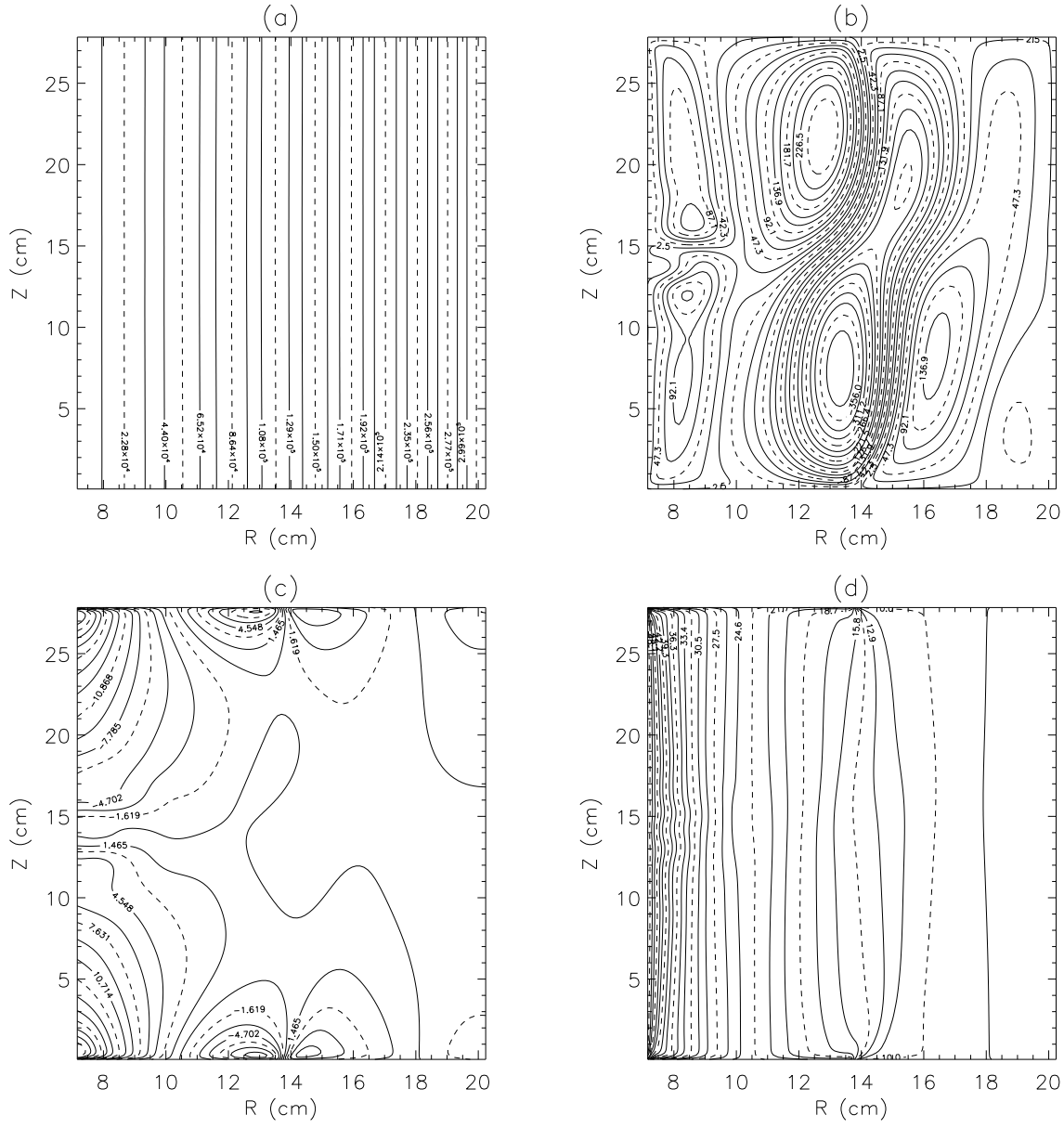

Figure 6.6: Like Fig. 6.4, but with two differential rotating rings and $\Lambda = 1.5$. the Stewartson layer is located between the rings and breaks the two big Ekman cells into eight cells.

The following observations can be made from Fig. 6.6. With rings the Stewartson

layer is more apparent than Ekman circulation, which has been minimized efficiently by the use of independently rotating rings. However the split end caps break the two big Ekman cells of the pure hydro Ekman circulation into eight cells, four at the top half and the other four at the bottom half (Fig. 6.6 (b)) (also see the analysis of §3.2.2 of Chap. 3). The middle four cells are the straightforward consequences of the Stewartson layer. The axial magnetic field aligns the flow along the field lines and elongates the cells axially. The stronger the axial magnetic field is, the more the azimuthal speed profile deviates from ideal Couette state (Fig. 6.7). This suggests that the Stewartson layer penetrates deeper into the fluid. Strong magnetic field leads to a more steady final state, even though the Reynolds number is high. This implication indicates that the strong magnetic field causes the Stewartson layer to be steady (Fig. 3.11 of Chap. 3). The higher Reynolds number is, the more the azimuthal speed profile deviates from ideal Couette state. This suggests the Stewartson layer extends further into the fluid (Fig. 6.8).

6.4 Discussion

It is worth emphasizing here that the rotation profile used in the simulations of this section ($\Omega_1/2\pi = 500$ rpm, $\Omega_2/2\pi = 66.625$ rpm, $\Omega_3/2\pi = 227.5$ rpm, $\Omega_4/2\pi = 81.25$ rpm) is different from the one used in the purely hydrodynamical experiment with $\Omega_4 < \Omega_2$ [26, 49]. And the purely hydrodynamical experimental results show that the azimuthal velocity profile is quite smooth; no obvious Stewartson layer is observed [49], which conflicts with our simulated results here and the reports of Hollerbach and Fournier [50]. This difference could be explained by an unstable Stewartson layer.

As mentioned before in Sec. 6.2, the sign of the quantity $1 + (1/2)r_* d\omega/dr_* = 1/(2\Omega r)d(r^2\Omega)/dr$ determines the structure of the flow significantly. The local value of the quantity is highly possible to be negative since in our experiment a small

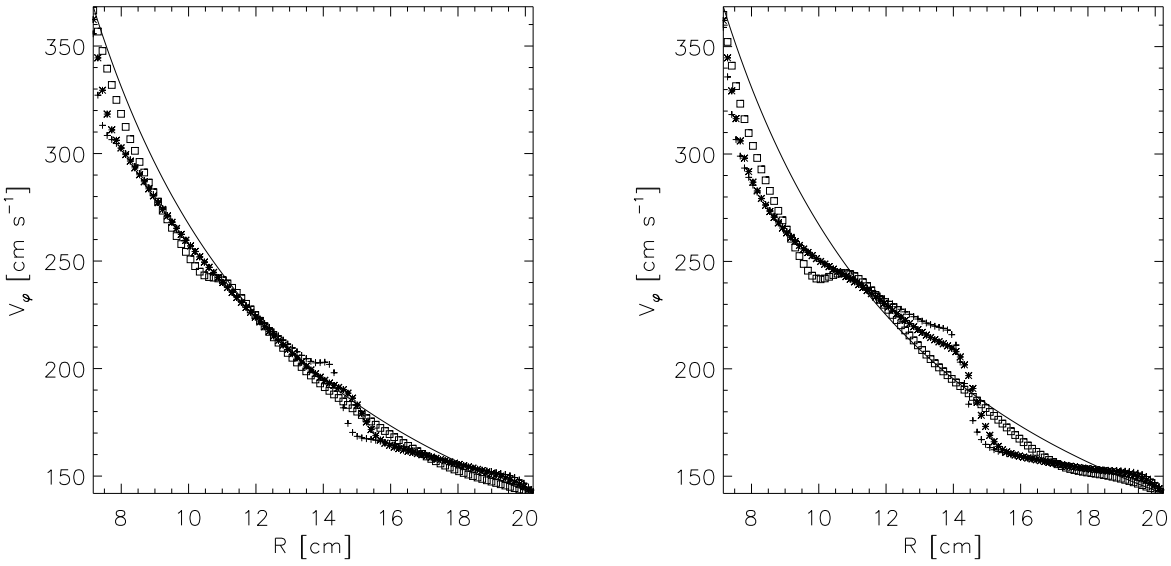

Figure 6.7: Azimuthal velocity v_φ cm s^{-1} versus radius r at different height with $Re_m = 2.5$, $Re = 6400$, for differential rotation end cap rings with $\Omega_1/2\pi = 500$ rpm, $\Omega_2/2\pi = 66.625$ rpm, $\Omega_3/2\pi = 227.5$ rpm, $\Omega_4/2\pi = 81.25$ rpm: solid line, ideal Couette state; + , 1.33 cm; $*$,2.79 cm; □ ,13.95 cm. Left panel: $\Lambda = 0.38$; right panel: $\Lambda = 1.5$.

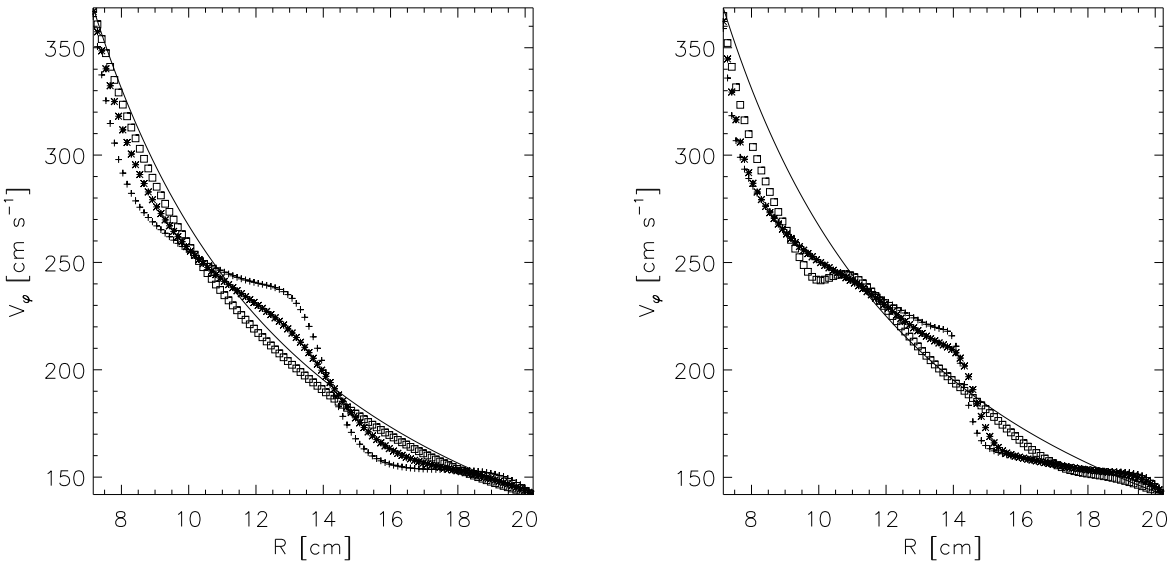

Figure 6.8: Azimuthal velocity v_φ cm s^{-1} versus radius r at different height with $Re_m = 2.5$, $\Lambda = 1.5$, for differential rotation end cap rings with $\Omega_1/2\pi = 500$ rpm, $\Omega_2/2\pi = 66.625$ rpm, $\Omega_3/2\pi = 227.5$ rpm, $\Omega_4/2\pi = 81.25$ rpm: solid line, ideal Couette state; + , 1.33 cm; $*$,2.79 cm; □ ,13.95 cm. Left panel: $Re = 400$; right panel: $Re = 6400$.

positive a is chosen to have the system close to a marginally Rayleigh's centrifugal stable case and the background flow could be locally modified. The negative quantity complicates the problem greatly, especially when $\Lambda < \Lambda_{\rm crit}$, which is usually satisfied in the experiment. In this case the purely oscillating solution results in a vertical shear (not necessarily confined in the boundary layer), thus is subject to the *Kelvin-Helmholtz instability* and quickly evolves into a turbulent state (see details in Sec.6.2). Moreover, at the joint of the rings, the outer ring rotates more slowly than the inner one ($\Omega_4 < \Omega_3$), hence $\partial(r^2\Omega^2)/\partial r < 0$ across the joint. This radial shear could also result in the *Kelvin-Helmholtz instability* given a sufficiently high Reynolds number. At the same time *Rayleigh's centrifugal instability* could also happen since $\partial(r^2\Omega)/\partial r < 0$ across the joint. Additionally we use a low Reynolds number in the simulations so that the boundary layer is laminar ($Re_\delta = \sqrt{Re} = 80$), however, under experimental parameters the boundary layer should be turbulent ($Re_\delta = \sqrt{Re} \gtrsim 3 \times 10^3$). Therefore an unstable Stewartson layer is highly possible. The layer may be smoothed by localized circulation and/or turbulence from these instabilities.

Unfortunately our 2-D simulation (the same as in Hollerbach and Fournier [50]) with a relatively low Reynolds number ($Re = 6400$) could not resolve these issues (possibly the *Rayleigh's centrifugal instability* could be resolved if the Reynolds number is high enough since it is basically a axisymmetric mode) since the *Kelvin-Helmholtz* is basically a toroidal nonaxisymmetric mode, and could possibly be the sources of the difference between the simulated result and the experimental observation.

It is well known that surface tension at the interface between two fluids will hinder the *Kelvin-Helmholtz instability*. Similarly in a homogeneous but magnetized fluid such as ours, magnetic field tension supplies a stabilizing force, and the stability requirement for the inviscid *Kelvin-Helmholtz instability* is:

$$\triangle v \leqslant 2V_A$$

where $\triangle v$ is the velocity jump and V_A is the Alfvén speed. The same is true for the *Rayleigh's centrifugal instability* [34]. This could explain why the Stewartson layer extends deeper into the bulk with a stronger magnetic field (Fig. 6.7), by suppressing the instabilities that would otherwise tend to smooth the velocity gradient. For example in Fig. 6.7, the $\triangle v = (\Omega_3 - \Omega_4) * r_d = 210$ cm s^{-1} while the V_A is 102 cm s^{-1} for the left panel with $\Lambda = 0.38$ and is 204 cm s^{-1} for the right panel with $\Lambda = 1.5$ respectively. Therefore the left panel is a *Kelvin-Helmholtz* unstable case while the right panel is a *Kelvin-Helmholtz* stable case.

Chapter 7

Conclusions and Future Work[1]

7.1 Conclusions

In Chap. 2 and Chap. 3 of this thesis we present non-ideal magnetohydrodynamic simulations of the Princeton MRI experiment. In vertically infinite or periodic cylinders, MRI saturates in a resistive current-sheet with a significant reduction of the mean shear, and with poloidal circulation scaling as the square root of resistivity. Angular momentum transport scales as the reciprocal square root of viscosity but only weakly depends on resistivity. For finite cylinders with insulating end caps, a method for implementing the fully insulating boundary condition is introduced. MRI grows with a clear linear phase from small amplitudes at rates in good agreement with linear analysis. In the final state one inflowing "jet" opposite to the usual Ekman "jet" is found near the inner cylinder. The MRI enhances the angular momentum transport at saturation. Under proper conditions our experimental facility is a good platform to show that MRI could be suppressed by a strong magnetic field.

The recently reported helical MRI [40, 41] has also been investigated in Chap. 4 and Chap. 5. In vertically infinite or periodic cylinders, resistive HMRI is a weakly destabilized hydrodynamic inertial oscillation propagating axially along the back-

[1] contribution also from Jeremy Goodman and Hantao Ji

ground Poynting flux. Growth rates are small, however, and require large axial currents. Furthermore, finite cylinders with insulating endcaps were shown to reduce the growth rate and to stabilize highly resistive, inviscid flows entirely, and the new mode is stable in Keplerian flow profiles regardless of end conditions. We also numerically investigate a traveling wave pattern observed in experimental magnetized Taylor-Couette flow at low magnetic Reynolds number. By accurately modeling viscous and magnetic boundaries in all directions, we reproduce the experimentally measured wave patterns and their amplitudes. Contrary to previous claims [42–44], the waves are shown to be transiently amplified disturbances launched by viscous boundary layers rather than globally unstable magnetorotational modes.

The roles of boundary layers, which are critical to this project, such as the magnetic Ekman layer and Stewartson layer [51], are also studied in Chap. 6. The magnetic field is found to inhibit the Ekman suction. While we quantitatively confirmed the conclusions of Gilman and Benton [77], Loper [78], Gilman [79], Benton and Chow [80], Gupta [81], the finite differential rotation cannot be neglected and modifies the linear Ekman layer. The width of the Ekman layer is reduced with increased magnetic field normal to the end plate. A uniformly-rotating region forms near the outer cylinder. The Stewartson layer penetrates deeper into the fluid with larger Reynolds number and stronger magnetic field. Furthermore a strong magnetic field leads to a steady Stewartson layer, at least in axisymmetric configuration.

This thesis work shows that in a laboratory Taylor-Couette experiment the boundary layer usually plays an important role, even dominating the bulk fluid through Ekman circulation and/or magnetic-boundary interactions. Most astrophysical studies model only large-scale phenomena insensitive to the boundary conditions. However one can not usually understand the physics of a laboratory Taylor-Couette experiment correctly without elaborating boundary effects since the laboratory flows are usually subsonic, and sometimes also sub-Alfvénic, the bulk fluid communicates easily with

the boundary. On the other hand, in order to apply knowledge we learnt from lab experiments to astrophysics, we need to filter out the effects due to boundaries. This process in general is not a trivial one when attempted through theory and experiment. Simulations can be a powerful tool to pin down exactly what parts are due to boundary and what parts are due to genuine physics we intend to study. A good example is Helical MRI.

This thesis work also illustrates the value of interplay between experiment, simulation and analytic insight. In all above studies, comparison of models and measurements will be used to validate our theoretical tools, which we will apply to nonlinear saturation of resistive MRI in astrophysical systems. Theoretical modeling has already played a major role in the design of the MRI experiment, and the physics of these modes and boundary layers may be of interest for fluid dynamics and geophysics as well as astrophysics.

7.2 Future Work

7.2.1 Performance Improvement of the current code

The most powerful computers today are clusters where hundreds to thousands of processors are inter-connected. In the spirit of ZEUS, the current code, the modified ZEUS-MP 2.0, is implemented as a SPMD (Single Program, Multiple Data) parallel code using the Message Passing Interface (MPI) to carry out interprocessor communication. The finite-difference scheme requires data at multiple mesh points to evaluate the gradient, divergence and Laplacian operators. When those operations are performed along processor boundaries, we need to exchange data between neighboring processors. Too much communication overhead would reduce the parallel efficiency and thus is not favored. This issue is commonly known as *scalability*, which is typically assessed by measuring the reduction in CPU time for a given quantity of work as

this is distributed among an increasing number of processors. Generally, scalability involves a number of factors, though parallelism is a leading one. The comprehensive discussion of scalability is beyond the scope of this thesis work; however better scalability is crucial for computations with strong magnetic field, high Reynolds number and/or three dimensions since higher resolution and thus a larger number of processors, is necessary. We have used several methods including *Non-blocking message passing*, which allows interprocessors data exchange to proceed simultaneously with computational operations, and *message packing* techniques, which assembles lots of short messages into one long messages to decrease the number of messages, to improve the scalability of the current code. However it is not yet maximumly optimized. Some performance improvement could be achieved with more effort.

Efficient scalable solver of the Grad-Shafranov Equation

The solution of the Grad-Shafranov equation [103, 104] with *conducting* boundary condition as part of von-Hagenow method [102] is a key ingredient of the implementation of fully insulating and partially conducting boundary conditions (see also §A.2.3). In the current code this equation is solved by combining FFTs along z with tridiagonal matrix inversion along r. Though the method used now is efficient, it is not well scalable. In a larger system, the *Multigrid* method is said to be scale better since ideally the required number of iterations for convergence of a *Multigrid* solver can be virtually independent of the problem size. Therefore the performance of the current code could be improved by employing such a method. Good parallel solvers satisfying the scalability requirement could be found in the *PETSc* package [107–109]. PETSc is a suite of data structures and routines for the scalable (parallel) solution of scientific applications modeled by partial differential equations. It provides many parallel solvers including *Multigrid* and *Incomplete Cholesky Conjugate Gradient (ICC-CG)* methods. As most parallel packages the data array used by *PETSc* is

divided along the first dimension of the data cube, which is sometimes called "slab" decomposition. Generally, the data is preprocessed from a general "block" domain decomposition to a "slab" decomposition before calling the *PETSc* routines. After this operation is completed, the "slab" decomposition of the data is transformed back to "block" decomposition in the postprocessing stage. Also note that *PETSc* is written in C language, and its FORTRAN version is also available but with less and worse functionality. *PETSc* routines must be called cautiously when they are called from a FORTRAN main program due to the different memory structures between C and FORTRAN. The codes based on *PETSc* using *Multigrid* or *ICC-CG* methods are ready; however significant effort is expected to debug them.

Implicit method to evolve the resistive term of the Induction Equation

ZEUS is an explicit MHD code. The diffusion term of the Induction equation is handled by an ohmic term added to the electromotive force in accord with the Constrained Transport algorithm [110], which preserves $\nabla \cdot \vec{B} = 0$ (see §A.1.1). However in an explicit diffusion scheme, the Courant-Friedrichs-Lewy (CFL) stability condition limits the time step to tiny in the very resistive limit (see §A.1.2). The current code uses the *SubCycling* technique to reduce the computation cost. Though this technique is efficient for the simulations discussed in this thesis work, it is not efficient enough for more demanding simulations like the ones with higher resolution. Implicit methods are essentially the best choice for the diffusive computations.

The Induction equation is:

$$\frac{\partial \vec{B}}{\partial t} = \underbrace{\nabla \times (\vec{V} \times \vec{B})}_{1} + \underbrace{\eta \triangle \vec{B}}_{2} .$$

We can handle the first term just following the explicit method used in ZEUS: MOC-

CT scheme [111]. The second term:

$$\frac{\partial \vec{B}}{\partial t} = \eta \triangle \vec{B}\,, \tag{7.1}$$

is a simple diffusion equation. As stated before, the best way to handle this diffusion equation is an *implicit* method.

The difficulties associated with this equation are: (1) this equation being a vector equation; (2) the divergence-free nature of the magnetic field, which could be manipulated by using vector potential.

Assuming axisymmetry, the toroidal component of Eq. 7.1 is:

$$\frac{\partial B_\varphi}{\partial t} = \eta (\triangle \vec{B})_\varphi\,. \tag{7.2}$$

As for the poloidal magnetic field components, we introduce the vector potential $\vec{A}$, satisfying:

$$\vec{B} = \nabla \times \vec{A}\,.$$

Since it is axisymmetric, $\vec{A}$ only has one independent component A_φ. Performing the curl operation on the Eq. 7.1, we get:

$$\frac{\partial A_\varphi}{\partial t} = \eta (\triangle \vec{A})_\varphi\,, \tag{7.3}$$

and

$$\begin{aligned} B_z &= \frac{1}{r}\frac{\partial}{\partial r}(r A_\varphi)\,; \\ B_r &= -\frac{1}{r}\frac{\partial}{\partial z}(r A_\varphi)\,. \end{aligned} \tag{7.4}$$

We can see that $rA_\varphi = \Psi$, which is the flux function discussed in previous chapters. Given the flux function at the inner cylinder, we can get the flux function Ψ from the

known magnetic field as:

$$\Psi(z,r) = \int_{r_1}^{r} r^{'} B_z(z,r^{'}) dr^{'} + \Psi(z,r_1)\,. \tag{7.5}$$

The computation of this flux function at the inner cylinder is not trivial for the fully insulating and partially conducting boundary conditions, which could be efficiently handled by the von-Hagenow method (see §A.2.3).

The mathematical nature of Eq. 7.2 and Eq. 7.3 is essentially the same. We can regard them as:

$$\frac{\partial u}{\partial t} = \eta(\triangle u)\,, \tag{7.6}$$

which could be efficiently solved by an implicit solver based on *ILU-ICC* or *Multigrid* methods. Again these solvers could be found in *PETSc* package. Some tentative coding is completed. However some significant effort is needed to debug the codes.

7.2.2 Work to be done

The Princeton MRI experiment has already had some initial magnetized results. Comparison between the simulated results and experimental results would be very exciting. The simulation results are very important to explain and model the experimental data since the experimental diagnostics are limited or inaccessible to some regions of the experimental facilities.

Though the MRI is primarily an axisymmetric mode, the toroidal mode could be generated due to the large Reynolds number ($Re \sim 10^7$, 100% run), for example in the purely hydrodynamical experiment with the outer cylinder stationary [112]. The *Kelvin-Helmholtz* instability discussed in §6.4 is essentially a toroidal mode, which can only be resolved in 3-D calculations. Furthermore possible turbulence cannot be investigated appropriately without 3-D computations. The unexpected $m = 1$ mode of the helical MRI observed in the Germany PROMISE experiment [42] also requires

3-D simulations. These concerns show that 3-D simulations of both Princeton MRI and Germany PROMISE experiments are possibly important. Though ZEUS-MP 2.0 is a 3-D code, the 3-D fully insulating boundary condition needs substantial work. Boundary Element Method (BEM) [113, 114] or the methods proposed in Alouges [115], Xu et al. [116] could be possible solutions.

It is not understood why linearly and axisymmetrically stable rotating flows with low Reynolds number are often also nonlinearly and nonaxisymmetrically unstable when Reynolds number is large enough, especially since subcritical transition does occur at some Rossby numbers [99]. The fact that even a very poorly coupled magnetic field can sometimes linearly destabilize such flows hints that it might also affect the nonlinear transition. Thus nonlinear hydrodynamical instability simulation with magnetic field is also a meaningful follow-up of this thesis work, though simulations with a large Reynolds number are required to step into this subcritical transition regime.

The flexibility of controlling the flow profile at the endcaps makes our experimental facilities a good platform to study the magnetized Ekman layers. However at our best knowledge no theoretical analysis of the magnetized Ekman layer with two split rings has been done yet. Thus the interplay between experiment, theory and simulation of the magnetized Ekman layer could be an interesting topic for further understanding the role of the boundary layers in the experiments.

Appendix A

ZEUS code and Modifications[1]

To confirm astrophysical MHD codes in a laboratory configuration is one of the declared aims of the Princeton experiment. Probably the most widely utilized astrophysical MHD code is ZEUS [96, 111], which has several versions. The simulations in this thesis were performed using modified ZEUS-2D and modified ZEUS-MP 2.0 [100], which were devised for compressible, ideal-MHD flow with various simple boundary conditions: periodic, outflow, inflow, reflecting.

ZEUS, like most astrophysical MHD codes, would not be the first choice to simulate an incompressible Taylor-Couette flow. However, after resistivity, viscosity, and appropriate boundary conditions are incorporated into ZEUS, it is found to be a sturdy and flexible testbed for the subsonic flows of interest. It reproduces the growth rates predicted for incompressible flow (Chap. 2), and agrees with hydrodynamic laboratory data [49]; MHD data are still on the way.

All fluids in nature are compressible. Incompressibility is a property obtained in the limit of $M \to 0$, where $M \equiv V_{\rm flow}/V_{\rm sound}$ is the Mach number. From hydrodynamics, the density changes of an ideal gas with fixed total volume generally are proportional to M^2 when $M < 1$. A compressible isothermal equation of state, with a sound speed chosen to enforce the maximum $M \leq 1/4$, was employed in ZEUS and

[1] contribution also from Jeremy Goodman, James Stone, Steve Jardin and Hantao Ji

quantitative agreement with incompressible codes at the few-percent level (§B.3) was achieved.

Both ZEUS-2D and ZEUS-MP 2.0 provide the options of Cartesian (x, y), spherical (R, θ), or cylindrical (z, r) coordinates. Cylindrical coordinates are used in this thesis. ZEUS-2D retains the azimuthal components of velocity (v_φ) and magnetic field (B_φ) although all quantities are assumed independent of the azimuth angle φ. We used ZEUS-MP 2.0, a 3-D code, with the assumption of axisymmetry.

A.1 New Physics: Explicit Viscosity and Magnetic Resistivity

A.1.1 General Hydromagnetic Equations

For completeness, we start from the general hydromagnetic equations based on the single-fluid model governing compressible hydromagnetic flow without bulk viscosity.

Navier-Stokes equation:

$$\rho\frac{D\vec{V}}{Dt} = \frac{1}{c}\vec{j}\times\vec{B} + \sigma\vec{E} - \nabla P + \rho\nu\bigtriangledown^2\vec{V} + \frac{1}{3}\rho\nu\bigtriangledown(\bigtriangledown\cdot\vec{V}) \tag{A.1}$$

Ohm's law:

$$\frac{1}{\eta}(\vec{E} + \frac{\vec{V}}{c}\times\vec{B}) = \vec{j} \tag{A.2}$$

Conservation of mass:

$$\frac{\partial\rho}{\partial t} + \nabla\cdot\rho\vec{V} = 0 \tag{A.3}$$

Ampére's law:

$$\nabla\times\vec{B} = \frac{4\pi}{c}\vec{j} + \frac{1}{c}\frac{\partial\vec{E}}{\partial t} \tag{A.4}$$

Divergence-free condition:

$$\nabla \cdot \vec{B} = 0 \tag{A.5}$$

Faraday's law:

$$\nabla \times \vec{E} = -\frac{1}{c}\frac{\partial \vec{B}}{\partial t} \tag{A.6}$$

Gauss's law:

$$\nabla \cdot \vec{E} = 4\pi\sigma \tag{A.7}$$

Here $\vec{V}$ is the fluid velocity, $\vec{B}$ is the magnetic field, $\vec{E}$ is the electric field, $D/Dt \equiv \partial/\partial t + \vec{V}\cdot\nabla$ and ρ, ν, η are density, kinetic viscosity and magnetic diffusivity respectively. Also σ and j are the free charge density and free current density, c is the speed of light, and P is the effective pressure including the gravity.

In the MHD regime, the equations are simplified to

$$\rho\frac{D\vec{V}}{Dt} = -\bigtriangledown P + \frac{1}{4\pi}(\bigtriangledown \times \vec{B}) \times \vec{B} + \rho\nu \bigtriangledown^2 \vec{V} + \frac{1}{3}\rho\nu \bigtriangledown (\bigtriangledown \cdot \vec{V}), \tag{A.8}$$

$$\frac{D\rho}{Dt} + \rho \bigtriangledown \cdot \vec{V} = 0, \tag{A.9}$$

$$\frac{\partial \vec{B}}{\partial t} = \nabla \times (\vec{V} \times \vec{B}) + \eta \bigtriangledown^2 \vec{B}, \tag{A.10}$$

$$\bigtriangledown \cdot \vec{B} = 0. \tag{A.11}$$

The system of equations is closed with a equation of state $P = \rho V_s^2$, where V_s is the constant sound speed.

Viscosity and resistivity have been incorporated into the code. In order to conserve angular momentum exactly, we cast the azimuthal component of the Navier-Stokes

equation in conservative form:

$$\frac{\partial L}{\partial t} \; + \; \frac{\partial}{\partial z}\left(V_z L + F_z + J_z\right) \; + \; \frac{1}{r}\frac{\partial}{\partial r}\left(r V_r L + r F_r + J_r\right) = 0\,. \tag{A.12}$$

In Eq. A.12, $L = rV_\varphi$, and F_r and F_z are the viscous angular-momentum fluxes per unit mass

$$F_z = -\nu\frac{\partial L}{\partial z}\,, \qquad F_r = -\nu r^2 \frac{\partial}{\partial r}\left(\frac{L}{r^2}\right)\,, \tag{A.13}$$

while J_r and J_z are the magnetic angular-momentum fluxes per unit mass

$$J_z = -\frac{rB_\theta B_z}{\mu_0 \rho}\,, \qquad J_r = -\frac{rB_\theta B_r}{\mu_0 \rho}\,. \tag{A.14}$$

In the spirit of ZEUS, the viscous part of Eq. (A.12) is implemented as part of the "source" substep. The original ZEUS implements the magnetic part of Eq. (A.12) in the Lorenz force step in a nonconservative form. It has been changed to a conservative form for this thesis work.

In accord with the Constrained Transport algorithm [110], which preserves $\nabla\cdot\vec{B} = 0$, resistivity is implemented by an ohmic term added to the electromotive force, which becomes

$$\mathcal{E} = \vec{V}\times\vec{B} - \eta\nabla\times\vec{B}\,. \tag{A.15}$$

A.1.2 Stability: New Time Step[2]

This section is following the framework of Stone and Norman [96, 111].

An explicit code like ZEUS must restrict the time step to satisfy the Courant-Friedrichs-Lewy (CFL) stability condition. Physically, this condition can be understood as limiting the distance that information can travel in one time step via waves or fluid motion to be smaller than one grid spacing. We must choose the largest time

[2]following the idea of Stone and Norman [96, 111]

step possible such that the CFL condition is satisfied in every cell. Thus, in ZEUS we choose the explicit time step using [96, 111]

$$\Delta t = C_0/[\max(\delta t_1^{-2} + \delta t_2^{-2} + \delta t_3^{-2} + \delta t_4^{-2} + \delta t_5^{-2})]^{1/2}\,.$$

The maximum is taken over all zones. C_0 is a safety factor (called the Courant number, typically $C_0 \approx 0.5$) and the various limiting time steps are defined as

$$\begin{aligned}
\delta t_1 &= [\min(\Delta x_1,\ \Delta x_2)]/V_s, && \text{(A.16)}\\
\delta t_2 &= \Delta x_1/(v_1 - vg_1), \quad \delta t_3 = \Delta x_2/(v_2 - vg_2), && \text{(A.17)}\\
\delta t_4 &= \min(\frac{\Delta x_1}{4C_2\Delta v_1},\ \frac{\Delta x_2}{4C_2\Delta v_2}), && \text{(A.18)}\\
\delta t_5 &= [\min(\Delta x_1,\ \Delta x_2)]/V_A, && \text{(A.19)}
\end{aligned}$$

where the minimum is taken over all grid zones, V_s is the sound speed and Δx_1, Δx_2, v_1, v_2, vg_1, vg_2 are the cell sizes, velocities, and grid velocities. In our case the 1, 2 directions are z and r. Note that metric factors need to be considered if the coordinate system is curvilinear. C_2 is the dimensionless coefficient of artificial viscosity [96] and V_A is the local Alfvén speed.

The inclusion of explicit viscosity and magnetic resistivity introduces diffusion to the Navier-Stokes and induction equations. For stability, explicit diffusion schemes are limited to time steps

$$\begin{aligned}
\delta t_6 &= [\min(\Delta x_1,\ \Delta x_2)]^2/2\nu\,, && \text{(A.20)}\\
\delta t_7 &= [\min(\Delta x_1,\ \Delta x_2)]^2/2\eta\,. && \text{(A.21)}
\end{aligned}$$

The time step is therefore chosen to

$$\Delta t = C_0/[\max(\delta t_1^{-2} + \delta t_2^{-2} + \delta t_3^{-2} + \delta t_4^{-2} + \delta t_5^{-2} + \delta t_6^{-2} + \delta t_7^{-2})]^{1/2}\,.$$

The codes are benchmarked in Appendix.B.

A.2 New Boundary Conditions

As mentioned before, the original ZEUS code only allows very simple boundary conditions: periodic, outflow, inflow, reflecting—but not no-slip. For our problem, the boundary layer plays an important role, even dominating the bulk fluid through Ekman circulation and/or magnetic-boundary interactions. Most astrophysical simulations model only large-scale phenomena insensitive to the boundary conditions. However one can not usually simulate the physics of a laboratory Taylor-Couette experiment correctly without implementing accurate boundary conditions since the laboratory flows are usually subsonic, and sometimes also sub-Alfvénic, the bulk fluid communicates easily with the boundary. The boundary conditions are chosen to "resemble" the physics at the boundary. ZEUS uses two "ghost zones" as a supplement to implement the boundary condition (Fig. A.1). Additionally ZEUS uses a staggered mesh, defining some variables at the center of the cell and some at the interface/vertices of the cell (Fig. A.2). This has significant implications for the boundary conditions. In the following, several boundary conditions already implemented in ZEUS are introduced.

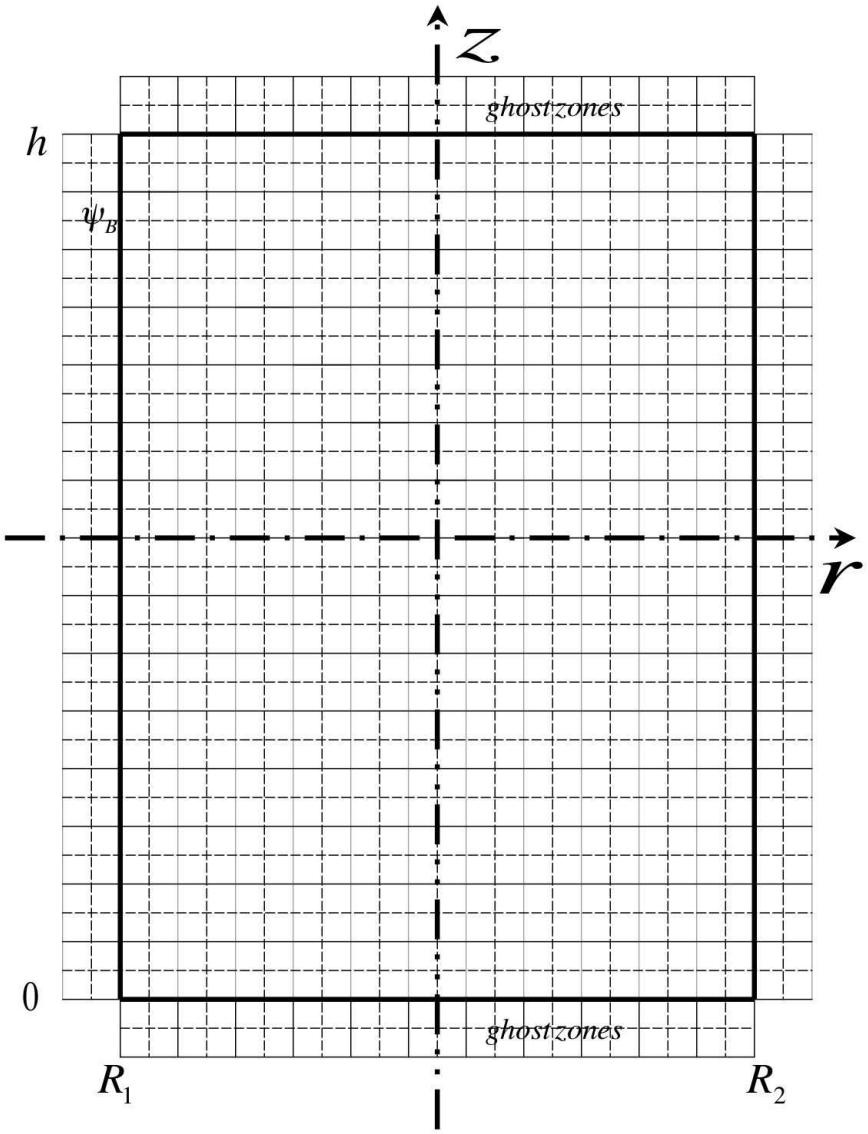

Figure A.1: Computing mesh with ghost zones used in ZEUS. Solid lines are the"a" mesh, dashed lines are the "b" mesh. The thick solid lines are the real boundary, at which the flux function at the boundary Ψ_B is defined. There are two "ghost zones" outside every boundary.

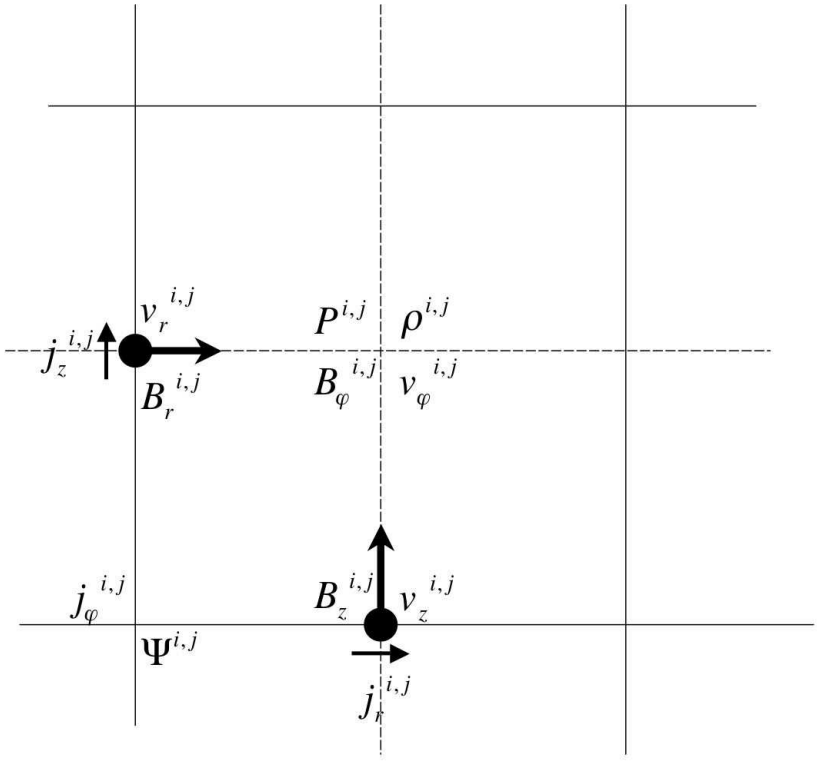

Figure A.2: Positions at which variables are defined. Solid lines are the "a" mesh, dashed lines are the "b" mesh. Ψ is the flux function discussed in the text. The pressure P, the density ρ, the azimuthal magnetic field B_φ and the azimuthal velocity v_φ are defined at the center of the cell. The vertical magnetic field B_z, the vertical velocity v_z and the radial current density j_r are defined at the bottom interface of the cell. The radial magnetic field B_r, the radial velocity v_r and the vertical current density j_z are defined at the left interface of the cell. The azimuthal current density j_φ and the flux function Ψ are defined at the vortex of the cell.

A.2.1 General Boundary Conditions

The general boundary condition with moving boundaries are [117]

$$\frac{d\vec{n}}{dt} = \vec{n} \times [\vec{n} \times (\nabla \vec{v}) \cdot \vec{n}] , \quad \text{(A.22)}$$

$$\vec{n} \cdot [(\rho\vec{v})^i - (\rho\vec{v})^e] = u(\rho^i - \rho^e) , \quad \text{(A.23)}$$

$$\vec{n} \times (\vec{B}^i - \vec{B}^e) = \frac{4\pi}{c}\vec{j}^* - \frac{u}{c}(\vec{E}^i - \vec{E}^e) , \quad \text{(A.24)}$$

$$\vec{n} \cdot (\vec{B}^i - \vec{B}^e) = 0 , \quad \text{(A.25)}$$

$$\vec{n} \times (\vec{E}^i - \vec{E}^e) = \frac{u}{c}(\vec{B}^i - \vec{B}^e) , \quad \text{(A.26)}$$

$$\vec{n} \cdot (\vec{E}^i - \vec{E}^e) = 4\pi\sigma^* , \quad \text{(A.27)}$$

$$\frac{1}{c}\vec{j}^* \times < \vec{B} >_{av} + \sigma^* < \vec{E} >_{av} - \vec{n}(P^i - P^e) = 0 , \quad \text{(A.28)}$$

where q^i and q^e represent the values of q in the interior and in the exterior respectively, $\vec{n}$ is the normal unit vector directed into the interior, $u = \vec{v} \cdot \vec{n}$ is the normal velocity at the boundary, $\sigma^* = \int_0^\delta \sigma ds$ is the surface charge, and $\vec{j}^* = \int_0^\delta \vec{j} ds$ is the surface current.

Obviously, the assumption of finite surface charge σ^* and surface current $\vec{j}^*$ implies infinite values for σ and $\vec{j}$ at the boundary.

Eq. A.22 to Eq. A.28 are derived by integration ($\int_0^\delta ds$) of Eq. A.1 to Eq. A.7 across the boundary layer, where the thickness of the boundary layer δ is taken to be negligible. The equations of state and conservation of mass are trivially satisfied.

Since the boundary wall in the Princeton MRI experiment is fixed and impene-

trable, $u = \vec{v} \cdot \vec{n} = 0$, which simplifies the boundary conditions to

$$\vec{n} \times (\vec{B}^i - \vec{B}^e) = \frac{4\pi}{c}\vec{j}^* \,, \tag{A.29}$$

$$\vec{n} \cdot (\vec{B}^i - \vec{B}^e) = 0 \,, \tag{A.30}$$

$$\vec{n} \times (\vec{E}^i - \vec{E}^e) = 0 \,, \tag{A.31}$$

$$\vec{n} \cdot (\vec{E}^i - \vec{E}^e) = 4\pi\sigma^* \,. \tag{A.32}$$

These are the usual electromagnetic boundary conditions commonly found in the electrodynamic textbooks. In the MHD regime and with $\vec{j}^*$ and σ^* vanishing at the insulating boundary, we get [113, 114]:

$$\vec{B}|_{\text{wall}} \text{ continuous} \,.$$

This is the usual magnetic boundary condition for laboratory Taylor-Couette experiment simulations with an insulating boundary.

A.2.2 Hydrodynamic Boundary Conditions[3]

The hydrodynamic (HD) boundary condition is relatively simple since the fluid is confined inside the solid boundaries unlike the magnetic field, which usually leaks out and extends to infinity. The most frequently used HD boundary condition is the so-called no-slip boundary condition. No-slip means the fluid element at the boundary is at rest in the rotating frame, thus stationary with respect to the rotating boundary.

$$\vec{v}|_{\text{wall}} = 0 \tag{A.33}$$

In the rotating frame, both normal and tangential velocities should be zero. The boundary conditions are straightforward to implement in ZEUS by setting the normal

[3]thanks to Jeremy Goodman for this point

components of the velocity to zero at the boundary while setting the normal and tangential components in the ghost zones equal to the corresponding negative values of their images in the active zones.

A.2.3 Electromagnetic (EM) Boundary Conditions

The electromagnetic boundary conditions are determined by the magnetic diffusivity of the wall material, η_w. We consider here three typical cases:

- perfectly conducting walls: $\eta_w \to 0$;
- insulating walls: $\eta_w = \infty$;
- partially conducting walls: finite η_w .

Vertically Periodic and Radially Conducting Boundary Condition[4]

The periodic boundary condition was implemented in the original ZEUS. The simplest EM boundary condition is the perfectly conducting boundary condition (Fig. A.3).

Initially one vertical uniform magnetic field is imposed while the conducting walls are rotating in the azimuthal direction. Applying the ideal Ohm's law inside the conducting wall

$$\vec{E} + \vec{v} \times \vec{B} = 0 \quad \text{for} \quad \eta = 0\,,$$

gives

$$\vec{E} \times \vec{n} = 0$$

since all components of the velocity and the magnetic field are zero except the azimuthal component of the velocity and the vertical component of the field. Thus, the tangential electric field inside the conducting wall vanishes. The interface condition for the electric field Eq. A.31 implies that the tangential electric field in the fluid also

[4]thanks to Jeremy Goodman for this point

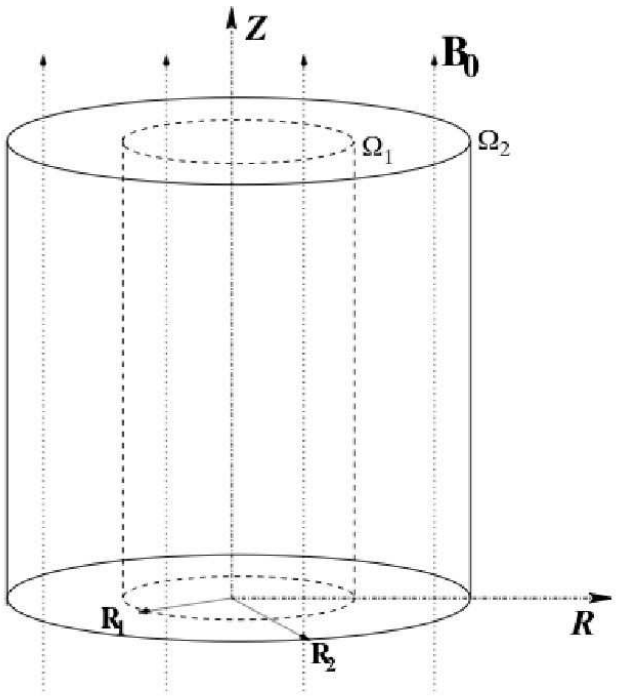

Figure A.3: Diagram of Vertically Periodic and Radially Conducting Boundary Condition. There is an externally imposed vertical constant magnetic field B_0. .

vanishes at the wall:

$$\vec{E} \times \vec{n}|_{\text{wall}} = 0\,. \tag{A.34}$$

Combining with Faraday's Law gives

$$\frac{\partial}{\partial t}(\vec{B} \cdot \vec{n}) = 0 \;\rightarrow \vec{B} \cdot \vec{n} = C\,, \tag{A.35}$$

where C is a constant determined by the initial condition, zero in this case. Using Ohm's law at the wall with Eq. A.33 and Eq. A.35, with $C = 0$, we obtain

$$(\vec{j} \times \vec{n})|_{\text{wall}} = 0\,. \tag{A.36}$$

This relationship means that the tangential components of the current density vanish at the wall. The wall condition for the current density can be transferred to a condition for the magnetic field with the help of Ampére's law. Eq. A.36 then reads

$$(\nabla \times \vec{B}) \times \vec{n}|_{\text{wall}} = 0. \tag{A.37}$$

In our specific case this yields

$$\frac{\partial(rB_\varphi)}{\partial r} = 0\,, \tag{A.38}$$

$$B_r = 0\,. \tag{A.39}$$

The vertical magnetic field B_z in the ghost zones is set equal to the corresponding values of its images in the active zones, to set $j_\theta|_{\text{wall}} = 0$.

Vertically Periodic and Radially Insulating Boundary Condition[5]

This section is inherited and modified from Jeremy Goodman's notes (unpublished).

[5]inherited and modified from Jeremy Goodman's unpublished notes

In insulating walls there is no electric current. Therefore, no current can enter the wall, so the normal component of the current density in the fluid vanishes at the wall:

$$\vec{j} \cdot \vec{n}|_{\text{wall}} = 0\,. \tag{A.40}$$

Assuming axisymmetry and current-free outside the fluid, we get

$$B_\varphi = \frac{C}{r} \text{ for } r \leqslant r_1 \text{ and } r \geqslant r_2\,, \tag{A.41}$$

where C is a constant determined by the initial condition. Without any axial background current, this constant is zero.

The other two poloidal components are more complicated to determine. The perturbed quantities are presumed to be vertically periodic, both in the interior and exterior. If the vertical solution possess multiple vertical modes, then a Fourier transformation is needed:

$$\vec{B}(r,z) = \sum_{n=-\infty}^{\infty} \vec{B}^n(r) \exp\left(i\pi n z/h\right). \tag{A.42}$$

The periodicity length is chosen to be $2h$. Hereafter, a single value of vertical wavenumber $k \equiv \pi n/h > 0$ is assumed. Negative values of k can be handled by taking complex conjugates.

With axisymmetry, it is most advantageous to represent $\vec{B}$ by a flux function in the outside vacuum region:

$$B_r = -r^{-1}\partial_z \Psi\,, \tag{A.43}$$

$$B_z = r^{-1}\partial_r \Psi\,, \tag{A.44}$$

$$r\partial_r(r^{-1}\partial_r \Psi) + \partial_z^2 \Psi = 0\,. \tag{A.45}$$

The elementary solution of Eq. A.45 is

$$\Psi_k(r,z) = \exp(ikz) r[\alpha_k I_1(kr) + \beta_k K_1(kr)]\,, \tag{A.46}$$

where I_1 and K_1 are modified Bessel functions and α_k and β_k are constant coefficients. Since $K_1(x)$ is singular as $x \to 0$ and approaches $(\pi/2x)^{1/2}\exp(-x)$ for $x \gg 1$, while $I_1(x)$ is well-behaved as $x \to 0$ but $I_1(x) \approx (2\pi x)^{-1/2}\exp(x)$ for $x \gg 1$,

$$\alpha_{k_n} = -\frac{B_r^{(n)}(r_1)}{ikI_1(kr_1)}, \quad \beta_{k_n} = 0 \text{ for } r \leqslant r_1\,, \tag{A.47}$$

$$\beta_{k_n} = -\frac{B_r^{(n)}(r_2)}{ikK_1(kr_2)}, \quad \alpha_{k_n} = 0 \text{ for } r \geqslant r_2\,. \tag{A.48}$$

Therefore α_k and β_k are determined by the radial component of the field at the cylinders. Once these components are determined for $k > 0$, the components of $B_r^{(n)}(r)$ and $B_z^{(n)}(r)$ can be calculated in the ghost zones using Eq. A.43, Eq. A.44, and Eq. A.46.

The above analysis is justified only in a continuous system, not on a discrete grid. In a discrete grid, like the staggered mesh used in ZEUS, the flux function Ψ is defined at the vertices of the cell (Fig. A.2), which are shifted from the cell interface at which B_r and B_z are defined (Fig. A.2).

As soon as $B_r(r,z)$ are known at discrete values of z on the boundaries, $B_r^{(n)}(r_1)$ are calculated from $B_r(r_1,z_m)$ with the usual FFT routines,

$$B_r^{(n)}(r) = \frac{1}{N}\sum_{m=0}^{N-1} B_r(r,z_m)e^{\pm i2\pi nm/N}, \quad z_m = z_0 + m\Delta z\,,$$

so that the inverse transform is

$$B_r(r,z_m) = \sum_{n=0}^{N-1} B_r^{(n)}(r)e^{\mp i2\pi nm/N}\,.$$

In either case, $k_n = \pi n/h$ for $1 \leqslant n \leqslant N/2$.

After the Fourier coefficients of $B_r^{(n)}(r)$ and $B_z^{(n)}(r)$ are computed, complex conjugation is used to determine those for $N/2+1 \leqslant n < N$: $B_r^{(N-n)}(r) = [B_r^{(n)}(r)]^*$. The $n = 0$ case is a special case. Since the magnetic field is divergence-free, the radial magnetic field B_r cannot have a nonzero vertical mean: $\Psi_{k=0}(r) = \frac{1}{2} r^2 B_{z,0}$ for all r, where $B_{z,0}$ is the imposed uniform external field. The case $n = N/2$ (Nyquist frequency) is more subtle since its coefficient should be real. Instead of $B_r(r,z) = r^{-1}\partial\Psi/\partial z$, in a finite difference approximation we have

$$B_r(r, z_m) = \frac{\Psi(r, z_{m+1/2}) - \Psi(r, z_{m-1/2})}{r\Delta z}.$$

For a given Fourier component $\Psi_k(r,z) \propto \exp(ikz)$, the finite-difference operator becomes

$$\frac{2i\sin(k\Delta z/2)}{\Delta z}$$

instead of ik. The Fourier components $B_r^{(n)}$ and $\Psi^{(n)}$ are related by this factor. At the Nyquist frequency where $k\Delta z = \pi$, this factor is imaginary with the value of $2i/\Delta z$. However since Ψ is defined at a different location from B_r, there is a shift $\Delta z/2$ between them so $B_r^{(n)}$ and $\Psi^{(n)}$ are also connected by a phase factor $\exp(ik\Delta z/2)$. Since this factor is i at the Nyquist frequency, its product with the factor from the difference operator turns out to be real.

Vertically Insulating and Radially Conducting Boundary Condition for bounded cylinder[6]

This section is inherited and modified from Jeremy Goodman's notes (unpublished).

In order to study magnetic Ekman layer problems, one may choose boundary conditions intermediate between fully conducting and fully insulating boundaries

[6] inherited and modified from Jeremy Goodman's unpublished notes

(Fig. A.4). Specifically, the radial boundaries are taken infinitely long and perfectly conducting while the endcaps are taken perfectly insulating, so the magnetic field is current-free at the top and bottom of the end caps:

$$B_r = 0, \quad \partial_r(rB_\phi) = 0 \quad @\ r = r_1, r_2 \quad \forall z\,, \tag{A.49}$$

$$\partial_r B_z - \partial_z B_r = 0 \quad @\ \{(r,z) : r_1 < r < r_2\,, \quad z < z_{\min} \text{ or } z > z_{\max}\}\,. \tag{A.50}$$

These boundary conditions imply that the total magnetic flux

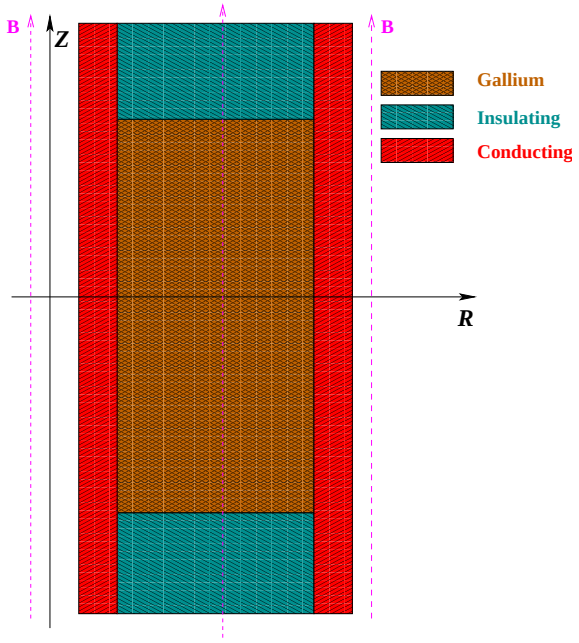

Figure A.4: Diagram of the system with Vertically Insulating and Radially Conducting Boundary Condition.

$$\Psi_0 \equiv 2\pi \int_{r_1}^{r_2} B_z\, r dr \tag{A.51}$$

is independent of z. To satisfy this requirement in a numerical implementation, it is

most convenient to express $\vec{B}$ by a flux function in the vacuum region:

$$B_r = -r^{-1}\partial_z\Psi, \quad B_z = r^{-1}\partial_r\Psi, \quad B_\phi = 0; \tag{A.52}$$

$$r\partial_r\left(r^{-1}\partial_r\Psi\right) + \partial_z^2\Psi = 0. \tag{A.53}$$

Eq. A.53 has the elementary solution

$$\Psi_k(r,z) = re^{-k|z-z_0|}\left[\alpha_k J_1(kr) + \beta_k Y_1(kr)\right], \quad z_0 \equiv z_{\min} \text{ or } z_{\max}, \tag{A.54}$$

where J_1 and Y_1 are Bessel functions, α_k and β_k are constant coefficients, and $k \geq 0$. From Eq. A.49,

$$\begin{aligned} k\left[\alpha_k J_1(kr_1) + \beta_k Y_1(kr_1)\right] &= 0, \\ k\left[\alpha_k J_1(kr_2) + \beta_k Y_1(kr_2)\right] &= 0, \end{aligned} \tag{A.55}$$

$$\Rightarrow \mathcal{D}(k) \equiv k^2\left[J_1(kr_1)Y_1(kr_2) - J_1(kr_2)Y_1(kr_1)\right] = 0. \tag{A.56}$$

Eq. A.56 has distinct solutions $0 = k_0 < k_1 < k_2 < \ldots$, where $k_0 = 0$ is a unique case:

$$\Psi_0(r,z) = \alpha_0 r^2 + \beta_0 \quad \forall \quad z < z_{\min} \text{ or } z > z_{\max}. \tag{A.57}$$

After $k \in \{k_n\}$ is computed from Eq. A.56, α_n/β_n can be calculated from either of the two conditions Eq. A.55. However, the normalization $\alpha_k^2 + \beta_k^2$ is arbitrary since Eq. A.53 is linear.

The vacuum field can be expressed as an expansion of the orthogonal functions

$$\Psi(r,z) = \sum_{n=0}^{\infty} c_n \Psi_{k_n}(r,z)\,, \tag{A.58}$$

$$c_n = N_n^{-1} \int_{r_1}^{r_2} B_z(r,z_0)\partial_r \Psi_{k_n}(r,z_0)\,dr\,. \tag{A.59}$$

The normalization constant is N_n, which is derived to be

$$N_n = \frac{1}{2}\left\{[\partial_r \Psi_{k_n}(r_2,z_0)]^2 - [\partial_r \Psi_{k_n}(r_1,z_0)]^2\right\}\,, \tag{A.60}$$

following Eq. §11.4.2 of Abramowitz and Stegun, *Handbook of Mathematical Functions*. This formula applies even for $n = 0$, when it reduces to $N_0 = 2\alpha_0^2(r_2^2 - r_1^2)$. Henceforth, $\alpha_0 = 1$ and $\beta_0 = 0$ is chosen, without loss of generality.

The total flux of the elementary solution Eq. A.54 is

$$2\pi \int_{r_1}^{r_2} \partial_r \Psi_{k_n}(r,z)\,dr = 2\pi\left[\Psi_k(r_2,z) - \Psi_k(r_1,z)\right].$$

Due to Eq. A.55, this flux should be zero for $n > 0$. However, Ψ_0 involves a nonzero flux and, with $\alpha_0 = 1$, $c_0 = \Psi_0/2\pi(r_2^2 - r_1^2)$ is deduced.

At the endcap $z = z_0$, B_z is defined at the cell interface, $r \in \{r_{\frac{1}{2}}, r_{\frac{3}{2}}, \ldots, r_{j_{\max}-\frac{1}{2}}\}$. The formula Eq. A.59 for c_n approaches:

$$c_n = N_n^{-1} \sum_{j=1}^{j_{\max}} B_z(r_{j-\frac{1}{2}},z_0)\left[\Psi_{k_n}(r_j,z_0) - \Psi_{k_n}(r_{j-1},z_0)\right]. \tag{A.61}$$

Note that this expression is exact if B_z is regarded as constant along each cell edge. The infinite sum in Eq. A.58 is exactly equal to $\Psi(r,z)$ in the vacuum regions. Plainly, a finite value $n_{\max}$ needs to be chosen to truncate the series. In practice, $n_{\max} = j_{\max} - 1$ is taken so that there are exactly as many coefficients $\{c_n\}$ as there are cells.

In order to increase the accuracy of the evaluation of Eq. A.61, which is critical for the success of this method, Gauss-Legendre integration is employed to evaluate Eq. A.61 .

Fully Insulating Boundary Condition for bounded cylinder[7]

Credited to von Hagenow [102], this section is inherited and modified from the class note of Stephen C. Jardin's course, entitled "Computational Methods in Plasma Physics".

For the fully insulating boundary condition, the magnetic field needs to be matched onto a vacuum field vanishing at infinity. This is fairly straightforward in spherical geometry (such as that of many geodynamo experiments) because Laplace's equation is separable. Our case is more complex because while Laplace's equation is uncoupled in an infinite cylinder, it is not fully separable outside a *finite* cylinder. Hence, an integral formulation that is not based on separability is needed. The approach, named after von Hagenow [102], is to determine a surface current at the boundary that amounts to the whole current density inside as the source of the outside field using the free-space Green's function. The surface current is calculated by solving the Grad-Shafranov equation [103, 104] inside with *conducting* boundary conditions, which *is* separable in our case. The problem can be worked out efficiently via a fast Fourier transformation along z and tridiagonal matrix inversion along r.

As usual the flux function Ψ, defined at the vertices, is introduced such that $\vec{B} = \bigtriangledown\varphi \times \bigtriangledown\Psi + B_\varphi \hat{\varphi}$ is the magnetic field. More explicitly, assuming axis-symmetry:

$$B_z = -\frac{1}{r}\frac{\partial}{\partial r}\Psi, \quad B_r = \frac{1}{r}\frac{\partial}{\partial z}\Psi\,. \tag{A.62}$$

[7] credit to von Hagenow [102], inherited and modified from the class note of Stephen C. Jardin's course, entitled "Computational Methods in Plasma Physics"

The flux function Ψ is the solution of the Grad-Shafranov equation [103, 104]

$$\triangle^* \Psi = r j_\varphi \tag{A.63}$$

or, in cylindrical coordinates,

$$r \frac{\partial}{\partial r} \frac{1}{r} \frac{\partial \Psi}{\partial r} + \frac{\partial^2 \Psi}{\partial z^2} = r j_\varphi \,, \tag{A.64}$$

where $j_\varphi = (\bigtriangledown \times \vec{B})_\varphi$ is the toroidal current density and $\triangle^*$ is the Grad-Shafranov operator. Given the basic physical variables in ghost zones, the system can be time advanced using Eqs. A.8 - A.11 and Eq. A.62.

To this point, Ψ has been presumed to be known on the boundary of the computational domain as well as inside the ghost zones. It is not trivial to calculate Ψ on the boundary and inside the ghost zones in the presence of the external current I_i in discrete conductors located at r_i^c, z_i^c as shown in Fig.A.5 (green points).

The Green's function of the operator $\triangle^*$ is known to be

$$G(r, z; r^{'}, z^{'}) = 2 \frac{\sqrt{r r^{'}}}{k} [(2 - k^2) K(k^2) - E(k^2)] \,, \tag{A.65}$$

where $K(k^2)$ and $E(k^2)$ are complete elliptic integrals of the first and second kind. The argument k^2 is defined as

$$k^2 = \frac{4 r r^{'}}{[(r + r^{'})^2 + (z - z^{'})^2]} \,,$$

which can be found in Jackson's *Classical Electrodynamics* as the vector potential due to an axisymmetric current source. Therefore, the Green's function $G(r, z; r^{'}, z^{'})$ and

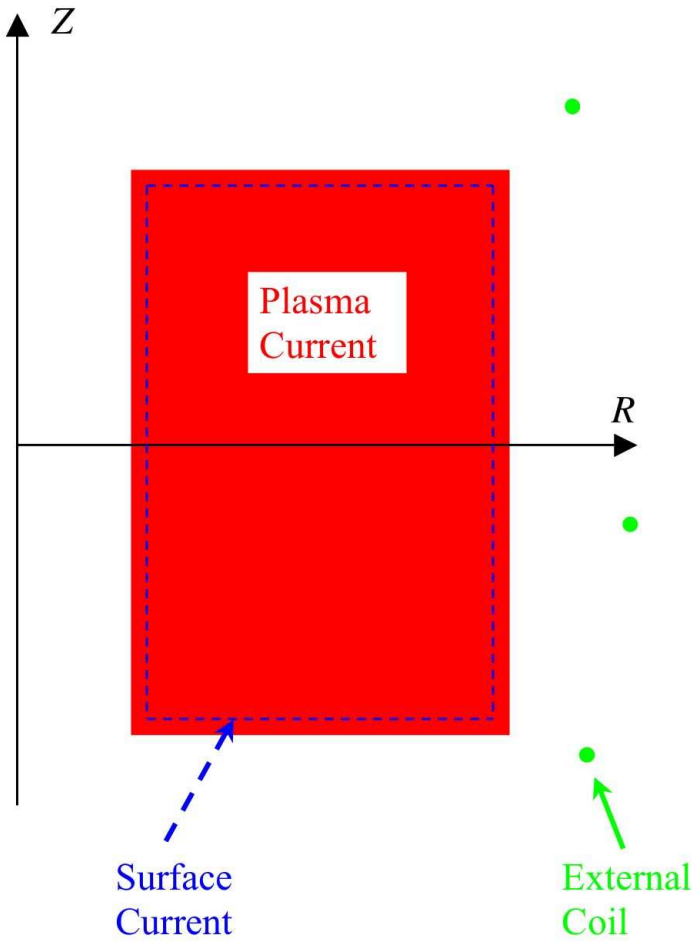

Figure A.5: Schematic Diagram of von Hagenow Method. Green points: external current coils; red colors: induced currents inside the fluid; blue dashed lines: surface current.

the flux function $\Psi(r,z)$ satisfy

$$\triangle^* G(r,z;r^{'},z^{'}) = r\delta(r-r^{'})\delta(z-z^{'})\,, \tag{A.66}$$

$$\triangle^* \Psi(r,z) = r j_\varphi(r,z)\,, \tag{A.67}$$

$$\triangle^* \Psi(r,z) = \sum_{i=1}^{N_c} r I_i \delta(r-r_i^c)\delta(z-z_i^c) \quad \text{in vacuum}\,. \tag{A.68}$$

The appropriate form of Green's theorem is

$$\bigtriangledown\cdot[\Psi\frac{1}{r^2}\bigtriangledown G(r,z;r^{'},z^{'}) - G(r,z;r^{'},z^{'})\frac{1}{r^2}\bigtriangledown\Psi] = \frac{1}{r^2}\Psi\triangle^*(r,z;r^{'},z^{'}) - \frac{1}{r^2}G(r,z;r^{'},z^{'})\triangle^*\Psi\,. \tag{A.69}$$

By integrating Eq.A.69 over the whole space, choosing the observation point $(r^{'},z^{'})$, Ψ at $(r^{'},\, z^{'})$ is obtained as

$$\Psi_{\rm B}(r^{'},z^{'}) = \int_{\rm fluid} G(r,z;r^{'},z^{'}) j_\varphi(r,z) dr dz + \sum_{i=1}^{N_c} G(r_i^c, z_i^c; r^{'}, z^{'}) I_i\,, \tag{A.70}$$

where the right hand side of Eq. A.70 is composed of two parts: the contribution from the fluid currents and the contribution from the external currents. If the computational domain has N cells in each direction, the first part is approximately

$$\sum_{i=1}^{N}\sum_{i=1}^{N} G(r_i,z_j;r,z) j_\varphi(r_i,z_j)\Delta r\Delta z\,, \tag{A.71}$$

where the double sum in Eq.A.71 is extremely time-consuming.

In order to speed up the calculation, we introduce a function $U(r,z)$ that satisfies the same differential equation as Ψ in the interior, but vanishes on the boundary:

$$\triangle^* U = \triangle^*\Psi = r j_\varphi\,,$$

$$U = 0 \quad \text{on boundary}\,.$$

The form of Green's theorem needed now is

$$\bigtriangledown\cdot[U\frac{1}{r^2}\bigtriangledown G(r,z;r^{'},z^{'}]-\bigtriangledown\cdot[G(r,z;r^{'},z^{'})\frac{1}{r^2}\bigtriangledown U]=\frac{1}{r^2}U\triangle^{*}G(r,z;r^{'},z^{'})-\frac{1}{r^2}G(r,z;r^{'},z^{'})\triangle^{*}U\,. \tag{A.72}$$

By placing the observation point $(r^{'},z^{'})$ a tiny displacement ϵ away from the computational boundary, integrating Eq.A.72 over the computational domain, and employing Gauss's theorem, the following expression is obtained for $\epsilon\rightarrow 0$:

$$\int_{\text{fluid}} G(r,z;r^{'},z^{'})J_{\varphi}drdz=\int_{\text{boundary}}\frac{dl}{r}G(r,z;r^{'},z^{'})\frac{\partial U}{\partial n}\,. \tag{A.73}$$

The right hand side of Eq.A.73 requires substantially less effort to evaluate than does the sum in Eq.A.71. The solution U can be obtained by a fast direct elliptic solver within $N^2(4\ln N+5)$ machine operations. Even with the $4N\times 4N$ operations of the line integral in Eq.A.73 for each boundary point, this method is still much less expensive than the $4N^3$ operations required by the double sum.

Thus, the final formula to evaluate Ψ at the boundary and inside the ghost zones is

$$\Psi(r^{'},z^{'})=\int\frac{dl}{r}G(r,z;r^{'},z^{'})\frac{\partial U}{\partial n}+\sum_{i=1}^{N_c}G(r_i,z_i;r^{'},z^{'})I_i\,. \tag{A.74}$$

Partially Conducting Boundary Condition for bounded cylinder[8]

[8]

It is difficult to implement the partially conducting boundary condition in a bounded cylinder for the reason stated in §A.2.3. The implementation of full insulating, no-slip boundary condition and proper treatment of the electromotive force and Lorentz force (discussed in Sec. A.3) forms the foundation for implementation of this boundary condition.

The extra difficulty due to metallic walls is that the hydrodynamical boundary, the

[8]thanks to Hantao Ji for initializing and encouraging me about this point

fluid-wall interface, is separated from the electromagnetic boundary, the wall-vacuum interface. Therefore the computational domain for the Navier-Stokes equation is different from that for the induction equation. The metallic walls are rotating rigidly, so the velocity in the walls is determined. But the magnetic field is evolving dynamically inside this partially conducting walls.

The computing grid should therefore be set up carefully to have the boundary between the wall and fluid (hereafter inner boundary) lie exactly on the *a-mesh* of the staggered mesh used in ZEUS [96, 111].

For the Navier-Stokes equation, the boundary is the inner boundary. In the spirit of ZEUS, two artificial *ghost zones* just beyond the inner boundary are introduced to implement the no-slip boundary condition. Thus the implementation of the hydrodynamic boundary condition requires the velocity in these *ghost zones* to be set up accordingly (§A.2.2). However, those *ghost zones* are also the dynamical zones for the evolution of the magnetic field and the advection terms. Therefore after the Navier-Stokes equation step, these two *ghost zones* should be set to satisfy that the walls are rigidly rotating.

For the induction equation, the boundary is the outer surface of the walls (hereafter outer boundary), at which the full insulating boundary condition discussed in Sec. A.2.3 should be applied. Exactly at the inner boundary, there is an ambiguity as to whether to use $\eta_{\rm wall}$ or $\eta_{\rm fluid}$ in Ohm's law, the practice shows it is better to use the smaller of them.

A.3 Boundary Condition for the Interpolated Physical Variables[9]

[9]thanks to James Stone for reminding me of this point

When the electromotive force and Lorentz force terms are manipulated, the interpolated velocity and field components are required. ZEUS uses the more stable and robust Method of Characteristics (MOC) to calculate the interpolated values. Consequently the boundary values for those interpolated variables need to be set as well. The general principle is the same as before, "to *resemble* the physics on the boundary". For example, for the full Insulating boundary condition, the perturbed azimuthal magnetic field at the boundary should vanish. But B_φ is defined at the cell centers. Therefore the perturbed B_φ must be set to zero at the boundary rather than interpolated, which usually would give out a nonzero B_φ at the boundary, to satisfy that the boundary is magnetically stress free.

A.4 Partially Conducting Boundary Condition for unbounded cylinder[10]

This section is based on the framework laid out in page. 37 of Müller and Bühler [101]. In the linear axisymmetric code used for benchmarking ZEUS, the partially conducting boundary condition described in this section is used.

In most Taylor-Couette laboratory experiments the container walls consist of metallic material with a finite magnetic diffusivity η_w. The analysis of this section depends on the assumption that the wall thickness d_w is small compared to the gap width $r_2 - r_1$, $d_w/(r_2 - r_1) \ll 1$ (Fig. A.3).

The Ohm's law may be applied inside and outside the liquid-solid boundary

$$\vec{E} \times \vec{n} + (\vec{v} \times \vec{B}) \times \vec{n} = \eta j \times \vec{n}\,.$$

[10] following the analysis of page.37 of Müller and Bühler [101]

We get

$$\vec{E} \times \vec{n} + (\vec{v} \cdot \vec{n})\vec{B} - (\vec{B} \cdot \vec{n})\vec{v} = \eta j \times \vec{n}\,,$$

in both sides of the liquid-solid boundary. The surface charge vanishes at the liquid-solid interface, hence the electrical field across this interface is continuous. Combining $\vec{v} \cdot \vec{n} = 0$ and the magnetic field is also continuous, we get at the wall boundary

$$\eta \vec{j} \times \vec{n}|_{\text{wall}} = \eta_w \vec{j_w} \times \vec{n}|_{\text{wall}}\,.$$

Assuming axisymmetry, Ampére's law implies that the normal derivative of the induced azimuthal magnetic field is continuous:

$$\eta \frac{1}{r}\frac{\partial}{\partial r}(rB_\varphi)|_{\text{wall}} = \eta_w \frac{1}{r}\frac{\partial}{\partial r}(rB_{\varphi,w})|_{\text{wall}}\,.$$

In case of thin walls, the induced azimuthal magnetic field in the wall may be expanded in a Taylor series to approximate the gradient. We treat the outer boundary as an example; the inner boundary is similar, although signs differ:

$$\frac{1}{r}\frac{\partial}{\partial r}(rB_{\varphi,w}) = \frac{r_{\text{outside}}B_{\varphi,\text{outside}} - r_{\text{inside}}B_{\varphi,\text{inside}}}{\frac{1}{2}[(r_{\text{inside}} + d_w)^2 - r_{\text{inside}}^2]}\,.$$

$B_{\varphi,\text{outside}}$ and $B_{\varphi,\text{inside}}$, $r_{\text{outside}} = r_2 + d_w$ and $r_{\text{inside}} = r_2$ are the values at the outer and inner surface of the outer container wall. Since there are no currents in the vacuum region outside the outer wall, the induced azimuthal field remains zero, $B_{\varphi,\text{outside}} = 0$. The boundary condition for the induced azimuthal magnetic field can therefore be expressed as

$$\frac{1}{r}\frac{\partial}{\partial r}(rB_\varphi) + \frac{\eta_w}{\eta}\frac{r_{inside}B_\varphi}{\frac{1}{2}[(r_{inside} + d_w)^2 - r_{inside}^2]} = 0\,.$$

We reach the final form of the boundary condition by scaling r to the gap width

$r_2 - r_1$

$$\frac{1}{r}\frac{\partial}{\partial r}(rB_\varphi) + c\frac{B_\varphi}{r_2 - r_1} = 0\,,$$

where the wall conductance parameter c is

$$c = \frac{\eta_w}{\eta}\frac{2r_2(r_2 - r_1)}{((r_2 + d_w)^2 - r_2^2)} \approx \frac{\eta_w}{\eta}\frac{(r_2^2 - r_1^2)}{[(r_2 + d_w)^2 - r_2^2]}\,.$$

This parameter describes the ratio of the electrical resistances of the wall and the fluid.

We have adapted a linear axisymmetric code developed by [45, 53] to allow for a helical field. Vertical periodicity is assumed, to allow separation of variables, but the full viscous and resistive radial equations are solved using finite differences, and a variety of radial boundary conditions including this partially conducting boundary condition have been implemented [46].

Appendix B

Benchmark of the modified ZEUS code

B.1 Code Tests (1) - Wendl's Low-Re Solution

At $Re \ll 1$ and $Re_m = 0$, poloidal flow is negligible and the toroidal flow is steady. The value of V_φ satisfies

$$\nu(\bigtriangledown^2 - \frac{1}{r^2})V_\varphi = 0. \tag{B.1}$$

Wendl [82] has given the analytic solution of this equation for no-slip vertical boundaries co-rotating with the outer cylinder. This serves as one benchmark for the viscous part of our code; note that the vertical boundary conditions differ from those used in the simulations of §2.

Figure B.1 compares results from ZEUS-2D with the analytical result. The maximum relative error is less than 3%. We have also calculated the viscous torque across the mean cylinder ($r = (r_1+r_2)/2$). Wendl's solution predicts $-1.5004\times10^9\,\mathrm{g\,cm^2\,s^{-2}}$, and our simulations yield $-1.5028\times10^9\,\mathrm{g\,cm^2\,s^{-2}}$.

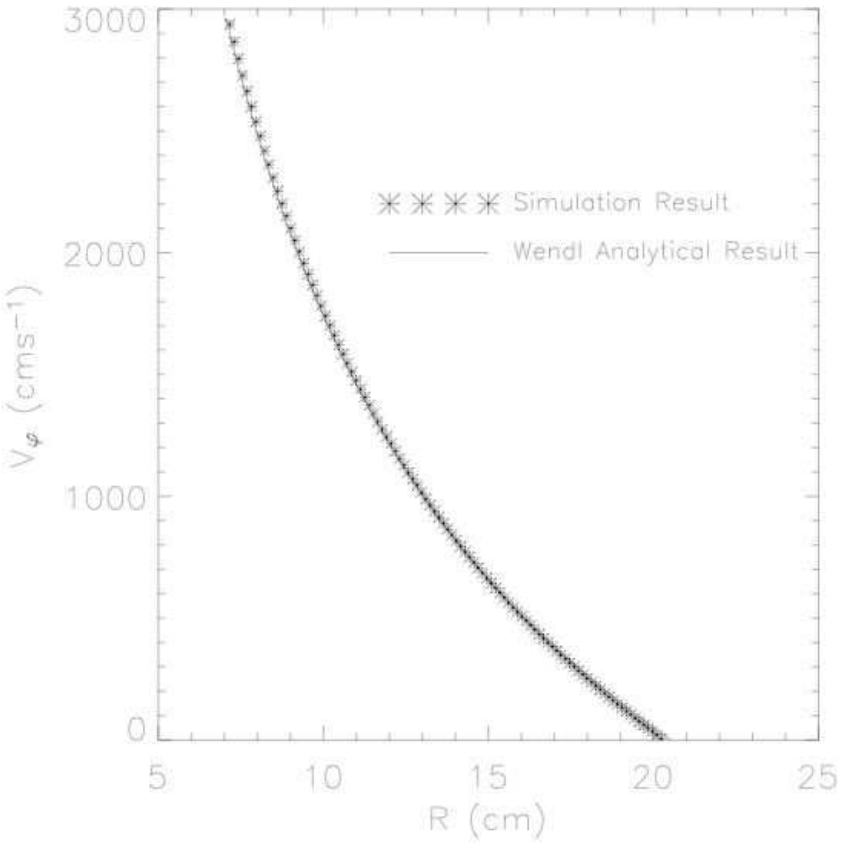

Figure B.1: Radial profile of the azimuthal velocity for $Re = 1$.

B.2 Code Tests (2) - Magnetic Diffusion

If the fluid is constrained to be at rest, then the toroidal induction equation becomes

$$\frac{\partial B_\varphi}{\partial t} = \eta \left(\frac{\partial^2 B_\varphi}{\partial r^2} + \frac{1}{r}\frac{\partial B_\varphi}{\partial r} - \frac{B_\varphi}{r^2} + \frac{\partial^2 B_\varphi}{\partial z^2} \right) \tag{B.2}$$

An exact solution compatible with our boundary conditions is:

$$\mathbf{B} = \hat{\mathbf{e}}_z B_z^0 \ + \hat{\mathbf{e}}_\varphi \frac{B_\varphi^0}{r} \cos(kz) \exp(-\eta k^2 t) \tag{B.3}$$

where k is the wave number, and B_z^0 and B_r^0 are constants. A comparison of the theoretical and simulated results shows that the error scales quadratically with cell size, as expected for our second-order difference scheme (Table B.1).

Re_m	Resolution	Decay Rate $[s^{-1}]$	Exact Rate $[s^{-1}]$	Error (%)
400	100x100	382.52642	392.26048	2.482
400	50x50	352.76963	391.87454	9.979
100	100x100	1533.6460	1569.0419	2.256
100	50x50	1420.4078	1567.4982	9.384

Table B.1: Magnetic Diffusion Test.

B.3 Comparison with an Incompressible Code

ZEUS-2D is a compressible code. However our experimental fluid, gallium, is nearly incompressible at flow speeds of interest, which are much less than its sound speed, $2.7\,\mathrm{km\,s^{-1}}$. As mentioned before, we can approximate incompressible flow by using a subsonic Mach number, $M < 1$. However, since ZEUS is explicit, $M \ll 1$ requires a very small time step to satisfy the CFL stability criterion. As a compromise, we have used $M = 1/4$ (based on the inner cylinder) throughout all the simulations presented in this dissertation. We assume an isothermal equation of state to avoid increases in

M by viscous and resistive heating; the nonlinear compressibility and thermodynamic properties of the actual liquid are in any case very different from those of ideal gases, for which ZEUS was written. Figure B.2 compares results obtained from ZEUS-2D with simulations performed by Kageyama et al. [47] using their incompressible Navier-Stokes code.

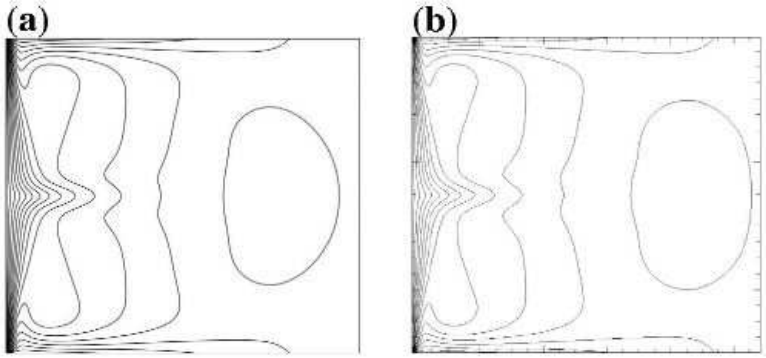

Figure B.2: Comparison with incompressible code at $Re = 1600$: (a) Contours of toroidal velocity from an incompressible code of Kageyama (b) Results from ZEUS-2D with $M = 1/4$.

Bibliography

[1] S. Balbus and J. Hawley, Rev. Mod. Phys. **70**, 1 (1998).

[2] L. Spitzer, *Physics of Fully Ionized Gases.* (Wiley Interscience, New York, 1962).

[3] J. E. Pringle, Ann. Rev. Astron. Astrophys. **19**, 137 (1981).

[4] J. Goodman (2004), unpublished.

[5] N. I. Shakura and R. A. Sunyaev, Astron. Astrophys. **24**, 337 (1973).

[6] S. Balbus and J. Hawley, Astrophys. J. **376**, 214 (1991).

[7] A. Brandenburg, A. Nordlund, R. Stein, and U. Torkelson, Astrophys. J. **446**, 741 (1995).

[8] K. A. Miller and J. M. Stone, Astrophys. J. **534**, 398 (2000).

[9] N. Turner, Astrophys. J. **605**, L45 (2004).

[10] J. Hawley and J. H. Krolik, Astrophys, J. **548**, 348 (2001).

[11] J. de Villiers, J. F. Hawley, and J. H. Krolik, Astrophys. J. **599**, 1238 (2003).

[12] R. F. Webbink, Nature **262**, 271 (1976).

[13] D. Lynden-Bell and J. E. Pringle, Mon. Not. R. Astron. Soc. **168**, 603 (1974).

[14] G. T. Bath and J. E. Pringle, Mon. Not. R. Astron. Soc. **194**, 967 (1981).

[15] G. T. Bath, Q. J. R. Astron. Soc. **19**, 442 (1978).

[16] A. D. Mallama and V. Trimble, Q. J. R. Astron. Soc. **19**, 430 (1978).

[17] O. Reynolds, Philos. Trans. R. Soc. London **174**, 935 (1883).

[18] F. Wendt, Ing. Arch. **4**, 577 (1933).

[19] G. Taylor, Proc. Roy. Soc. London A **157**, 546 (1936).

[20] D. Richard and J. P. Zahn, Astro. Astrophys. **347**, 734 (1999).

[21] D. Richard, Ph.D. thesis, Université Paris 7 (2001).

[22] F. Schultz-Grunow, Z. angew. Math. Mech. **39**, 101 (1959).

[23] B. Dubrulle, Icarus **106**, 59 (1993).

[24] W. J. Duschl, P. A. Strittmatter, and P. L. Biermann, Astron. Astrophys. **357**, 1123 (2000).

[25] J. M. Hure, D. Richard, and J. P. Zahn, Astron. Astrophys. **367**, 1087 (2001).

[26] H. Ji, M. Burin, E. Schartman, and J. Goodman, Nature **444**, 343 (2006).

[27] J. F. Hawley and S. A. Balbus, Astrophys. J.. **376**, 223 (1991).

[28] E. P. Velikhov, J. Expl Theoret. Phys. (USSR). **36**, 1398 (1959).

[29] S. Chandrasekhar, Proc. Nat. Acad. Sci. **46**, 253 (1960).

[30] E. Knobloch, Mon. Not. R. Astron. Soc. **255**, 25 (1992).

[31] C. Gammie and S. Balbus, Mon. Not. R. Astron. Soc. **270**, 138 (1994).

[32] C. Curry and R. Pudritz, Astrophys. J. **453**, 697 (1995).

[33] S. Balbus and J. Hawley, Astrophys. J. **392**, 662 (1992).

[34] S. Chandrasekhar, *Hydrodynamic and Hydromagnetic Stability* (Oxford University Press, 1961).

[35] R. Donnelly and M. Ozima, Phys. Rev. Lett. **4**, 497 (1960).

[36] R. Donnelly and M. Ozima, Proc. R. Soc. Lond. A **266**, 272 (1962).

[37] R. Donnelly and D. Caldwell, J. Fluid Mech. **19**, 257 (1964).

[38] A. Brahme, Physica Scripta **2**, 108 (1970).

[39] D. R. Sisan, N. Mujica, W. A. Tillotson, Y. Huang, W. Dorland, A. B. Hassam, T. M. Antonsen, and D. P. Lathrop, Phys. Rev. Lett. **93**, 114502 (2004).

[40] R. Hollerbach and G. Rüdiger, Phys. Rev. Lett. **95**, 124501 (2005).

[41] G. Rüdiger, R. Hollerbach, M. Schultz, and D. Shalybkov, Astron. Nachr. **326**, 409 (2005).

[42] F. Stefani, T. Gundrum, G. Gerbeth, G. Rüdiger, M. Schultz, J. Szklarski, and R. Hollerbach, Phys. Rev. Lett. **97**, 184502 (2006).

[43] G. Rüdiger, R. Hollerbach, F. Stefani, T. Gundrum, G. Gerbeth, and R. Rosner, Astrophys. J. **649**, L145 (2006).

[44] F. Stefani, T. Gundrum, G. Gerbeth, G. Rüdiger, J. Szklarski, and R. Hollerbach (2007), submitted to New J. Phys.

[45] W. Liu, J. Goodman, I. Herron, and H. Ji, Phys. Rev. E **74**, 056302 (2006).

[46] W. Liu, J. Goodman, and H. Ji, Phys. Rev. E. **76**, 016310 (2007).

[47] A. Kageyama, H. Ji, J. Goodman, F. Chen, and E. Shoshan, J. Phys. Soc. Japan. **73**, 2424 (2004).

[48] D. Cannell, M. Dominguez-Lerma, and G. Ahlers, Phys. Rev. Lett. **50**, 1365 (1983).

[49] M. Burin, E. Schartman, H. Ji, R. Cutler, P. Heitzenroeder, W. Liu, L. Morris, and S. Raftopolous, Exp. Fluids **40**, 962 (2006).

[50] R. Hollerbach and A. Fournier, in *MHD Couette Flows: Experiments and Models, American Inst. Phys. Conf. Proc.*, edited by G. Rosner, G. Rüdiger, and A. Bonanno (2004), vol. 733, pp. 114–121.

[51] K. Stewartson, J. Fluid Mech. **3**, 17 (1957).

[52] H. Ji, J. Goodman, and A. Kageyama, Mon. Not. R. Astron. Soc. **325**, L1 (2001).

[53] J. Goodman and H. Ji, J. Fluid Mech. **462**, 365 (2002).

[54] C. F. Gammie and K. Menou, Astrophys. J. **492**, L75 (1998).

[55] O. M. Blaes and S. A. Balbus, Astrophys. J. **421**, 163 (1994).

[56] C. Gammie, Astrophys. J. **457**, 355 (1996).

[57] M. Wardle, Mon. Not. Astron. Soc. **307**, 849 (1999).

[58] T. Sano, S. Miyama, T. Umebayashi, and T. Nakano, Astrophys. J. **543**, 486 (2000).

[59] J. Hawley, Comp. Phys. Comm. **89**, 127 (1995).

[60] R. Matsumoto and T. Tajima, Astrophys. J. **445**, 767 (1995).

[61] J. Stone, J. Hawley, C. Gammie, and S. Balbus, Astrophys. J. **463**, 656 (1996).

[62] J. F. Hawley, S. A. Balbus, and W. Winters, Astrophys. J.. **518**, 394 (1999).

[63] N. A. Krall and A. W. Trivelpiece, *Principles of Plasma Physics* (San Francisco Press, San Francisco, 1986).

[64] R. M. Kulsrud, *Handbook of Plasma Physics*, vol. 1 (Elsevier Science B.V., North Holland, 1983).

[65] P. B. Snyder, G. W. Hammett, and W. Dorland, Phys. Plasmas **4**, 3974 (1997).

[66] E. J. Quataert, W. Dorland, and G. W. Hammet, Astrophys. J. **577**, 524 (2002).

[67] P. Sharma, G. W. Hammett, and E. Quataert, Astrophys. J. **596**, 1121 (2003).

[68] P. Sharma, G. W. Hammett, E. Quataert, and J. M. Stone, Astrophys. J. **637**, 952 (2006).

[69] K. Noguchi, V. I. Pariev, S. A. Colgate, H. F. Beckley, and J. Nordhaus, Astrophys. J. **575**, 1151 (2002).

[70] E. P. Velikhov, A. A. Ivanov, V. P. Lakhin, and K. S. Serebrennikov, Physics Letters A. **356**, 357 (2006).

[71] E. P. Velikhov, A. A. Ivanov, V. S. Zakharov, A. O. Livadny, and K. S. Serebrennikov, Physics Letters A. **358**, 216 (2006).

[72] I. V. Khalzov, V. I. Ilgisonis, A. I. Smolyakov, and E. P. Velikhov, Phys. Fluids **18**, 124107 (2006).

[73] W. Liu, J. Goodman, and H. Ji, Astrophys. J. **643**, 306 (2006).

[74] E. Knobloch and K. Julien, Mon. Not. R. Astron. Soc. **000**, 1 (2005).

[75] W. Liu, J. Goodman, and H. Ji (2007), in preparation.

[76] W. Liu, J. Goodman, and H. Ji (2007), in preparation.

[77] P. A. Gilman and E. R. Benton, Phys. Fluids **11**, 2397 (1968).

[78] D. E. Loper, Phys. Fluids **12**, 2999 (1970).

[79] P. Gilman, Phys. Fluids **14**, 7 (1971).

[80] E. R. Benton and J. H. S. Chow, Phys. Fluids **12**, 2174 (1972).

[81] A. S. Gupta, Acta Mechanica **13**, 155 (1972).

[82] M. C. Wendl, Phys. Rev. E. **60**, 6192 (1999).

[83] G. Rüdiger and D. Shalybkov, Phys. Rev. E **66**, 016307 (2002).

[84] G. Rüdiger, M. Schultz, and D. Shalybkov, Phys. Rev. E **67**, 046312 (2003).

[85] G. Rüdiger and Y. Zhang, Astron. Astrophys. **378**, 302 (2001).

[86] S. Balbus and J. Hawley, Mon. Not. R. Astron. Soc. **266**, 769 (1994).

[87] K. Menou, S. Balbus, and H. Spruit, Astrophys. J. **607**, 564 (2005).

[88] T. P. Fleming, J. M. Stone, and J. F. Hawley, Astrophys. J. **457**, 355 (2000).

[89] T. Sano and S. Inutsuka, Astrophys. J. **561**, L179 (2001).

[90] V. Pariev, Magnetohydrodynamics **2**, 123 (2003).

[91] I. Herron and F. Soliman, Applied Mathematics Letters **19**, 1113 (2005).

[92] M. Ilgner and R. Nelson, Astron. Astrophys. **445**, 205 (2006).

[93] E. Knobloch, Phys. Fluids **8**, 1446 (1996).

[94] I. Herron and J. Goodman, Z. angew. Math. Phys. **57**, 615 (2006).

[95] G. Rüdiger and R. Hollerbach (2007), http://arxiv.org/pdf/0705.0883.

[96] J. Stone and M. Norman, ApJS. **80**, 753 (1992).

[97] E. Ince, *Ordinary Differential Equations* (Dover, New York, 1956).

[98] J. Szklarski and G. Rüdiger, Astron. Nachr. **327**, 844 (2006).

[99] G. Lesur and P.-Y. Longaretti, Astron. Astrophys. **444**, 25 (2005).

[100] J. C. Hayes, M. L. Norman, R. A. Fiedler, J. O. Bordner, P. S. Li, S. E. Clark, A. ud Doula, and M.-M. M. Low., Astrophys, J. Suppl. **165**, 188 (2006).

[101] U. Müller and L. Bühler, *Magnetohydrodynamic flows in ducts and cavities.* (Springer-Verlag, 2000), chap. 3, page 39.

[102] K. Lackner, Comput. Phys. Comm. **12**, p33 (1976).

[103] H. Grad and H. Rubin, Proceedings of the 2nd UN Conf. on the Peaceful Uses of Atomic Energy **31**, 190. (1958).

[104] V. Shafranov, Reviews of Plasma Physics **2**, 103 (1966).

[105] T. Von Kármán, Math. Phys. Klasse **5**, 58 (1930), available in English translation as NACA TM 611, 1931.

[106] S. Goldstein, Proceedings of the Royal Society of London. Series A, Mathematical and Physical Scoence **159**, 473 (1937).

[107] S. Balay, W. D. Gropp, L. C. McInnes, and B. F. Smith (2001), http://www.mcs.anl.gov/petsc.

[108] S. Balay, W. D. Gropp, L. C. McInnes, and B. F. Smith, Tech. Rep. ANL-95/11 - Revision 2.1.5, Argonne National Laboratory (2003).

[109] S. Balay, W. D. Gropp, L. C. McInnes, and B. F. Smith, in *Modern Software Tools in Scientific Computing*, edited by E. Arge, A. M. Bruaset, and H. P. Langtangen (Birkhauser Press, 1997), p. 163202.

[110] C. Evans and J. F. Hawley, ApJ. **33**, 659 (1988).

[111] J. Stone and M. Norman, ApJS. **80**, 791 (1992).

[112] T. Mullin, Y. Toya, and S. Tavener, Phys. Fluids **14**, 2778 (2002).

[113] A. Iskakov, S. Descombes, and E. Dormy, Journal of Computational Physics **197**, 540 (2004).

[114] A. Iskakov and E. Dormy, Geophysical and Astrophysical Fluid Dynamics **99**, 481 (2005).

[115] F. Alouges, ESAIM Control Optim. Calc. Var. **6**, 629 (2001).

[116] M. Xu, F. Stefani, and G. Gerbeth (2007), http://arxiv.org/abs/0704.2657.

[117] T. H. Stix, *Waves in Plasmas* (Springer-Verlag, New York, 1992).